THÈSE

En vue de l'obtention du

DOCTORAT DE L'UNIVERSITÉ DE TOULOUSE

Délivré par :

Institut National Polytechnique de Toulouse (Toulouse INP)

Discipline ou spécialité :

Génie Mécanique, Mécanique des Matériaux

Présentée et soutenue par :

M. SHARAN RAJ RANGASAMY MAHENDREN

le lundi 14 septembre 2020

Titre :

Thermomechanical behaviour of multi-cracked brittle media taking into account unilateral effects: theoretical and numerical approaches

---

Ecole doctorale :

Mécanique, Energétique, Génie civil, Procédés (MEGeP)

Unité de recherche :

Laboratoire de Génie de Productions de l'ENIT (E.N.I.T-L.G.P.)

Directeur(s) de Thèse :

M. OLIVIER DALVERNY

MME HÉLÈNE WELEMANE

Rapporteurs :

M. ALBERT GIRAUD, ECOLE NATIONALE SUPERIEURE DE GEOLOGIE

M. DJIMÉDO KONDO, UNIVERSITE SORBONNE

Membre(s) du jury :

M. FRÉDÉRIC LEBON, AIX-MARSEILLE UNIVERSITE, Président

M. AMEVI TONGNE, ECOLE NATIONALE D'INGENIEUR DE TARBES, Membre

Mme HÉLÈNE WELEMANE, ECOLE NATIONALE D'INGENIEUR DE TARBES, Membre

M. OLIVIER DALVERNY, ECOLE NATIONALE D'INGENIEUR DE TARBES, Membre

என் தாய், தந்தை, பாட்டி மற்றும் தாய் தமிழுக்கு சமர்பணம் ...

To my parents and grandmother ...

My greatest fear is that by the time that they have come to love,
we will have come to hate.

- Anonymous

தொட்டனைத் தூறும் மணற்கேணி மாந்தர்க்குக்
கற்றனைத் தூறும் அறிவு. (குறள் – 396)

– திருவள்ளுவர்

Acknowledgement

This manuscript is the synthesis of three years of research work carried out at the Laboratoire Génie de Production (LGP) of the Ecole Nationale d'Ingénieurs de Tarbes (ENIT). Thesis works are often associated with autonomy and personal investment, however, it could not have been completed without the participation of many people. Therefore, the following lines are intended to express my gratitude and appreciation towards them.

First of all, I would like to thank Frédéric Lebon, Professor Université d'Aix-Marseille for having accepted to preside over the jury of my thesis. I would like to express my sincere gratitude to Albert Giraud, Professor Université de Lorraine and Djimédo Kondo, Professor Sorbonne Université for agreeing to review this thesis work and their invaluable comments.

I would also like to thank my thesis director Olivier Dalverny, Professor ENIT, who guided me throughout my thesis, for our discussions, for his valuable scientific qualities and his constructive criticism as well as all the help he gave me.

I'm deeply grateful to my thesis co-director Hélène Welemane, Associate Professor ENIT, for the supervision of my work, for her support and encouragement in moments of doubts during all these years of study. It has not always been easy, but I thank you for your scientific insights, kindness, positive attitude, enthusiasm and for sharing with me your knowledge, and also for allowing me to push past my limits. I wish you all the best to become a "big boss" yourself soon.

I thank Amèvi Tongne, Associate Professor ENIT, who co-supervised my thesis and ensured its follow-up. His numerous ideas and knowledge of FEM, allowed me to advance in my work.

I would like to thank Jean Denape, former Research Director of LGP and also secretaries Eliane Casta and Marie Teixeira for making me feel welcome at the laboratory. My sincere gratitude to teaching-researchers: Olivier Pantale, Jean-Pierre Faye, Christian Garnier, Marina Fazzini, ... and fellow researchers and doctoral students: Roger-Pierre, Matthias, Ferhat, Mohamed Medhat, Yves, Vincent, Rami, Hassan, Marie, Shahriar, ...

I thank my subcontinent friends: Mahadev, Saif, Faheem and Sagar for their unforgettable moments in France. A special thanks to my favourite librarian Chantal Barutau of ENIT. I also extend my regards to director Catherine Azzaro Pantel and secretary Kamila Koziura of MEGEP doctoral school.

Finally, these results would not have been the same without the support, trust and encouragement from my family and friends Siva, Clyde and Iryna. Above all, thank a lot my beloved Louis for being my rock and your family for giving me a second home.

Table of contents

List of Figures

List of Tables

List of Symbols

Tensorial Notations

a	scalar
$\mathbf{a}$	unit vector
$\mathbf{A}$	second order tensor
$\mathbb{A}$	fourth order tensor
$\mathbf{I}$	second order identity tensor
$\mathbf{I} = \mathbf{I} \overline{\underline{\otimes}} \mathbf{I}$	fourth order identity tensor
$\cdot$	simple contraction
:	double contraction
$\otimes$	tensor product
$\mathbb{J}$	$= \frac{1}{3} \mathbf{I} \otimes \mathbf{I}$
$\mathbb{K}$	$= \mathbb{I} - \mathbb{J}$
$(\mathbf{A} \overline{\underline{\otimes}} \mathbf{B})_{ijkl}$	$= \frac{1}{2}(\mathrm{A}_{ik}\mathrm{B}_{jl} + \mathrm{A}_{il}\mathrm{B}_{jk})$

Other Symbols

$\mathbf{n}$	unit vector normal to the plane of the cracks
$\boldsymbol{\alpha}_c$, $\boldsymbol{\alpha}_m$	thermal strain tensor of cracks and the matrix respectively
$\boldsymbol{\alpha}_{hom}$	effective thermal strain tensor of the microcracked media
$\boldsymbol{\kappa}_c$, $\boldsymbol{\kappa}_m$	thermal stress tensor of cracks and the matrix respectively
$\boldsymbol{\kappa}_{hom}$	effective thermal stress tensor of the microcracked media
$\boldsymbol{\lambda}_c$, $\boldsymbol{\lambda}_m$	thermal conductivity tensor of cracks and the matrix respectively
$\boldsymbol{\lambda}_{hom}$	effective thermal conductivity tensor of the microcracked media
$\boldsymbol{\rho}_c$, $\boldsymbol{\rho}_m$	thermal resistivity tensor of cracks and the matrix respectively
$\boldsymbol{\rho}_{hom}$	effective thermal resistivity tensor of the microcracked media

σ, $\mathbf{\Sigma}$	microscopic and macroscopic stress tensors respectively
ε, $\mathbf{E}$	microscopic and macroscopic strain tensors respectively
$\mathbf{A}, \mathbf{B}$	gradient localization and flux concentration tensors respectively
$\mathbf{a}, \mathbf{b}$	thermal strain localization and stress concentration tensors respectively
$\mathbf{S}^E$	depolarization tensor
$\Delta T = T_1 - T_0$	difference between temperatures T_1 and T_0
λ_c, λ_m	scalar thermal conductivity of cracks and the matrix respectively
$(\mathbf{t}, \mathbf{v}, \mathbf{k})$	orthonormal coordinate system of the simulated volume in 3D
$(\mathbf{t}, \mathbf{v})$	orthonormal coordinate system of the simulated volume in 2D
$(\mathbf{X}, \mathbf{Y}, \mathbf{Z})$	orthonormal coordinate system in ABAQUS
$\mathbb{A}, \mathbb{B}$	strain localization and stress concentration tensors respectively
$\mathbb{C}_c, \mathbb{C}_m$	elastic stiffness tensor of cracks and the matrix respectively
$\mathbb{C}_{hom}$	effective elastic stiffness tensor of the microcracked media
$\mathbb{P}^E$	first Hill tensor
$\mathbb{Q}^E$	second Hill tensor
$\mathbb{S}^d$	spatial distribution tensor
$\mathbb{S}^E$	Eshelby tensor of cracks
$\mathbb{S}_c, \mathbb{S}_m$	elastic compliance tensor of cracks and the matrix respectively
$\mathbb{S}_{hom}$	effective elastic compliance tensor of the microcracked media
$\mathcal{A}$	simulated area with dimension $L \times L$
$\mathcal{N}$	number of cracks (per unit volume in 3D, per unit area in 2D)
μ_c, μ_m	shear modulus of cracks and the matrix respectively
Ω	volume (in 3D) or area (in 2D) of the RVE (with boundary $\delta\Omega$)
ω	mean aspect ratio of the cracks
ρ	material density
ρ_c, ρ_m	scalar thermal resistivity of cracks and the matrix respectively
A	cross sectional area of the simulated volume
a, c	mean semi-axes of the cracks

$c_{\varepsilon,c}, c_{\sigma,c}$	scalar specific heat capacity (per unit volume) of cracks at constant strain and stress respectively
$c_{\varepsilon,hom}, c_{\sigma,hom}$	effective specific heat capacity (per unit volume) at constant strain and stress respectively
$c_{\varepsilon,m}, c_{\sigma,m}$	scalar specific heat capacity (per unit volume) of the matrix at constant strain and stress respectively
d	scalar density of the cracks
$E^*, \nu^*, \mu^*, \alpha^*$	fictitious Young's modulus, Poisson's ratio, shear modulus and thermal expansion of the closed cracks respectively
E_c, ν_c	Young's modulus and Poisson's ratio of the cracks respectively
E_m, ν_m	Young's modulus and Poisson's ratio of matrix respectively
f_c, f_m	volume fraction of cracks and the matrix respectively
g, G	microscopic and macroscopic temperature gradient respectively
$G_{\mathbf{t}}, G_{\mathbf{v}}, G_{\mathbf{k}}$	temperature gradient along the direction $\mathbf{t}, \mathbf{v}$ and $\mathbf{k}$ respectively
k_c, k_m	bulk modulus of cracks and the matrix respectively
q, Q	microscopic and macroscopic heat flux respectively
$Q_{\mathbf{t}}, Q_{\mathbf{v}}, Q_{\mathbf{k}}$	total heat flux along the direction $\mathbf{t}, \mathbf{v}$ and $\mathbf{k}$ respectively
s	entropy
U	specific free enthalpy (per unit volume)
V	simulated volume with dimension $L \times L \times L$
W	specific free energy (per unit volume)

Abbreviations & Acronyms

BEM	Boundary Element Method
CMC	Ceramic Matrix Composite
CTE	Coefficient of Thermal Expansion
EHM	Equivalent Homogeneous Material
FEA	Finite Element Analysis
FEM	Finite Element Method
MFH	Mean-Field Homogenization

MT	Mori-Tanaka
PCW	Ponte Castañeda-Willis
ppm	parts per million
RC	Reference Configuration
RVE	Representative Volume Element
SEM	Scanning Electron Microscope
UCS	Ultimate Compressive Strength

General introduction

The design and realization of optimized technological systems are increasing through the development and integration of different functions and combining elements of varied nature. As the need and demand for extreme conditions resistant materials increases, especially to high and ultra-high temperature, research study and development of materials are necessary. For several applications, brittle materials (ceramics, concrete, composites, rocks, etc.) are faced with such kind of requirements.

Ceramics which fall between metallic and non-metallic compounds are a typical example of these materials due to their refractory properties. They are known to have relatively high stiffness and strength, some of them even higher than metals. They are also well known for low electrical and thermal conductivities, sometimes showing higher temperature resistance than metals. Heat management at higher temperatures is a key for energy savings in power electronics and energetics. In most cases, the higher the energy efficiencies are, the higher the operating temperatures will be. So, high-temperature heat exchangers based on ceramic materials have a wide range of applications. A special kind of ceramics called ultra-high temperature ceramics (UHTC) has applications in the field of aerospace. Most used UHTC's are zirconium diboride (ZrB_2) and hafnium diboride (HfB_2) for making the leading edge of hypersonic vehicles (Fig. 1a) and tantalum carbide (TaC) for making rocket nozzles. Not only in the field of space but also power electronics or energetics, there are many ceramic parts linked by various processes (like brazing, sintering, shrinking) to metallic/non-metallic elements of different physical, mechanical and thermal properties. When these assemblies are subjected to high levels of thermo-mechanical loadings, microcracks induced by the manufacturing process can grow, increasing the damage and by the same way the thermomechanical phenomena leading to the failure of the system.

Brittle composite materials like Ceramic Matrix Composites (CMCs) are well known for their high-temperature capability, reduced cooling requirements, low weight, and high specific strength. This makes them an ideal candidate for making turbine blades (Fig. 1b), combustion chambers for jet engines and brake discs in automobiles. In the nuclear industry, due to their ability to withstand high temperatures and high mechanical damage tolerance and good chemical compatibility with coolants, CMCs are considered for the construction of internal reactor structures.

Concretes are also one of the most studied brittle material due to their immense ap-

(a) Falcon HTV-2 (b) Turbine blade (c) Fire damaged building

Figure 1: Brittle materials at high temperature.

plication in the field of civil and construction engineering. Concretes are known for their high compressive strength (sometimes up to nearly ten times their tensile strength), low thermal expansion and moderate thermal conductivity. The increasing need for High-Performance concrete (HPC) in construction has seemingly compromised its fire resistance. To be fire-resistant, walls should have the necessary load-bearing capacity, insulation and integrity (no significant cracks). So the walls must carry the load for the duration of the fire. Since all concretes are prone to microcracking to some extent, it is important to know their influence in case of fire (Fig. 1c).

Rocks which are considered as porous materials (including pores, voids and cracks) have applications in petroleum engineering and deep geological repository for radioactive waste. Sedimentary rock with very low permeability, high mechanical strength acts as a natural barrier for underground storage of nuclear wastes. These rocks can be subjected to natural mechanical, thermal and/or chemical loadings. This phenomenon is referred to as thermo-chemo-mechanical. So, investigating the effective properties, thermal or elastic or thermoelastic, is equally important.

As these various examples have shown, the use of temperature resistant brittle materials is of great interest in the advanced industries but also in geotechnical and civil domineering fields. Yet, all these materials initially exhibit some heterogeneities (for instance inclusions, fibres, cracks or porosity) at their microscale, induced by their formation or manufacturing process. Under high levels of thermomechanical loadings, these defects induce significant over-stresses that can lead to microcracks growth and irreversible damage in materials and structures. Though the influence of mechanical loading on cracks is a widely explored topic, the impact of thermal and thermomechanical loading needs further investigation. This thesis intends to focus on the effect of cracks on the brittle materials and their interaction with thermal and thermomechanical behaviour. In the

coming sections are presented some number of elements that will help to position the work presented below.

Damage by microcracking

Mechanical properties of various solids are firmly based on their interior defects and inhomogeneities. For different kind of materials, the defects might originate due to various reasons and can come in different geometric shapes and sizes. Damage in ductile materials such as aluminium, copper, titanium, etc., primarily involves nucleation and evolution of micro-voids whereas in brittle materials like concrete, ceramics, rocks, CMC, etc., damage is predominantly due to microcracking (Fig. 2).

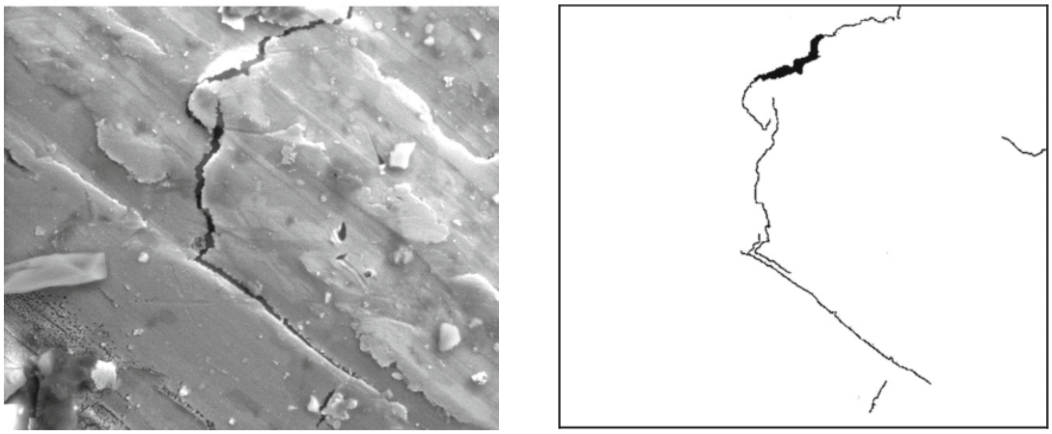

(a) SEM image (b) Microcrack profile

FIGURE 2: Microcrack in ZTA ceramics (×50000 magnification) (Shiliang *et al.* 2015).

Microcracking can be generated during the formation (rocks) or manufacturing process. For brittle materials such as ceramics, cooling from high sintering temperature often creates sufficiently large stresses to cause internal spontaneous cracking (Buessem

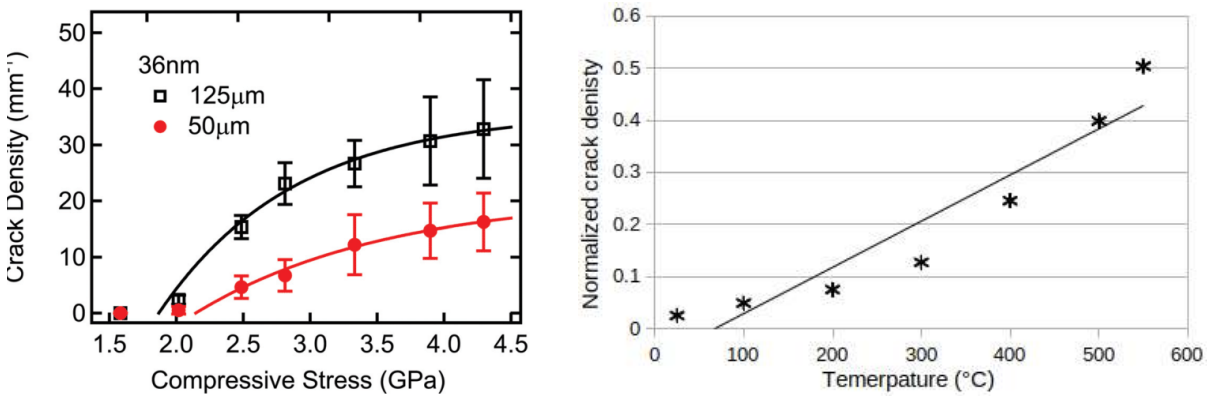

(a) Alumina films (b) Sandstone

FIGURE 3: Influence of (a) mechanical load and film thickness (Jen *et al.* 2011), and (b) temperature on cracks (Kim *et al.* 2020).

and Lange 1966, Case *et al.* 1981). Also during service conditions, some solids show many kinds of defects based on their exposure to various factors such as mechanical loads (Fig. 3a), temperature (Fig. 3b) or any environmental conditions.
The main consequence of microcracking in brittle materials are as follows:

- Stress-strain nonlinearity,
- Deterioration of properties,
- Induced anisotropy,
- Unilateral effect.

It is imperative to discuss the above-mentioned consequences in detail. The following paragraphs analyze these different points, to better understand the different aspects of damage by microcracking on the mechanical properties.

Stress-Strain nonlinearity

Fig. 4 shows the general non-linear behaviour of some ceramic materials under mechanical loads.

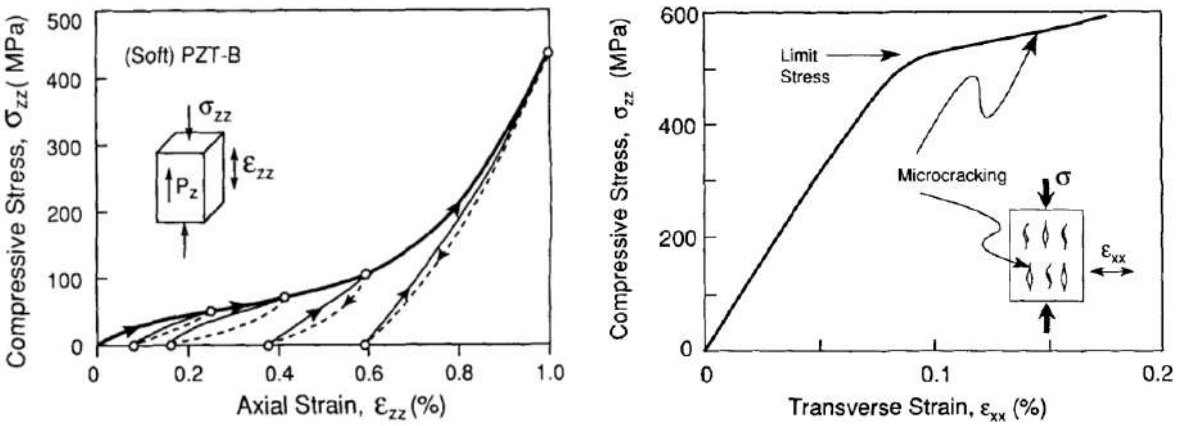

(a) PZT ceramics (b) PMN-PT ceramics

FIGURE 4: Stress-strain non-linearity in ceramics (Cao and Evans 1993).

This non-linearity is mainly attributed to degradation of properties, unilateral effect in some cases (both discussed later) and also for some materials irreversible strain (Fig. 4b). For instance, sometimes, the fragment of a damaged microcrack or an inclusion can get stuck between crack lips and not allow the crack to close perfectly during unloading, leading to an additional strain.

Even when we have a fixed damage (i.e. fixed damage density), nonlinearity is observed. The material in such a case exhibits nonlinearity in terms of hysteresis loop during loading – unloading cycles (Fig. 4a). This phenomenon is mainly due to the closure of cracks and frictional sliding of the microcracks. So, based on the applied load, type of load and microstructural phenomenon affecting them, this nonlinearity can therefore be important.

Deterioration of mechanical properties

Progressive and irreversible deterioration of material properties can be due to the formation of defects (voids, cracks, etc.) which characterizes the damage.

Due to the influence of microcracking, there can be a 10% to 30% loss in Young's modulus when compared with virgin (non-microcracked) material. Such degradation of elastic properties can be seen through unloading phases of mechanical tests (Fig. 4a). Wong *et al.* (1996) show that peak strength of marbles drops with increasing initial crack density (Fig. 5a). Fig. 5b gives the modulus reduction as a function of crack density in Calcium alumino silicate glass ceramic (CAS/SiC) composite.

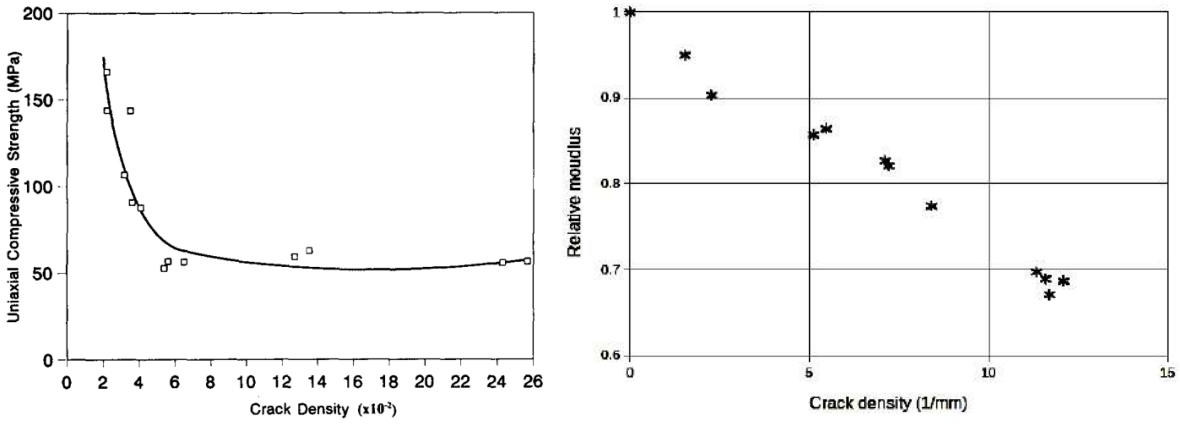

(a) (b)

Figure 5: Deterioration of (a) Uniaxial Compressive Strength (UCS) in Yuen Long marbles (Wong *et al.* 1996) and (b) Young's modulus in a brittle matrix composite (Evans and Zok 1994).

Induced anisotropy

The orientation of the microcracks depends on the loading path, their normals being directed in the direction of maximum elongation. Let us consider an initially isotropic material under mechanical loading. After some load level, microcracks start to appear and they exhibit preferential orientation related to the load direction and nature (i.e. tension or compression). Due to this directional dependency, the initially isotropic material becomes anisotropic, its resulting anisotropy being related with cracks orientation. Fig. 6 gives data obtained from analyses of crack orientation in ceramics under uniaxial tension. We clearly observe in this figure that cracks do not always follow the preferential path and they indeed have oriented nature.

Fig. 7 shows the distribution of the Young's modulus of a ceramic composite that is mainly degraded in some directions. Note that the resulting anisotropy is clearly a function of the load direction but can be affected by initial anisotropy of the material (see comparison between Figs. 7a and 7b done for two load directions). Results show that microcracking affects not only axial properties but also transverse and shear properties.

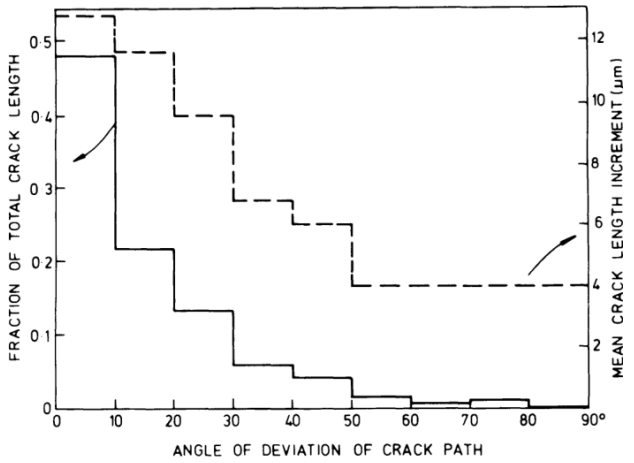

FIGURE 6: Variation of incremental crack length and proportion of crack length as a function of crack orientation (Tappin *et al.* 1978).

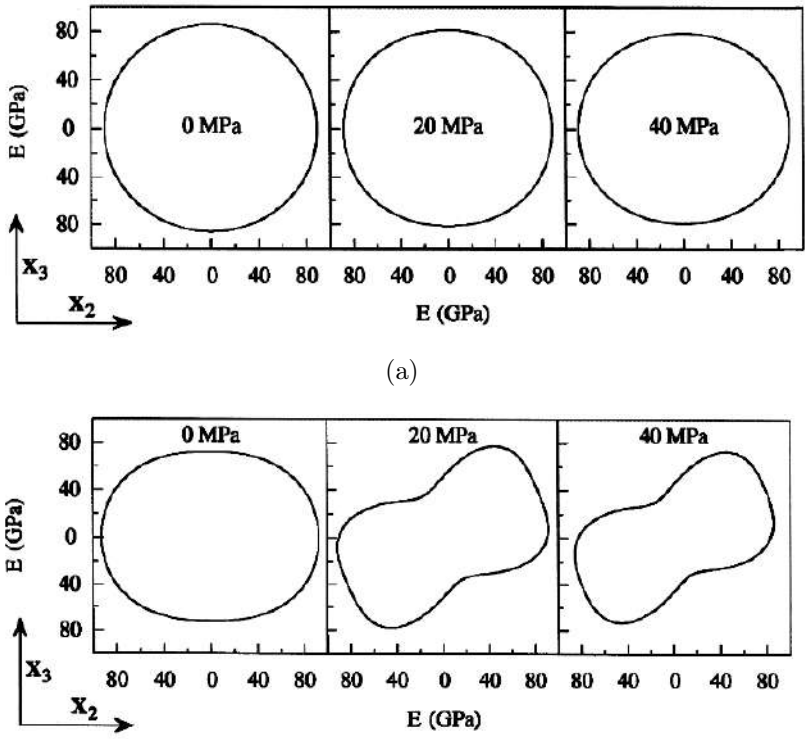

(a)

(b)

FIGURE 7: Young's modulus E (**m**) associated with the unit vector direction **m** in the plane (x_2, x_3) as a function of the tensile stress applied in the x_3 direction for a CC-SiC composite: (a) x_3 corresponds to one of the fiber directions (0°), (b) x_3 forms an angle of 30° with one of the fiber directions, (Baste and Aristégui 1998).

Unilateral effect

Since cracks are surface decohesion defects, they might open or close according to the local tension or compression mechanical load on their lips. According to their state (open or closed), cracks have different influence on the macroscopic behavior of the material.

This is known as unilateral effect. Specially, closure of cracks results in some recovery in the materials properties compared to the open state (Fig. 8).

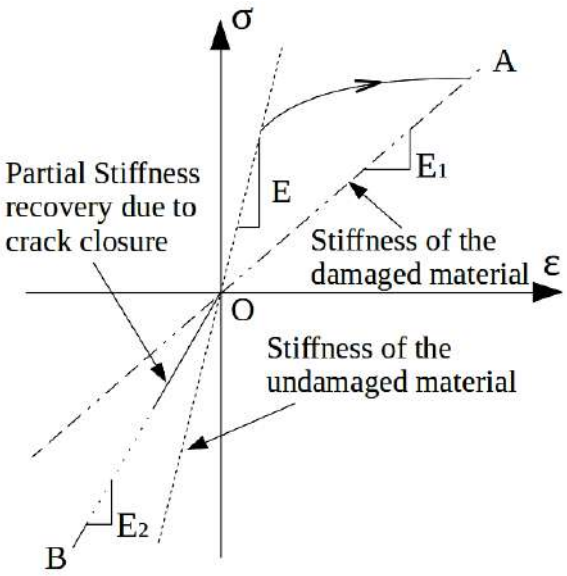

FIGURE 8: Schematic response of a material subjected to uniaxial compression after being damaged in tension: Material damaged in tension (path OA) then unloaded (path AO) and loaded in compression (path OB).

Another consequence of this behavior can be the dissymmetry between tension and compression loads. There can be a huge contrast between the tension fracture stress (Fig. 9a) and compression fracture stress (Fig. 9b). The lower stiffness in tension is mainly due to the fact that microcracks are opened whereas the higher stiffness in compression can be attributed to microcracks closure. This shows that microcracks evolve differently based on their status (open/closed) and has a varied influence on a macroscopic level. Typically after unloading, several microcracks "disappear" (i.e. become closed). Fig. 10 clearly shows this cracks closure in rocks.

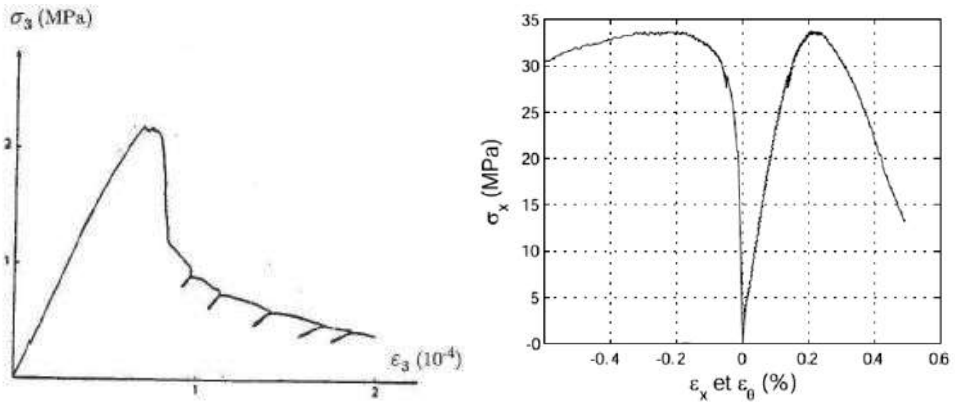

(a) (b)

FIGURE 9: Concrete under simple (a) tension (Terrien 1980) and (b) compression (Vu 2007).

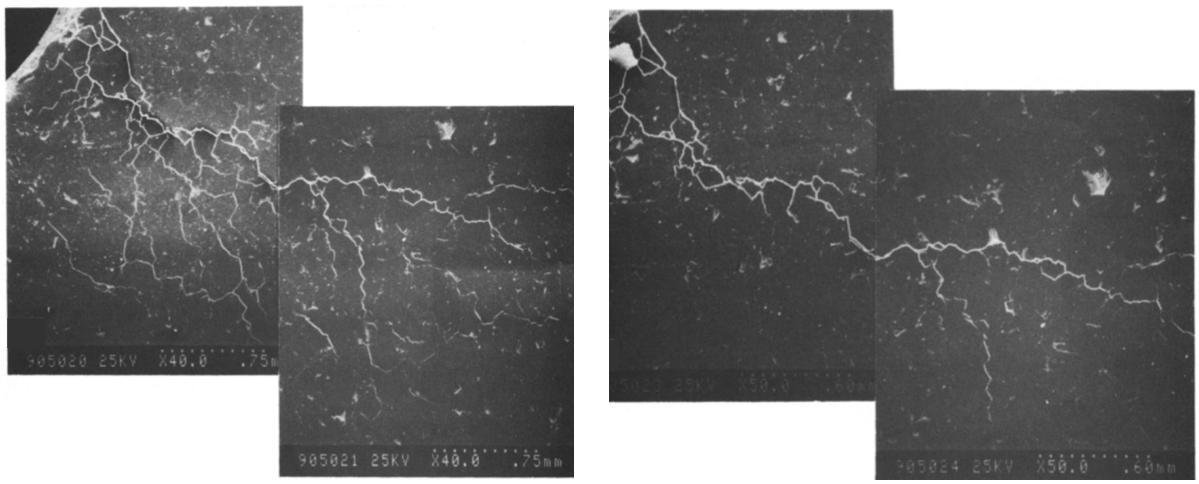

(a) (b)

FIGURE 10: SEM microphotographs of the crack distribution in slotted rock: (a) during loading and (b) after unloading (Zhao *et al.* 1993).

Extension to thermal issues

As mentioned in the previous section, not only mechanical properties but also thermal properties can be affected by microcracking. In retrospect, two specific aspects can be identified as:

- influence of the thermal loads on microcracking,
- influence of microcracking on thermal properties.

This is important since the brittle materials which are the subject of the study, are generally refractory which exacerbates the thermomechanical effects. In what follows, we will discuss the importance of these aspects.

Influence of thermal loads on microcracking

Civil engineering provides the most studies on thermal response of brittle materials. Especially it is critical to study the behaviour of concrete during fire or thermal hazard conditions. The performance of cement-based material under elevated temperatures are very complicated and difficult to characterize.

Thermal loading results in both physical and chemical changes in the microstructure affecting the mechanical behaviour. Researchers agree that there is a decrease in mechanical characteristics of brittle materials due to thermal induced microcracking. Their influence on elastic properties (Fig. 11a), strength (Fig. 11b), stiffness (Nechnech *et al.* 2002, Griffiths *et al.* 2017) and compressive strength (Gardner *et al.* 2005, Vejmelková *et al.* 2008) are well known.

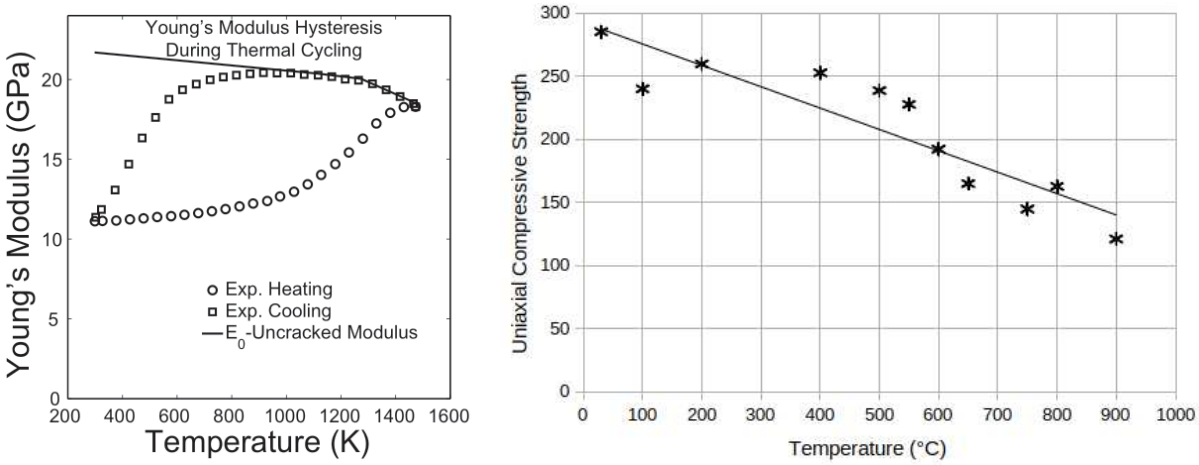

(a) ceramics (b) granite

FIGURE 11: Influence of microcracking on (a) Young's modulus in ceramics during thermal loading (Fertig and Nickerson 2015) and (b) UCS in granite as a function of thermal stressing temperature (Griffiths *et al.* 2017).

Fig. 12 shows the effect of exposure to temperature on a sandstone subjected to hydrostatic compression. According to temperature level, we can see at the early stages of the mechanical load the decrease in compressibility modulus K. This can be attributed to increasing damage, induced by exposure to increasing temperature. We could also note in the figure that with increasing compression load the compressibility modulus is recovered to its initial value K_0. Such unilateral effect, related to closure of defects, confirms that thermal-induced cracks are responsible for the deterioration process involved here.

Vejmelková *et al.* (2008) found up to 80% decrease in the compressive strength in various concretes (Tab. 1). Such degradation of properties due to thermal loading is not only seen in concrete but also into other brittle materials (in rocks Sibai *et al.* 2003, Ghassemi Kakroudi 2007, Chen *et al.* 2012a, in granite Lin 2002, Chen *et al.* 2012b, in quasi-brittle materials Tang and Tang 2015).

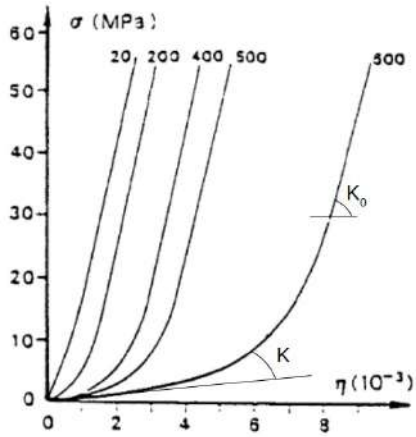

FIGURE 12: Hydrostatic compression of a thermally pre-cracked sandstone at different temperature levels (Homand-Etienne *et al.* 1987).

Table 1: Effects of thermally induced cracks in high performance concrete (Vejmelková *et al.* 2008)

High Performance Concretes	**Compressive Strength** MPa		**Thermal conductivity** λ [W· m^{-1}·K^{-1}]	
	without cracks at 25 °C	with cracks at 600 °C	without cracks at 25 °C	with cracks at 600 °C
BBI	63.57	21.49	4.16	2.90
BII	83.47	32.33	2.36	1.43
PI	119.06	29.86	0.637	0.510

So far the influence of thermal load on mechanical properties due to microcracking was presented, now, it is imperative to investigate how thermal loading affects damage evolution. Lin (2002) verified that higher the peak temperature load, higher is the microcrack density. The author also noted that the density of intragranular cracks accounts for a major percentage of the overall crack density and grain boundary cracks contribute very less. Damhof (2010) observed that thermal-induced damage linearly depends on temperature (Fig. 13a). The author goes on to add that the damage originates purely from the thermal expansion mismatch in the refractory material. This can be seen in Fig. 13a, where damage occurs only after the start of thermal loading. Griffiths *et al.* (2017) note a stable crack length but an increase in the number of cracks under thermal loading. This increase in the number of cracks leads to an increase in the crack density (Fig. 13b). After producing varied explanations for a near-constant density after 600 °C, they conclude that it is probable that microcracks stop growing after this point, and rather open (increase in aspect ratio). This could explain why strength decreases with temperature but crack density remains constant after 600 °C (Figs. 11b and 13b). Kim *et al.* (2020) study sandstone specimens which have pre-existing cracks due to environment. They observe that at low temperatures microcracks evolve slowly when compared to higher temperatures (Fig. 3b). The literature has a lot more investigation exploring how damage evolution takes

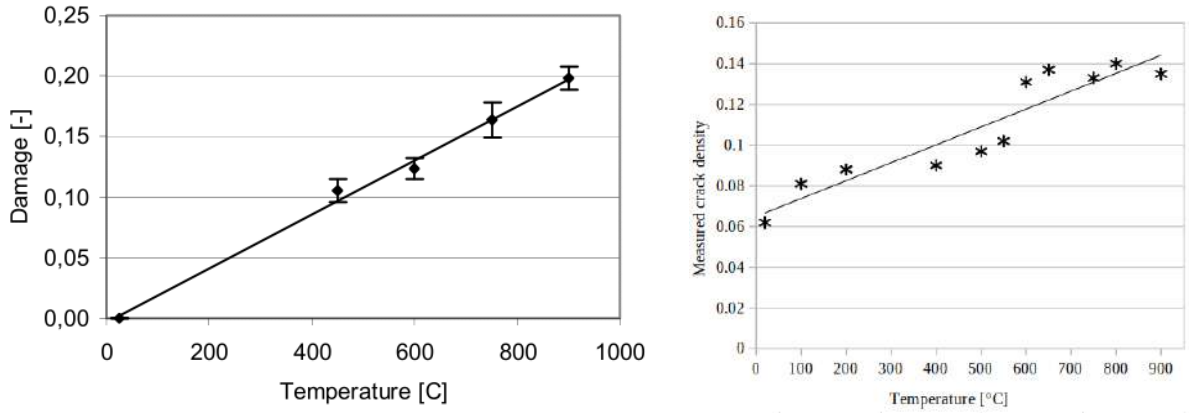

(a) (b)

Figure 13: Damage evolution in (a) refractory material (Damhof 2010) and (b) granite (Griffiths *et al.* 2017), as a function of temperature.

place during thermal loading. From these information, we can say that temperature plays a major role in microcracking growth, both in thermal-induced cracks and pre-existing cracks.

Influence of microcracking on thermal properties

Microcracks not only influence the mechanical properties (Fig. 5a) but also have effects on the optical, electrical, magnetic and thermal properties as well. Experimental data on the effect cracks have on thermal properties is very scarce. One such paper is from Vejmelková *et al.* (2008), who shows up to a 40% drop in the thermal conductivity of various concretes (Tab. 1). Kim *et al.* (2000) presents that transverse cracks in carbon-epoxy composite affect and change the thermal expansion of the laminate (Fig. 14a). From this, we can establish that thermal loading affects both mechanical response and heat flow process.

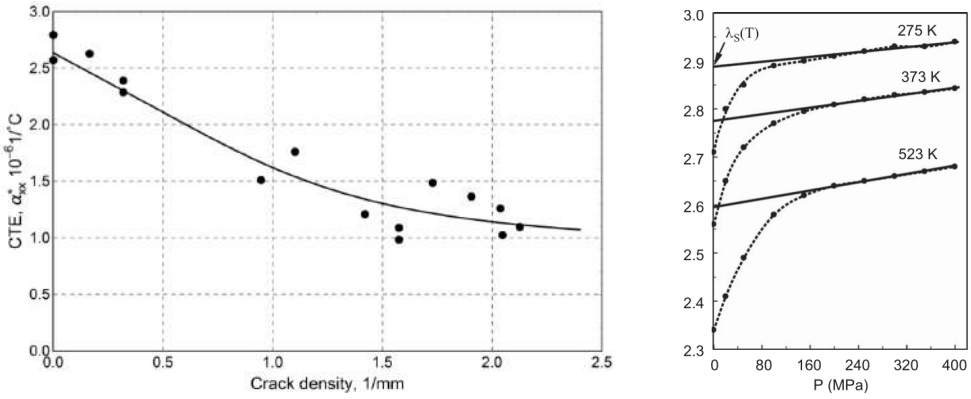

(a) (b)

Figure 14: (a) Deterioration of the Coefficient of Thermal Expansion (CTE) in a carbon-epoxy composite (Kim *et al.* 2000) (b) Thermal conductivity of sandstone as a function of pressure at various temperatures (Abdulagatova *et al.* 2009).

Fig. 14b gives us the influence of temperature on thermal conductivity in sandstone under pressure loading. Based on the increase in the temperature, we see decrease in the conductivity. This is due to the evolution of damage during thermal loading. Interestingly, the increase in conductivity for a given temperature can be explained by cracks closure. Even then, at high pressure when all cracks are closed, further increase in pressure does not have a big impact on the conductivity. From this, it is safe to say that thermal-induced cracks are responsible for the loss in thermal conductivity.

It is imperative to understand that both the influence of thermal loads on cracks development and the influence of cracks existence on thermal properties are closely linked. Having said that, this thesis will focus on the latter, which will be the precursor in creating a fully coupled thermomechanical damage model. Predicting or calculating the effective properties of a heterogeneous media (with inclusion or cracks) for real configurations is challenging due to their complex geometry, boundary conditions or loads and/or consti-

tutive behaviours. In addition, the lack of experimental data makes it very relevant to investigate the effects of microcracking through other means, such as homogenization and numerical simulations.

Homogenization

Length scale separation

In continuum micromechanics, homogenization methods are used to find the effective response of finite statistically homogeneous materials. Homogenization is typically build on the principle of *separation of scales* (Zaoui 2002). The lowest scale described is microscale, largest is macroscale and intermediate ones are called mesoscale. In a classic formulation, the characteristic length of the studying inhomogeneity d, much be smaller than the size ℓ of the Representative Volume Element (RVE). This RVE should be representative of the material to be studied irrespective of its location in the structure. Then, ℓ must be smaller than the characteristic dimension L of the whole body and fluctuation length η of the prescribed loading. To put all this together,

$$d_0 \ll d \ll \ell \ll L, \qquad \ell \ll \eta \tag{1}$$

where d_0 is the lowest possible length of the inhomogeneity below which continuum mechanics cannot be used.

Methodology

Homogenization can be interpreted as describing the behaviour of a heterogeneous material at lower length scale in terms of a fictitious Equivalent Homogeneous Material (EHM) at higher length scale (Fig. 15). This process is done by means of homogenization applied on the RVE. Accordingly, such volume should remain sufficiently small to contain all the necessary information describing the behaviour of the heterogeneous material, and at the same time, large enough to make itself a meaningful sample of the material.

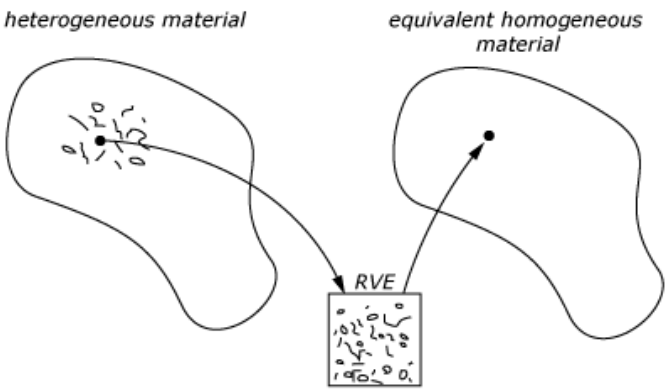

Figure 15: Homogenization of a heterogeneous medium/material.

One of the most commonly used homogenization technique is Mean-Field Homogenization (MFH) and known for its computational efficiency. MFH is based on approximate volume average quantities (stress, strain, flux, gradient, etc.) over each phase to derive the overall behaviour of the heterogeneous material. The quantities are based on the homogenization schemes used, which are in turn based on the assumptions made about the interaction between the matrix and the inclusions. Some of such well known schemes are dilute, self-consistent, differential, Mori-Tanaka (MT), Ponte Castañeda-Willis (PCW), etc.

Existing works

Homogenization techniques were first developed to study the effective properties of composites. Over the years many, researchers have studied the effective elastic (Hill 1963, Hashin 1983, François *et al.* 2012, Dvorak 2013), thermoelastic (Levin 1967, Laws 1973), thermal (Torquato 2002, Pietrak and Wiśniewski 2015) and other properties of the composites.

Most of the existing research on MFH is based on the pioneering works of Eshelby (1957). Eshelby introduces a fourth order tensor depending on the matrix property and the shape of the inclusion to find the effective elastic properties. Though Eshelby's *equivalent inclusion method*, also called *eigenstrain method*, was developed for an ellipsoidal inclusion, other shapes like spheroidal, penny-shape, cylindrical can be considered as a special case of an ellipsoid.

Later, the methods were extended to material inhomogeneities (fibres, inclusions, voids, cracks, etc) emphasizing their shapes. Focusing on cracks, *direct* homogenization methodology uses displacement jump between crack lips to derive the elastic properties (Kachanov 1993, Nemat-Nasser and Hori 1993). If the cracks are considered as penny-shaped inclusion (which is a limit case for an ellipsoid), then, we can use the above mentioned Eshelby's method (Eshelby 1957) to solve for the effective elastic and thermoelastic properties (Budiansky and O'Connell 1976, Mura 1987, Dormieux and Kondo 2016).

Due to the mathematically analogy between the elasticity and steady-state heat conduction (Bristow 1960), authors have extended modelling approaches to solve thermal problem of a microcracked media. One such example is Sevostianov (2006), who uses *direct* methodology to predict the effective conductivity by studying temperature jump across the crack lips. Though many authors tried to extend *equivalent inclusion method* to steady-state, Hatta and Taya (1986) were the first one to propose a general method to solve the problem. They introduce a new tensor (later named as *depolarization* tensor) which is similar to the Eshelby tensor in elasticity but only depends on the shape of the inclusion. They give thermal conductivity of two and three phase composites as a function of the depolarization tensor where the fibres are assumed be a cylindrical (another limit case of ellipsoid). They also provide the components of *depolarization* tensor for various

inclusion shapes. Fig. 16 shows the normalized thermal conductivity of an aligned short SiC fibre/epoxy composite (Hatta and Taya 1986).

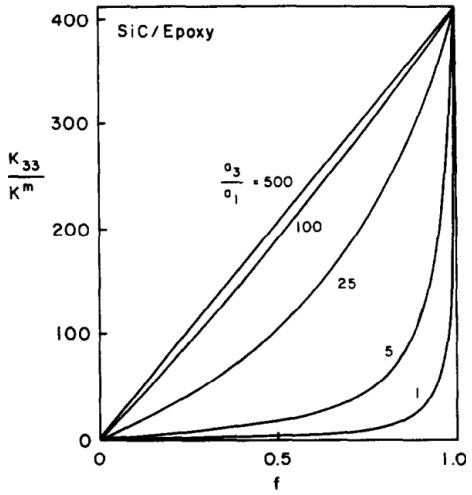

FIGURE 16: Thermal conductivity of two phase composite along the x_3 axis (K_{33}) normalized by K_m as a function of fibre volume fraction f for various aspect ratios (Hatta and Taya 1986).

From this information, it is clear that the theoretical framework for finding the effective elastic, thermoelastic and thermal properties of composite materials already exists. In the present work, attention is paid to the special case of microcracks. The modelling of elastic properties of microcracked media has been extensively investigated in the literature, and methodologies are often considered to be easily extendable to thermal behaviours. Yet, closed-form expression of thermal and thermoelastic properties are not provided in existing works. Accordingly, this work intends to implement homogenization theories to derive the thermomechanical response of microcracked media. Without existing exhaustive experimental characterization of these issues, the homogenization approach can be helpful for the study and optimization of brittle materials in view of previously-mentioned industrial applications. Moreover, due to the specific feature of cracks defects, it seems important to account for the interaction between their unilateral behaviour and the overall thermal behaviour of materials.

Numerical simulations

In addition to the theoretical approach, we also propose to address these aspects through numerical simulations. Several numerical methods can be used for the simulation of the materials effective behaviour. One can cite for instance, Fast Fourier Transform (FFT), Boundary Element Method (BEM), Finite Difference Method (FDM), Finite Element Method (FEM), etc. There are few numerical studies done on the effective thermal properties of microcracked media, many of them are based on FEM.

For example, Lu and Hutchinson (1995) suggests a FEM (in ABAQUS) to find the overall conductivity of a matrix-cracked composite. The discretization is done for a quar-

ter of the model with quadratic axisymmetric elements. They simulate the behaviour of temperature gradient and heat flux field near the crack tip. Authors also show good agreement between the analytical and simulated solutions (Fig. 17). Finally, they state that the numerical results are insensitive to the meshing when crack density is low but very much sensitive when it is high.

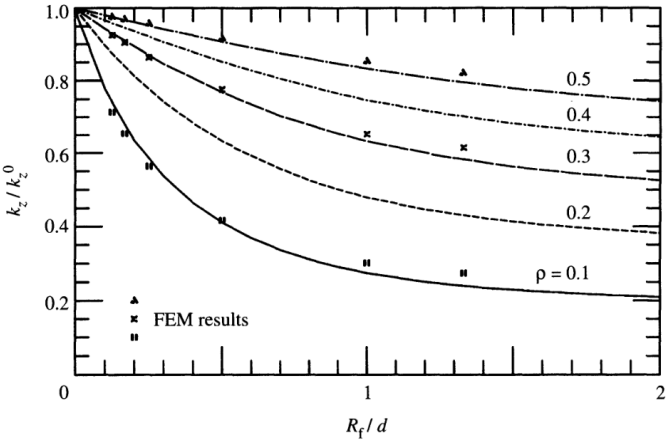

FIGURE 17: Normalized longitudinal conductivity k_z/k_z^0 as a function of normalized crack density R_f/d for various fibre volume fraction ρ (Lu and Hutchinson 1995).

Carson *et al.* (2003) investigate the overall thermal conductivity of a porous material with pores and inclusions with very low conductivity. They perform their analysis on a 2D Finite Element grid using *PDEase2D*™and study the influence of the inclusion size, shape, and interactions. Fig. 18 shows that as volume fraction (in turn crack density) increases, the effective conductivity decreases. Fig. 18a is given for three inclusion shapes considered for the simulation. In Fig. 18b, the Maxwell structure refers to no interaction between inclusions and intermediate structure to interaction between them.

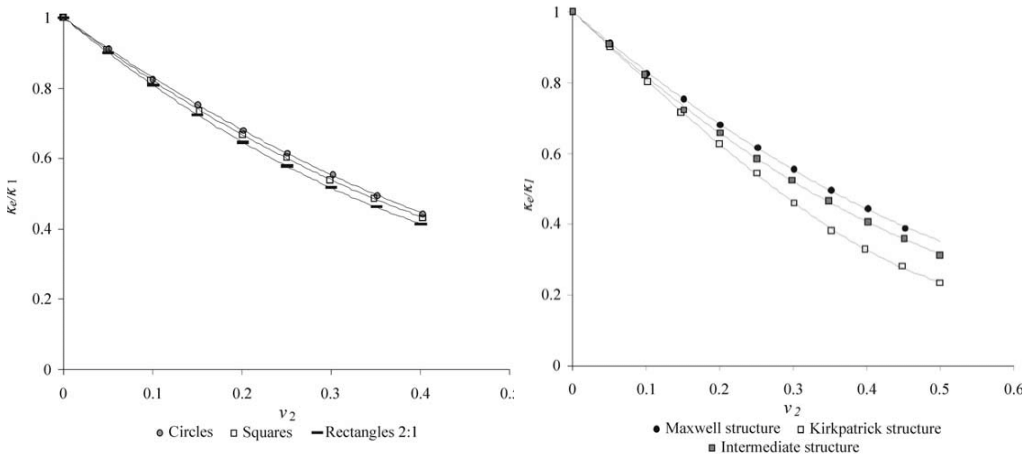

(a) (b)

FIGURE 18: Normalized thermal conductivity of a porous material as a function of inclusion volume fraction: (a) effect of inclusion shape, (b) interaction between inclusions (Carson *et al.* 2003).

Tang *et al.* (2012) also propose a Finite Element model to find the effective conductivity of concrete with conductive aggregates. They conclude that effective thermal conductivity very strongly depends on the degree of heterogeneity, i.e. it is greatly influenced by the difference between the mortar and aggregate individual conductivities. Fig. 19 shows the influence of the homogeneity index m on the effective property. The heat flux vector of a heterogeneous concrete ($m = 1.2$) is more disordered than that of a homogeneous one ($m = 30$). This suggests that low conductivity elements (cracks, pores, inclusions) in the concrete form a thermal barrier preventing heat flow through the matrix. Wu and Wriggers (2014) numerically studied the debonding of hardened cement paste (HCP) and aggregates at interfacial transition zone (ITZ) of a concrete. During the study they observed that, under uniaxial tensile load at constant temperature there is a temperature jump across the crack interface (lips) which creates thermal resistance and leads to reduction of thermal flux in the concrete. They conclude saying this reduction of thermal flux contributes to the degradation of the overall conductivity of the concrete. Shen *et al.* (2015) give us a Finite Element model to predict the effective conductivity of a concrete. They note that, due to the occurrence of tensile microcrack, there is a drastic decrease in the effective thermal conductivity. They also observe that, even though the RVE is initially isotropic, the effective conductivity is anisotropic after crack formation. Fig. 20 shows the thermal conductivity of a concrete specimen subjected to tensile displacement. The aggregate and mortar start to separate from each other and microcracks are formed. When air flows into the cracks, it forms an interfacial thermal resistance, which reduces the matrix conductivity and in turn the effective conductivity.

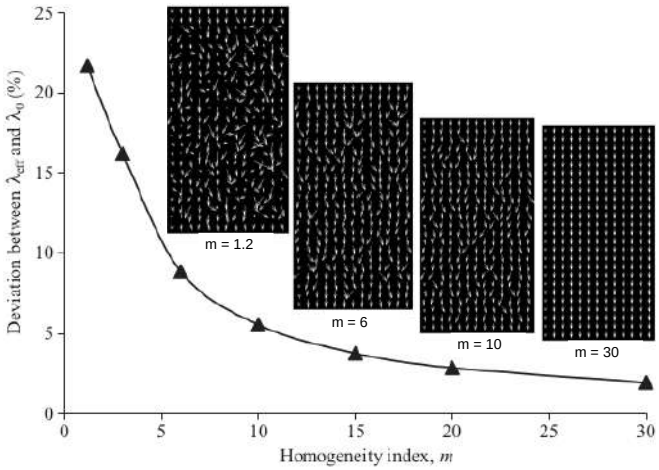

Figure 19: Deviation between the effective conductivity and mortar conductivity vs homogeneity index, and corresponding heat flux vectors (Tang *et al.* 2012).

Nguyen *et al.* (2017) suggests a pattern-based method (PBM) with FEM to determine the overall properties of heterogeneous materials. The PBM uses morphologically representative pattern (MRP) instead of the unit cell or entire RVE. This method allows one to simulate a single crack instead of a family of cracks, thus saving a lot of computational time. The procedure to determine the effective properties of a heterogeneous

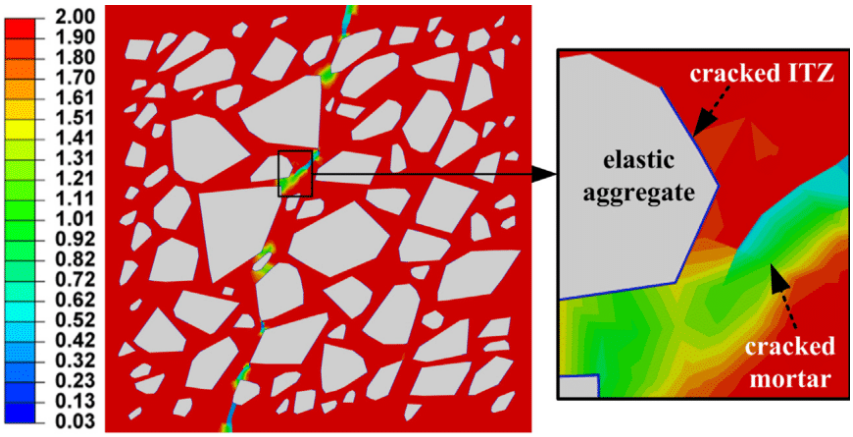

FIGURE 20: Thermal conductivity of cracked concrete specimen (Shen *et al.* 2015).

(or microcracked) media described by an MRP is similar to the Eshelby approach. This involves embedding the MRP inside an infinite medium and applying uniform boundary condition at infinity to find the local properties and inturn the average macroscopic quantities. Though the MRP contains only one crack, the boundary condition can be changed to account for the interaction. Nguyen *et al.* studies the effective conductivity of microcraked media for various crack density, spatial distribution and conductive/non conductive cracks. Fig. 21a shows the effect of crack conductivity on the temperature jump across the crack radius whereas Fig. 21b gives the numerical effective conductivity for various crack distribution.

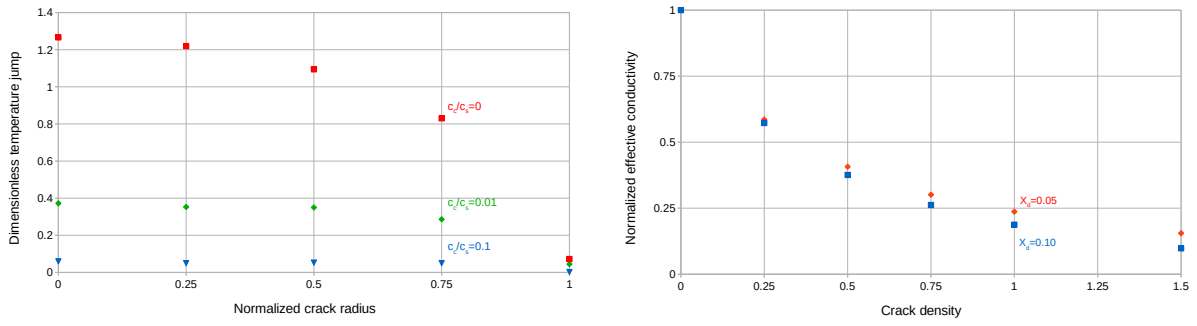

(a) (b)

FIGURE 21: (a) Temperature jump across the crack (b) Numerical effective conductivity from PBM, (Nguyen *et al.* 2017).

Tran *et al.* (2018) presents an alternate semi-analytical method to find the effective conductivity of cracked media. They propose an adaptive model which is obtained by combining the analytical (or theoretical) and numerical (Boundary Element Method) solutions. Fig. 22 shows how the temperature distribution is influenced by the presence of cracks.

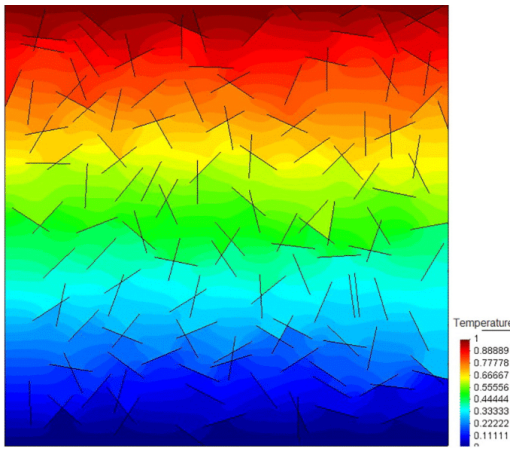

FIGURE 22: Temperature distribution in a 2D microcracked medium (Tran *et al.* 2018).

In the same manner as theory, numerical simulation comes thus in handy and may help to estimate the effective behaviour of materials. In this thesis, the numerical part will include FEM simulations performed within a framework consistent with the theoretical approach. In this way, numerical results can be compared to analytical ones.

Thesis plan

Considering all this previous information into account, the present thesis concentrates on investigating the effective thermomechanical properties of a brittle material both theoretically and numerically. The work starts with the analytical study of the thermal conductivity and resistivity of a brittle microcracked media in steady-state followed by numerical simulation. Once these results are presented, the work moved forward onto the modelling of the thermoelastic properties of the said media. And finally, results are compared and conclusions are drawn. The thesis is organized with each chapter corresponding to a published or submitted research paper.

- Chapter 1 [C. R. Mecanique; 347: 944–952 (2019)] provides the effective thermal properties of a 3D microcracked media under the steady-state condition. The medium considered is initially isotropic and has families of randomly oriented cracks. The main focus will be on the unilateral effect. Influenced by Deudé *et al.* (2002) the closed cracks are considered to be a fictitious isotropic material. Using classical Eshelby-like approach, closed-form expressions for various schemes (interacting and non-interacting cracks) are given.

- Chapter 2 [Mechanics & Industry; 21: 519 (2020)] gives the effective thermal conductivity for a 2D microcracked media. The medium is assumed to be initially isotopic and weakened by a single-family of parallel cracks. The theoretical method uses various estimates to provide closed-form expressions. The numerical method involves FE simulations performed in ABAQUS to compare with the micromechanical results.

- Chapter 3 [Euro. J. Mech. A/Solids; (2020); submitted] presents the effective thermoelastic properties of a 3D microcracked media. Using classical strain and stress based boundary conditions, the overall thermal stress and strain tensors and specific heat capacities at constant strain and stress are found. Special attention is paid to crack induced anisotropy and unilateral effect.

- Chapter 4 holds the collection of the simulations performed. This includes 3D FE simulations of conductivity, resistivity and thermoelasticity. The simulations investigate the influence of crack orientation, size, and crack status (open/closed). Thus obtained results are compared to the theory.

Finally, conclusions are drawn summarizing the main observations from the theoretical and numerical approaches. Future perspectives of this work and its relevancy in creating a new damage model are discussed.

The appendices have exhaustive details on the theoretical developments performed during the duration of the thesis.

Chapter 1

Homogenized thermal conduction properties in 3D

Abstract

This chapter intends to provide effective thermal properties related to the conduction problem in 3D taking into account the unilateral effect (opening/closure of cracks). This analysis considers steady-state heat transfer within an initially isotropic media weakened by randomly oriented crack families. Eshelby's equivalent inclusion method in steady-state discussed earlier is implemented. According to boundary conditions, estimates and bounds based on Eshelby-like formalism are developed to derive closed-form expressions for effective thermal conductivity and resistivity at fixed microcracking state. The open cracks are considered non-conductive whereas, the closed cracks are fictitious isotropic conductive material. The effective properties are determined for dilute and Mori-Tanaka schemes, and Ponte Castañeda-Willis bound. Influence of crack orientation and variation of crack density are also explored.

Present chapter is based to the published research paper (Rangasamy Mahendren et al. 2019) [C. R. Mecanique; 347: 944–952 (2019)].
Some elements have been added to provide a more complete overview to the theoretical background.
A self-consistent notation is adopted.

1.1 Introduction

Homogenization is a useful tool for the modelling and analysis of the behaviour of heterogeneous materials. One of its main objectives is to estimate their overall properties from their microstructural features (phase properties, inclusions distribution and geometry, ...). This topic is even more interesting when there is a lack of experimental data. Several studies have been dedicated to the micromechanical analysis of microcracked media, especially to address their elastic behaviour (for instance Kachanov 1993, Nemat-Nasser and Hori 1993, Ponte Castañeda and Willis 1995 for initially isotropic materials). Still, many practical applications require proper modelling of other properties such as thermal, transport and piezoelectric properties which are not investigated much (Dormieux *et al.* 2006, Sevostianov and Kachanov 2019, Su *et al.* 2008, Wang and Jiang 2003, Giraud *et al.* 2007).

Taking into account the unilateral effect (opening and closure of cracks) makes the estimation of said effective properties challenging, and this even more as microcracks are oriented defects. Some authors have investigated the elastic problem taking into account both the induced anisotropy and recovery phenomenon due to cracks closure, through averaging up-scaling methods (Kachanov 1993, Andrieux *et al.* 1986, Deudé *et al.* 2002, Dormieux and Kondo 2009). Such modelling strategy has never been applied before for a steady state heat conduction problem. So, in this work, we intend to address this issue through Eshelby-like approach and derive effective thermal properties of microcracked media focusing mainly on the unilateral effect.

1.2 Theoretical Framework of the thermal conduction problem

Since a lot of studies have presented the homogenization of elastic behaviour, the thesis would like to recall the conduction behaviour. Assuming length scale separation, this study deals with continuum micromechanics. Homogenization process providing microstructure-properties relationships is conducted through the mean-field theory. Present developments for effective thermal properties are inspired by the mathematical analogy between elasticity and steady-state heat conduction problems (Hashin 1983, Torquato 2002):

$$\begin{aligned}
\text{stress } \boldsymbol{\sigma} &\iff \text{heat flux } q \\
\text{strain } \boldsymbol{\varepsilon} &\iff \text{temperature gradient } g \\
\text{stiffness } \mathbb{C} &\iff \text{thermal conductivity } \boldsymbol{\lambda} \\
\text{compliance } \mathbb{S} &\iff \text{thermal resistivity } \boldsymbol{\rho} \\
\text{Hooke's law} &\iff \text{Fourier's law}
\end{aligned}$$

Let consider Ω the volume of the RVE of a heterogeneous material, $\partial\Omega$ the external surface and $\mathbf{u}$ the outward unit normal to $\partial\Omega$. The macroscopic thermal gradient G can be defined as mean temperature on the external surface $\partial\Omega$:

$$G = \frac{1}{|\Omega|}\int_{\partial\Omega} T(x)\ \mathbf{u}(x)\ d\Omega \qquad \text{and} \qquad Q = \frac{1}{|\Omega|}\int_{\partial\Omega} q(x)\cdot\mathbf{u}(x)\ x\ d\Omega \tag{1.1}$$

with $T(x)$ and $q(x)$ the local temperature and local heat density at any point x of Ω respectively. Using divergence theorem, under stationary thermal conditions, the macroscopic quantities correspond to the average of its respective microscopic quantities (Valès *et al.* 2016):

$$G = \frac{1}{|\Omega|}\int_{\Omega} g(x)\ d\Omega = \langle g\rangle \qquad \text{and} \qquad Q = \frac{1}{|\Omega|}\int_{\Omega} q(x)\ d\Omega = \langle q\rangle \tag{1.2}$$

with $g(x)$ the local temperature gradient at any point x at Ω.

Let say the RVE has two phases ($r = \{m, i\}$), matrix (m) and inclusion (i) and their volume fractions are given as f_m and f_i respectively. Such a media exhibits a matrix-inclusion typology in which each phase are supposed to exhibit a homogeneous behaviour and follows the Fourier's law:

$$q(x) = -\boldsymbol{\lambda}(x)\cdot g(x) \qquad \text{and} \qquad g(x) = -\boldsymbol{\rho}(x)\cdot q(x) \qquad \forall\ x\ \in\Omega \tag{1.3}$$

with

$$\boldsymbol{\lambda}(x) = \begin{cases} \boldsymbol{\lambda}_m, & \forall\ x\in\Omega_m \\ \boldsymbol{\lambda}_i, & \forall\ x\in\Omega_i \end{cases} \quad \boldsymbol{\rho}(x) = \begin{cases} \boldsymbol{\rho}_m, & \forall\ x\in\Omega_m \\ \boldsymbol{\rho}_i, & \forall\ x\in\Omega_i \end{cases}, \ \Omega_m\cup\Omega_i = \Omega,\ \Omega_m\cap\Omega_i = \varnothing \tag{1.4}$$

where $\boldsymbol{\lambda}_m$ and $\boldsymbol{\rho}_m = \boldsymbol{\lambda}_m^{-1}$ denote the matrix thermal conductivity and resistivity with volume Ω_m, $\boldsymbol{\lambda}_i$ and $\boldsymbol{\rho}_i = \boldsymbol{\lambda}_i^{-1}$ denote the inclusion thermal conductivity and resistivity with volume Ω_i. Two different boundary conditions can be imposed at the outer boundary $\delta\Omega$ of the RVE, i.e. either uniform macroscopic temperature gradient (G imposed at $\delta\Omega$) or uniform macroscopic heat flux (Q imposed at $\delta\Omega$). Assuming an initial natural state, the microscopic and macroscopic quantities can be linked linearly as (Hill 1963):

$$g(x) = \mathbf{A}(x)\cdot G \quad \text{and} \quad q(x) = \mathbf{B}(x)\cdot Q \qquad \forall\ x\in\Omega \tag{1.5}$$

where $\mathbf{A}$ (resp. $\mathbf{B}$) is the second order gradient localization (resp. flux concentration) tensor such that $\langle\mathbf{A}\rangle = \langle\mathbf{B}\rangle = \mathbf{I}$ ($\mathbf{I}$ being the second order identity tensor). Average temperature gradient G and heat flux Q of the heterogeneous media as obtained by Eq. (1.2) can thus be related by effective thermal tensors:

$$Q = \langle q\rangle = -\langle\boldsymbol{\lambda}\cdot g\rangle = -\langle\boldsymbol{\lambda}\cdot\mathbf{A}\cdot G\rangle = -\langle\boldsymbol{\lambda}\cdot\mathbf{A}\rangle\cdot G = -\boldsymbol{\lambda}_{hom}\cdot G \tag{1.6}$$

$$G = \langle g \rangle = -\langle \boldsymbol{\rho} \cdot q \rangle = -\langle \boldsymbol{\rho} \cdot \mathbf{B} \cdot Q \rangle = -\langle \boldsymbol{\rho} \cdot \mathbf{B} \rangle \cdot Q = -\boldsymbol{\rho}_{hom} \cdot Q \tag{1.7}$$

where $\boldsymbol{\lambda}_{hom}$ and $\boldsymbol{\rho}_{hom}$ are the effective thermal conductivity and resistivity tensors respectively. Since each phase is considered homogeneous, the effective tensors can be simplified as:

$$\boldsymbol{\lambda}_{hom} = \langle \boldsymbol{\lambda} \cdot \mathbf{A} \rangle = \sum_r f_r \ \boldsymbol{\lambda}_r \cdot \langle \mathbf{A} \rangle_r \qquad \text{with } \langle \mathbf{A} \rangle = \sum_r f_r \ \langle \mathbf{A} \rangle_r = \mathbf{I} \tag{1.8}$$

$$\boldsymbol{\rho}_{hom} = \langle \boldsymbol{\rho} \cdot \mathbf{B} \rangle = \sum_r f_r \ \boldsymbol{\rho}_r \cdot \langle \mathbf{B} \rangle_r \qquad \text{with } \langle \mathbf{B} \rangle = \sum_r f_r \ \langle \mathbf{B} \rangle_r = \mathbf{I} \tag{1.9}$$

where operator $\langle \cdot \rangle_r = \frac{1}{|\Omega_r|} \int_{\Omega_r} \cdot \, d\Omega$ is the average value over the volume of the phase r. Further development of the above equations give:

$$\boldsymbol{\lambda}_{hom} = \boldsymbol{\lambda}_m + f_i \ (\boldsymbol{\lambda}_i - \boldsymbol{\lambda}_m) \cdot \langle \mathbf{A} \rangle_i \quad \text{and} \quad \boldsymbol{\rho}_{hom} = \boldsymbol{\rho}_m + f_i \ (\boldsymbol{\rho}_i - \boldsymbol{\rho}_m) \cdot \langle \mathbf{B} \rangle_i \tag{1.10}$$

The mean localization tensors help us establish the link between the mean temperature gradient per phase and the macroscopic quantity:

$$\langle g \rangle_r = \langle \mathbf{A} \rangle_r \cdot G \qquad \text{and} \qquad \langle q \rangle_r = \langle \mathbf{B} \rangle_r \cdot Q \tag{1.11}$$

From these expressions, knowing the localization tensor $\langle \mathbf{A} \rangle_r$ and concentration tensor $\langle \mathbf{B} \rangle_r$ is enough to solve for the effective conductivity and resistivity respectively. But for this, we need to find the local heat flux q, temperature gradient g and temperature T fields to solve the following problem on the RVE, either (Torquato 2002):

$$\begin{cases} q(x) & = -\boldsymbol{\lambda}(x) \cdot g(x), \quad \forall \ x \in \Omega \\ div \ q & = 0 \\ g(x) & = grad \ T(x) \\ T(x) & = G \cdot x, \quad \forall \ x \in \partial\Omega \end{cases} \quad \text{or} \quad \begin{cases} g(x) & = -\boldsymbol{\rho}(x) \cdot q(x), \quad \forall \ x \in \Omega \\ div \ q & = 0 \\ g(x) & = grad \ T(x) \\ q(x) & = Q, \quad \forall \ x \in \partial\Omega \end{cases} \tag{1.12}$$

Left part of Eq. (1.12) corresponds to uniform temperature gradient (G) boundary conditions whereas right part is related to uniform flux (Q) conditions. The solution for (q, g) is neither unique nor easy due to the lack of thermal and geometric description of the heterogeneous materials. To address this difficulty, two approaches are possible: (1) to explore and find a range of possible solutions (bound methods like Voigt and Reuss), (2) to make additional assumptions on the microstructure of the RVE to deduce expressions for q and g (estimation methods). Works on the single-inhomogeneity problem, initiated by Eshelby (1957) in elasticity and extended to thermoelasticity (Berryman 1997, Torquato 2002) and to steady-state (Hatta and Taya 1986, see detailed explanation in Appendix A.1), provides some solutions for such issue if the inclusions are ellipsoidal. Indeed, the temperature gradient and heat flux local fields in the crack can be approximated by the

uniform respective local fields obtained in an ellipsoid embedded in an infinite matrix subjected to uniform boundary conditions denoted as G_∞ and Q_∞. Assuming perfect interfaces, several representations can be developed according to remote conditions, matrix properties, phases volume fractions, and geometry and properties of the inhomogeneity.

Now in line with the thesis, consider a 3D RVE with N number of crack families. Let denote $\boldsymbol{\lambda}_{c,j}$ and $\boldsymbol{\rho}_{c,j} = \boldsymbol{\lambda}_{c,j}^{-1}$ the conductivity and resistivity of the j^{th} $(j = 1...N)$ family of parallel cracks and $f_{c,j}$ their volume fraction. Eq. (1.10) for this microcracked media becomes:

$$\boldsymbol{\lambda}_{hom} = \boldsymbol{\lambda}_m + \sum_{j=1}^{N} f_{c,j} \, (\boldsymbol{\lambda}_{c,j} - \boldsymbol{\lambda}_m) \cdot \langle \mathbf{A} \rangle_{c,j} \tag{1.13}$$

$$\boldsymbol{\rho}_{hom} = \boldsymbol{\rho}_m + \sum_{j=1}^{N} f_{c,j} \, (\boldsymbol{\rho}_{c,j} - \boldsymbol{\rho}_m) \cdot \langle \mathbf{B} \rangle_{c,j} \tag{1.14}$$

where phase r for $r = \{m, c_j\}$. At this point, effective tensors $\boldsymbol{\lambda}_{hom}$ (directly derived from uniform gradient-based boundary conditions) and $\boldsymbol{\rho}_{hom}$ (naturally obtained from uniform flux-based boundary conditions) strictly describe the same equivalent homogeneous media, so that these tensors are inverse of each other, i.e. $\boldsymbol{\lambda}_{hom} = \boldsymbol{\rho}_{hom}^{-1}$.

(a) (b)

FIGURE 1.1: (a) RVE with arbitrarily oriented microcracks, (b) penny-shaped crack geometry.

For the present case, the RVE is composed of an initially isotropic homogeneous media, considered as the matrix. Its thermal conductivity and resistivity tensors are given by $\boldsymbol{\lambda}_m = \lambda_m \, \mathbf{I}$ and $\boldsymbol{\rho}_m = \rho_m \, \mathbf{I}$ (λ_m and ρ_m are the scalar thermal conductivity and resistivity, with $\lambda_m = \rho_m^{-1}$) respectively. This matrix is weakened by randomly distributed microcracks with arbitrary orientations (Fig. 1.1a). A convenient way to represent such kind of defect is in the form of a flat oblate ellipsoid (mean semi-axes a and c, Fig. 1.1b). For the j^{th} family of parallel microcracks, $\mathbf{n}_j$ denotes their unit vector, $\omega_j = {}^{c_j}/_{a_j}$ their mean aspect ratio and $d_j = \mathcal{N}_j \, a_j^3$ their scalar crack density parameter ($\mathcal{N}_j$ is the number of cracks in the j^{th} family per unit volume, Budiansky and O'Connell 1976). Crack volume fraction comes thus to $f_{c,j} = \frac{4}{3} \, \pi d_j \omega_j$ (Appendix A.2). Under these assumptions, estimated solutions for localization and concentration tensors $\langle \mathbf{A} \rangle_{c,j}^{est}$ and $\langle \mathbf{B} \rangle_{c,j}^{est}$ depend on the following depolarization tensor $\mathbf{S}_j^E$ (similar to the Eshelby tensor of elastic problems)

(Hatta and Taya 1986, see Appendix A.3):

$$\mathbf{S}_j^E \;=\; \left(1-\frac{\pi}{2}\omega_j\right)\mathbf{n}_j\otimes\mathbf{n}_j \;+\; \frac{\pi}{4}\omega_j\,\left(\mathbf{I}-\mathbf{n}_j\otimes\mathbf{n}_j\right) \tag{1.15}$$

Last important points for the considered problem deal with the geometry and properties of the cracks. Regarding the former, the configuration of penny-shaped cracks corresponds to the limit case $\omega_j \to 0$ that must be introduced at the very end of mathematical developments. Moreover, the fact that microcracks can be either open or closed according to compressive loads is introduced through the latter point. In both cases, cracks are assumed to be isotropic ($\boldsymbol{\lambda}_{c,j} = \lambda_{c,j}\ \mathbf{I}$ and $\boldsymbol{\rho}_{c,j} = \rho_{c,j}\ \mathbf{I}$) but they behave differently depending upon the state of the microcrack:

- for the open case, $\lambda_{c,j} = 0$ and $\rho_{c,j} \to \infty$, which corresponds to adiabatic conditions on the cracks lips,
- following the works of Deudé *et al.* (2002), closed cracks are represented by a fictitious isotropic material with scalar conductivity $\lambda_{c,j} = \lambda^*$ and resistivity $\rho_{c,j} = \rho^*$, which accounts for some heat transfer continuity at the closure of cracks (friction-less contact). Taking $\lambda^* = \lambda_m$ and $\rho^* = \rho_m$ may seem natural, but we will nevertheless continue the development for a general case where λ^* and ρ^* are scalars with a condition $\lambda^* \neq 0$ and $\rho^* \not\to \infty$.

1.3 Gradient-based formulation

By gradient-based formulation, we mean to impose a uniform macroscopic temperature gradient G at the outer boundary $\delta\Omega$ of the RVE. Such a situation corresponds to the classical strain-based condition of the Eshelby's problem. Let us consider three different approaches to derive the effective properties.

1.3.1 Dilute scheme

In a first approach, we are going to estimate the homogenized properties assuming a dilute density of cracks, which is to consider no interaction between defects. Remote conditions on the Eshelby problem come in that case to the macroscopic gradient ($G_\infty = G$, Fig. 1.2a). Hence, the gradient localization tensor is given by:

$$\langle\mathbf{A}\rangle_{c,j}^{dil} = \left[\mathbf{I} + \mathbf{P}_j^E\cdot\left(\boldsymbol{\lambda}_{c,j}-\boldsymbol{\lambda}_m\right)\right]^{-1} \tag{1.16}$$

where $\mathbf{P}_j^E = \mathbf{S}_j^E\cdot\boldsymbol{\rho}_m$ is the symmetric second order interaction tensor (equivalent to the first Hill tensor in elasticity). Eq. (1.16) can be simplified as:

$$\langle\mathbf{A}\rangle_{c,j}^{dil} = \left[\mathbf{I}-\left(1-\xi_j\right)\mathbf{S}_j^E\right]^{-1} \quad \text{with} \quad \xi_j = \frac{\lambda_{c,j}}{\lambda_m} \tag{1.17}$$

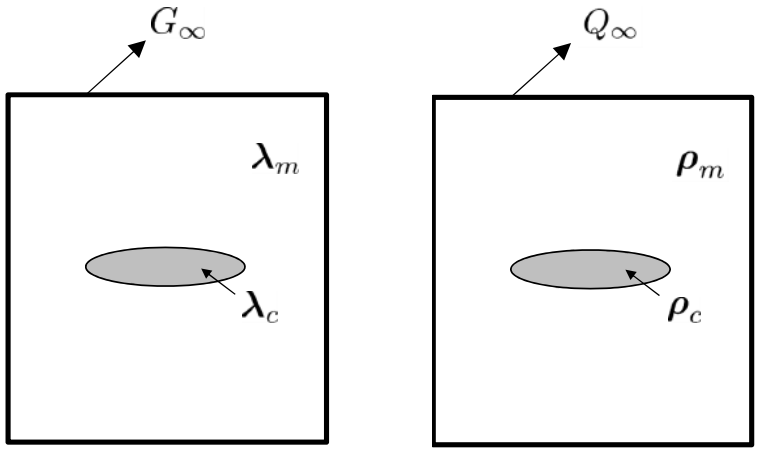

FIGURE 1.2: Phase properties and boundary conditions at infinity: (a) imposed temperature gradient G_∞, (b) imposed heat flux Q_∞.

Eq. (1.13) thus comes to:

$$\boldsymbol{\lambda}_{hom}^{dil} = \lambda_m \left[\mathbf{I} - \frac{4}{3}\pi \sum_{j=1}^{N} d_j\, \omega_j \left(1-\xi_j\right) \langle \mathbf{A} \rangle_{c,j}^{dil} \right] \tag{1.18}$$

We can see that the $\boldsymbol{\lambda}_{hom}^{dil}$ depends on the aspect ratio ω_j in our case. However, we show that the quantity $\omega_j \left(1-\xi_j\right) \langle \mathbf{A} \rangle_{c,i}^{dil}$ tends to a limit $\mathbf{T}_j$ when $\omega_j \to 0$, so:

$$\boldsymbol{\lambda}_{hom}^{dil} = \boldsymbol{\lambda}_m \cdot \left[\mathbf{I} - \frac{4}{3}\pi \sum_{j=1}^{N} d_j\, \mathbf{T}_j \right] \quad \text{with } \mathbf{T}_j = \lim_{\omega_j \to\, 0} \omega_j \left(1-\xi_j\right) \left[\mathbf{I} - \mathbf{S}_{E,j} \left(1-\xi_j\right) \right]^{-1} \tag{1.19}$$

Such expansion includes both crack configurations, i.e. for open cracks $\lambda_{c,j} = 0$, so $\xi_j = 0$ while for closed cracks $\lambda_{c,j} = \lambda^* \neq 0$, so $\xi_j \neq 0$. Taking this into account, tensor $\mathbf{T}_j$ for the j^{th} family of cracks is given by:

$$\mathbf{T}_j = \begin{cases} \dfrac{2}{\pi}\, \mathbf{n}_j \otimes \mathbf{n}_j & \text{, if cracks are open} \\ \mathbf{0} & \text{, if cracks are closed} \end{cases} \tag{1.20}$$

Accordingly, Eq. (1.19) can be simplified in:

$$\boldsymbol{\lambda}_{hom}^{dil} = \boldsymbol{\lambda}_m \cdot \left[\mathbf{I} - \frac{8}{3} \sum_{j/open} d_j\, \mathbf{n}_j \otimes \mathbf{n}_j \right] \tag{1.21}$$

in which only open cracks contribute in an additive manner. As an example, the effective thermal conductivity of a media weakened by a single family of parallel microcracks with

unit normal $\mathbf{n}$ and density d takes the form:

$$\boldsymbol{\lambda}_{hom}^{dil} = \begin{cases} \boldsymbol{\lambda}_m - \dfrac{8}{3}\, d\, \lambda_m\, \mathbf{n} \otimes \mathbf{n} & \text{, if cracks are open} \\ \boldsymbol{\lambda}_m & \text{, if cracks are closed} \end{cases} \tag{1.22}$$

Detailed development for a single family of crack in dilute case can be found in Appendix A.5.1.

1.3.2 Mori-Tanaka scheme

In line with Eshelby-like approach, the Mori-Tanaka (MT) scheme (Mori and Tanaka 1973) considers cracks embedded in an infinite media (with matrix properties) that is subjected to the average temperature gradient over the matrix phase ($G_\infty = \langle g \rangle_m$, Fig. 1.2a). Introducing inhomogeneities inside a thermally-stressed matrix in this way amounts to account for some interactions between cracks. Averaging rule Eq. (1.2) leads to the following localization tensor:

$$\langle \mathbf{A} \rangle_{c,j}^{MT} = \langle \mathbf{A} \rangle_{c,j}^{dil} \cdot \left[f_m\, \mathbf{I} + \sum_{k=1}^{N} f_{c,k}\, \langle \mathbf{A} \rangle_{c,k}^{dil} \right]^{-1} \tag{1.23}$$

Now Eq. (1.13) can be written as:

$$\boldsymbol{\lambda}_{hom}^{MT} = \boldsymbol{\lambda}_m \cdot \left[\mathbf{I} + \frac{4}{3}\pi \sum_{j=1}^{N} d_j\, \mathbf{T}_j \right]^{-1} = \boldsymbol{\lambda}_m \cdot \left[\mathbf{I} + \frac{8}{3} \sum_{j/open} d_j\, \mathbf{n}_j \otimes \mathbf{n}_j \right]^{-1} \tag{1.24}$$

since $\lim\limits_{\omega_j \to\, 0} \omega_j \left[\mathbf{I} - \mathbf{S}_{E,j}\, \left(1 - \xi_j\right) \right]^{-1} = \mathbf{T}_j$ also. Accordingly, the specific conduction behaviour for the simple case of a single family of parallel microcracks according to their status described is as follows (see Appendix A.5.2):

$$\boldsymbol{\lambda}_{hom}^{MT} = \begin{cases} \boldsymbol{\lambda}_m - \dfrac{8}{3}\, d\, \lambda_m \dfrac{1}{1 + \frac{8d}{3}}\, \mathbf{n} \otimes \mathbf{n} & \text{, if cracks are open} \\ \boldsymbol{\lambda}_m & \text{, if cracks are closed} \end{cases} \tag{1.25}$$

1.3.3 Ponte Castañeda–Willis upper bound

Based on the Hashin-Shtrikman bounds (Hashin and Shtrikman 1963), Ponte Castañeda and Willis (PCW) derived explicit strain-based bounds for the effective stiffness of composite materials with ellipsoidal inclusions (Ponte Castañeda and Willis 1995).Their estimate corresponds to a rigorous upper bound for the class of cracked media in which the matrix is the stiffest phase. The PCW formulation separately accounts for the inclusion shape and spatial distribution respectively through fourth order interaction $\mathbb{P}_j^E$ and spatial crack distribution $\mathbb{P}_c^d$ tensors. Using a similar approach for the thermal problem with a second

order spatial distribution tensor $\mathbf{P}_c^d$, the effective conductivity can be given by:

$$\boldsymbol{\lambda}_{hom}^{PCW} = \boldsymbol{\lambda}_m + \left(\mathbf{I} - \sum_{i=1}^{N} f_{c,j} \left[\left(\boldsymbol{\lambda}_{c,j} - \boldsymbol{\lambda}_m \right)^{-1} + \mathbf{P}_j^E \right]^{-1} \cdot \mathbf{P}_c^d \right)^{-1} \cdot \left(\sum_{j=1}^{N} f_{c,j} \left[\left(\boldsymbol{\lambda}_{c,j} - \boldsymbol{\lambda}_m \right)^{-1} + \mathbf{P}_j^E \right]^{-1} \right) \tag{1.26}$$

It is also convenient to observe that:

$$\boldsymbol{\lambda}_{hom}^{PCW} = \boldsymbol{\lambda}_m \cdot \left(\mathbf{I} + \sum_{j=1}^{N} f_{c,j} \, \mathbf{M}_{c,j} \cdot \boldsymbol{\lambda}_m \cdot \mathbf{P}_c^d \cdot \boldsymbol{\lambda}_m \right)^{-1} \cdot \left(\mathbf{I} - \sum_{j=1}^{N} f_{c,i} \, \mathbf{M}_{c,j} \cdot \mathbf{Q}_c^d \right) \tag{1.27}$$

where $\mathbf{M}_{c,j} = \left[\left(\boldsymbol{\rho}_{c,j} - \boldsymbol{\rho}_m \right)^{-1} + \mathbf{Q}_j^E \right]^{-1}$, $\mathbf{Q}_j^E = \boldsymbol{\lambda}_m \cdot \left(\mathbf{I} - \mathbf{P}_j^E \cdot \boldsymbol{\lambda}_m \right)$ (equivalent to the second Hill tensor in elasticity) and $\mathbf{Q}_c^d = \boldsymbol{\lambda}_m \cdot \left(\mathbf{I} - \mathbf{P}_c^d \cdot \boldsymbol{\lambda}_m \right)$. For simplicity, a spherical spatial distribution is adopted in this study, for which $\mathbf{P}_c^d$ reads:

$$\mathbf{P}_c^d = \frac{1}{3} \, \boldsymbol{\rho_m} \tag{1.28}$$

Even though, the PCW formulation is derived from the energy approach, Eq. (1.26) can be interpreted in the form of Eq. (1.13) through the following localization tensor:

$$\langle \mathbf{A} \rangle_{c,j}^{PCW} = \langle \mathbf{A} \rangle_{c,j}^{dil} \cdot \left(f_m \, \mathbf{I} + \sum_{k=1}^{N} f_{c,k} \left[\mathbf{I} + \left(\mathbf{P}_k^E - \mathbf{P}_c^d \right) \cdot \left(\boldsymbol{\lambda}_{c,k} - \boldsymbol{\lambda}_m \right) \right] \cdot \langle \mathbf{A} \rangle_{c,k}^{dil} \right)^{-1} \tag{1.29}$$

As already emphasized by Ponte Castañeda and Willis, it can be observed that when $\mathbf{P}_c^d = \mathbf{P}_j^E$, the PCW scheme corresponds to the Mori-Tanaka estimate (Eq. (1.29) comes to Eq. (1.23)) while the case $\mathbf{P}_c^d = \mathbf{0}$ leads to the dilute approximation (Eq. (1.29) reduces to Eq. (1.16)).

Taking into account Eqs. (1.26) and (1.27), or equivalently Eqs. (1.29) and (1.13), the corresponding effective conductivity reads:

$$\boldsymbol{\lambda}_{hom}^{PCW} = \boldsymbol{\lambda}_m \cdot \left[\mathbf{I} - \left(\frac{4}{3} \, \pi \sum_{j=1}^{N} d_i \, \mathbf{T}_j \right) \cdot \left(\mathbf{I} + \frac{4}{9} \, \pi \sum_{j=1}^{N} d_i \, \mathbf{T}_j \right)^{-1} \right] \tag{1.30}$$

Keeping in mind Eq. (1.20), one gets (refer to Appendix A.5.3):

$$\boldsymbol{\lambda}_{hom}^{PCW} = \boldsymbol{\lambda}_m \cdot \left[\mathbf{I} - \left(\frac{8}{3} \sum_{j/open} d_j \, \mathbf{n}_j \otimes \mathbf{n}_j \right) \cdot \left(\mathbf{I} + \frac{8}{9} \sum_{j/open} d_j \, \mathbf{n}_j \otimes \mathbf{n}_j \right)^{-1} \right] \tag{1.31}$$

which reduces to:

$$\boldsymbol{\lambda}_{hom}^{PCW} = \begin{cases} \boldsymbol{\lambda}_m - \dfrac{8}{3}\, d\, \lambda_m \dfrac{1}{1+\frac{8d}{9}}\, \mathbf{n}\otimes\mathbf{n} & \text{, if cracks are open} \\ \boldsymbol{\lambda}_m & \text{, if cracks are closed} \end{cases} \tag{1.32}$$

for a single family of parallel microcracks. Note that MT (Eq. (1.25)) and PCW (Eq. (1.32)) tend to dilute prediction (Eq. (1.22)) when $d \to 0$.

1.4 Flux-based formulation

This section considers uniform macroscopic heat flux Q at $\delta\Omega$. Estimates and bound are based on the local fields of cracks embedded inside a matrix subjected to uniform heat flux at infinity (Q_∞). Accordingly, the temperature gradient $g(x)$ tends to $\boldsymbol{\rho}_m \cdot Q_\infty$ when $|x| \to \infty$. This, therefore, amounts to the gradient boundary conditions of the Eshelby-like problem that provide the average temperature gradient $\langle g \rangle_c$ over the cracks volume. From the average heat flux in this phase $\langle q \rangle_c = \boldsymbol{\lambda}_c \cdot \langle g \rangle_c$, estimates of tensor $\mathbf{B}$ can be derived.

1.4.1 Dilute Scheme

For the dilute scheme, conditions at infinity correspond to the macroscopic heat flux ($Q_\infty = Q$, Fig. 1.2b). So that:

$$\langle \mathbf{B} \rangle_{c,j}^{dil} = \boldsymbol{\lambda}_{c,j} \cdot \langle \mathbf{A} \rangle_{c,j}^{dil} \cdot \boldsymbol{\rho}_m = \left[\mathbf{I} + \mathbf{Q}_j^E \cdot \left(\boldsymbol{\rho}_{c,j} - \boldsymbol{\rho}_m \right) \right]^{-1} \tag{1.33}$$

Appendix A.6.1 has information regarding this development. Substituting Eq. (1.33) into Eq. (1.14), we get:

$$\boldsymbol{\rho}_{hom}^{dil} = \boldsymbol{\rho}_m \cdot \left[\mathbf{I} + \frac{4}{3}\pi \sum_{j=1}^{N} d_j\, \mathbf{T}_j \right] \tag{1.34}$$

As previously mentioned, Eq. (1.34) accounts for the cracks state. For open cracks, $\rho_{c,j} \to \infty$, so again $\xi_j = 0$, while for closed cracks $\rho_{c,j} = \rho^* \not\to \infty$, so $\xi_j \neq 0$ with related expression of the $\mathbf{T}_j$ tensors provided in Eq. (1.20). Now,

$$\boldsymbol{\rho}_{hom}^{dil} = \boldsymbol{\rho}_m \cdot \left[\mathbf{I} + \frac{8}{3} \sum_{j/open} d_j\, \mathbf{n}_j \otimes \mathbf{n}_j \right] \tag{1.35}$$

Taking this into account, the expression of the effective resistivity tensor for a single family of cracks comes to:

$$\boldsymbol{\rho}_{hom}^{dil} = \begin{cases} \boldsymbol{\rho}_m + \dfrac{8}{3}\, d\, \rho_m\, \mathbf{n}\otimes\mathbf{n} & \text{, if cracks are open} \\ \boldsymbol{\rho}_m & \text{, if cracks are closed} \end{cases} \tag{1.36}$$

It should be noted that, according to the boundary condition, dilute approximation leads to different representation of the thermal behaviour in the open state of cracks, $\boldsymbol{\lambda}_{hom}^{dil} \neq (\boldsymbol{\rho}_{hom}^{dil})^{-1}$. A similar result is obtained in elasticity as well. Yet, effective conductivity and resistivity are obviously inverse of each other for the closed state of cracks, $\boldsymbol{\lambda}_{hom}^{dil} = (\boldsymbol{\rho}_{hom}^{dil})^{-1}$, while in this case strain-based or stress-based formulations of elasticity still remain different (Dormieux and Kondo 2009, Zhu 2006).

1.4.2 Mori-Tanaka scheme

In this case, the remote conditions correspond to the average heat flux over the matrix phase ($Q_\infty = \langle q \rangle_m$, Fig. 1.2b) and again, using the average rule, the flux concentration tensor is given by:

$$\langle \mathbf{B} \rangle_{c,j}^{MT} = \langle \mathbf{B} \rangle_{c,j}^{dil} \cdot \left[f_m \, \mathbf{I} + \sum_{k=1}^{N} f_{c,k} \, \langle \mathbf{B} \rangle_{c,k}^{dil} \right]^{-1} \tag{1.37}$$

Introducing Eq. (1.37) in Eq. (1.14) finally gives:

$$\boldsymbol{\rho}_{hom}^{MT} = \boldsymbol{\rho}_{hom}^{dil} \tag{1.38}$$

From Eqs. (1.24), (1.35) and (1.38), it is clear that the Mori-Tanaka approach leads to the same predictions under gradient or flux conditions (see also Appendix A.6.2), both for open and closed microcracks, i.e. $\boldsymbol{\lambda}_{hom}^{MT} = (\boldsymbol{\rho}_{hom}^{MT})^{-1}$. The same conclusion has been drawn for elastic properties too (Dormieux and Kondo 2009, Zhu 2006).

1.4.3 Ponte Castañeda–Willis lower bound

As inspired by Ponte Castañeda and Willis (1995), Dormieux and Kondo (2009) derived a variational stress-based lower bound for the effective compliance using an energy approach. Similar to this work, the thermal resistivity can thus be given as:

$$\boldsymbol{\rho}_{hom}^{PCW} = \left(\mathbf{I} - \sum_{j=1}^{N} f_{c,j} \, \mathbf{M}_{c,j} \cdot \mathbf{Q}_c^d \right)^{-1} \cdot \left(\mathbf{I} + \sum_{j=1}^{N} f_{c,j} \, \mathbf{M}_{c,j} \cdot \boldsymbol{\lambda}_m \cdot \mathbf{P}_c^d \cdot \boldsymbol{\lambda}_m \right) \cdot \boldsymbol{\rho}_m \tag{1.39}$$

From Eqs. (1.27) and (1.39), we can observe the equivalence between the upper and lower PCW bounds, since $\boldsymbol{\lambda}_{hom}^{PCW} = (\boldsymbol{\rho}_{hom}^{PCW})^{-1}$. As for the gradient-based bound, the above estimate can be interpreted through the following concentration tensor:

$$\langle \mathbf{B} \rangle_{c,j}^{PCW} = \langle \mathbf{B} \rangle_{c,j}^{dil} \cdot \left(f_m \, \mathbf{I} + \sum_{k=1}^{N} f_{c,k} \Big[\mathbf{I} + \left(\mathbf{Q}_k^E - \mathbf{Q}_c^d \right) \cdot \left(\boldsymbol{\rho}_{c,k} - \boldsymbol{\rho}_m \right) \Big] \cdot \langle \mathbf{B} \rangle_{c,k}^{dil} \right)^{-1} \tag{1.40}$$

Taking into account the spatial distribution adopted in Eq. (1.28), the flux-based PCW bound leads to the following effective thermal resistivity (Appendix A.6.3):

$$\boldsymbol{\rho}_{hom}^{PCW} = \left[\mathbf{I} + \left(\frac{4}{3}\pi \sum_{j=1}^{N} d_j \, \mathbf{T}_j\right) \cdot \left(\mathbf{I} - \frac{8}{9}\pi \sum_{j=1}^{N} d_j \, \mathbf{T}_j\right)^{-1}\right] \cdot \boldsymbol{\rho}_m \tag{1.41}$$

After introducing Eq. (1.20), we get:

$$\boldsymbol{\rho}_{hom}^{PCW} = \left[\mathbf{I} + \left(\frac{8}{3} \sum_{j/open} d_j \, \mathbf{n}_j \otimes \mathbf{n}_j\right) \cdot \left(\mathbf{I} - \frac{16}{9} \sum_{j/open} d_j \, \mathbf{n}_j \otimes \mathbf{n}_j\right)^{-1}\right] \cdot \boldsymbol{\rho}_m \tag{1.42}$$

For a single family example considered throughout the study, the above equation comes to:

$$\boldsymbol{\rho}_{hom}^{PCW} = \begin{cases} \boldsymbol{\rho}_m + \dfrac{8}{3} \, d \, \rho_m \dfrac{1}{1 - \frac{16d}{9}} \, \mathbf{n} \otimes \mathbf{n} & \text{, if cracks are open} \\ \boldsymbol{\rho}_m & \text{, if cracks are closed} \end{cases} \tag{1.43}$$

which again tends to dilute case (Eq. (1.36)) for $d \to 0$. Potential equivalences and between the schemes and their results can be seen in Appendix A.7.

1.5 Discussion

We propose to highlight the consequences of microcracks on thermal properties through the case of a matrix with a single family of parallel cracks, for which closed-form expressions of dilute and Mori-Tanaka estimates and variational bounds have been provided in the text.

For the open cracks, we note that the material exhibits a damage-induced anisotropy, irrespective of the scheme or boundary conditions. To be precise, the effective thermal properties are transversely isotropic around axis $\mathbf{n}$ of cracks (see Eqs. (1.22), (1.25) and (1.32) and Eqs. (1.36), (1.38) and (1.43)). Especially, conductivity (respectively resistivity) is mostly degraded (resp. enhanced) along the direction orthogonal to the cracks surface, which is consistent with adiabatic conditions on the cracks lips. As an illustration, Fig. 1.3 presents the rose diagrams of the generalized scalar conductivity $\lambda(\mathbf{v})$ and resistivity $\rho(\mathbf{v})$ in the direction of unit vector $\mathbf{v}$ respectively defined by:

$$\lambda(\mathbf{v}) = \frac{\mathbf{v} \cdot Q}{\mathbf{v} \cdot G} \qquad \text{and} \qquad \rho(\mathbf{v}) = \frac{\mathbf{v} \cdot G}{\mathbf{v} \cdot Q} \tag{1.44}$$

when the material is subjected to uniform temperature gradient $G = G_v \mathbf{v}$ and to uniform flux $Q = Q_v \mathbf{v}$ respectively. Introducing overall conductivity and resistivity tensors thus gives:

$$\lambda(\mathbf{v}) = \mathbf{v} \cdot \boldsymbol{\lambda}_{hom} \cdot \mathbf{v} \qquad \text{and} \qquad \rho(\mathbf{v}) = \mathbf{v} \cdot \boldsymbol{\rho}_{hom} \cdot \mathbf{v} \tag{1.45}$$

On the contrary, we note that closed cracks do not contribute to the degradation or en-

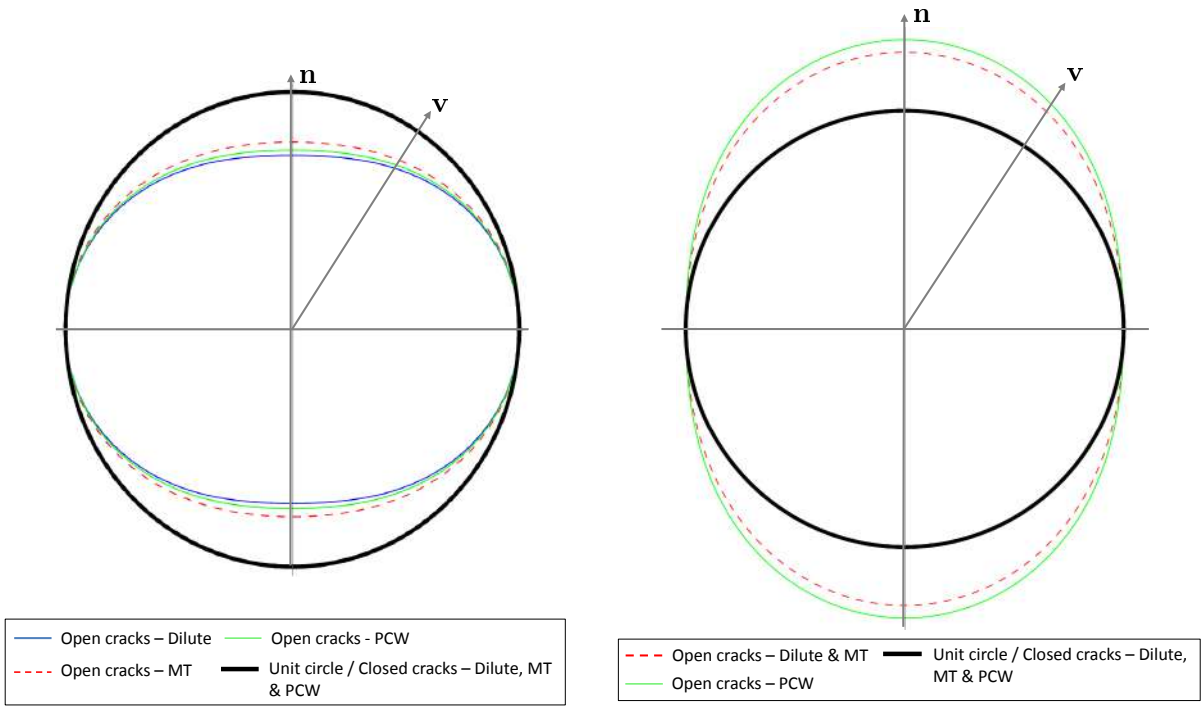

(a) $\dfrac{\lambda(\mathbf{v})}{\lambda_m}$ (b) $\dfrac{\rho(\mathbf{v})}{\rho_m}$

FIGURE 1.3: Generalized thermal conductivity $\lambda(\mathbf{v})$ and resistivity $\rho(\mathbf{v})$ normalized by their initial values for a material weakened by a single family of parallel microcracks of unit normal $\mathbf{n}$ (cracks density $d = 0.1$).

hancement of thermal conduction properties. This result is true regardless of the scheme, boundary conditions, fictitious properties (λ^*, ρ^*) or considered direction $\mathbf{v}$. Indeed, in all cases, effective conductivity and resistivity in any direction recover their initial value (of the virgin material) at the closure of microcracks, i.e.:

$$\lambda(\mathbf{v}) = \lambda_m \quad \text{and} \quad \rho(\mathbf{v}) = \rho_m \ , \quad \forall\ \mathbf{v}, \text{ if cracks are closed} \tag{1.46}$$

This means that the continuity of heat transfer is fully ensured when microcracks are closed, with a conduction response equal to that inside the homogeneous isotropic (virgin) matrix. Such a conclusion clearly differs from the results micromechanically established for elastic properties. Indeed, under frictionless conditions, closure of cracks leads to a partial recovery of mechanical properties. Considering for instance the Young modulus $E(\mathbf{v}) = [\mathbf{v} \otimes \mathbf{v} : \mathbb{S} : \mathbf{v} \otimes \mathbf{v}]^{-1}$ (resp. the elongation modulus $L(\mathbf{v}) = [\mathbf{v} \otimes \mathbf{v} : \mathbb{C} : \mathbf{v} \otimes \mathbf{v}]$) with $\mathbb{S}$ the compliance tensor (resp. $\mathbb{C}$ the stiffness tensor) for a stress-based formulation (resp. for a strain-based formulation), it has been demonstrated that closed cracks do not influence the Young modulus $E(\mathbf{n})$ (resp. the elongation modulus $L(\mathbf{n})$) in the direction $\mathbf{n}$ normal to the cracks but still remain active for others directions (Welemane and Cormery 2002, Goidescu *et al.* 2013). The complete damage deactivation for heat conduction properties can be attributed to the lesser complexity of the problem itself and also to the simple definition of the depolarization tensor. Compared to elastic case, Eshelby-like

tensor $\mathbf{S}^E$ for conduction behaviour (Eq. (1.15)) contains only basic information, as it is of the second order, symmetric and depends only on the aspect ratio ω and orientation $\mathbf{n}$ of the crack (no dependency on the matrix properties like the Eshelby tensor does in the elastic case for instance).

At last, it seems relevant to compare the homogenization estimates according to the microcrack density parameter. Conclusions for the closed state of microcracks are obvious since in all cases thermal properties are not affected by the defects. On the other hand, the open state shows some significant differences between dilute and Mori-Tanaka estimates and PCW variational bounds of conductivity, especially as crack density increases (Fig. 1.4a). Yet, similarly to compliance in elasticity, the Mori-Tanaka formulation coincides with the dilute case for resistivity (Eq. (1.38)). This is due to the combination of both the spatial crack distribution considered by MT (corresponding to Eshelby distribution) and the specific thermal resistivity of open crack ($\rho_c \to \infty$). Such point is confirmed by the evolution of the lower bound established in Dormieux and Kondo (2009) which clearly differs from both previous schemes. Fig. 1.4b illustrates the significant role of interactions in the resistivity prediction.

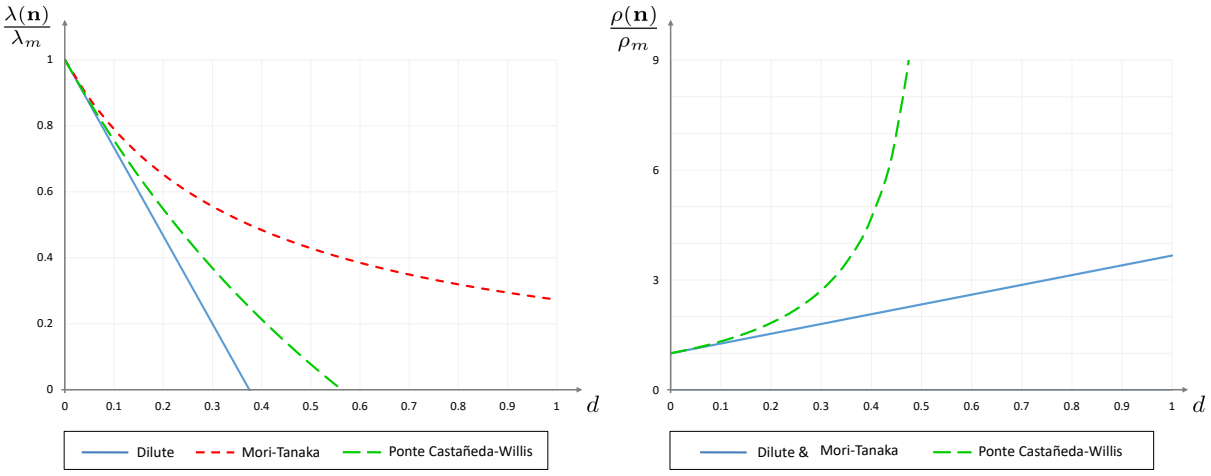

(a) $\frac{\lambda(\mathbf{n})}{\lambda_m}$ (b) $\frac{\rho(\mathbf{n})}{\rho_m}$

FIGURE 1.4: Predictions of homogenization estimates and bounds for the generalized thermal conductivity $\lambda(\mathbf{n})$ and resistivity $\rho(\mathbf{n})$ for a material weakened by a single family of open parallel microcracks of unit normal $\mathbf{n}$.

1.6 Conclusion

In this chapter, the effective conduction properties were analyzed by three different homogenization techniques. Open cracks do have varied influence based on the technique but the properties are always anisotropic (transversely isotropic for a single family of cracks). We also see that the spatial distribution of cracks plays an important role in predicting the behaviour of the microcracked media. Regarding the unilateral behaviour,

results show that the closure of cracks leads to a total deactivation of their effects on the thermal conductivity and resistivity of the material, irrespective of homogenization methods (taking into account or not interactions between microcracks) or boundary conditions. Without experimental data, the choice has been made to compare theoretical results to numerical simulations. This comparison is discussed in the following chapter.

Chapter 2

Thermal conductivity in 2D: theoretical and numerical approaches

Abstract

The objective of this chapter is to compare the effective conductivity of a microcracked media either derived from theoretical or numerical results. For simplicity, the 2D case is considered here. The theoretical approach uses the same Eshelby's equivalent inclusion method used in Chapter 1. Applying a uniform temperature gradient allows for finding the overall conductivity of an isotropic media containing a single family of parallel microcracks. The numerical work uses FEM in ABAQUS to evaluate the same configuration as the theoretical one and allow us to compare with the micromechanical results. Both approaches consider non-conductive open cracks and conductive closed cracks.

Present chapter corresponds to the published research paper (Rangasamy Mahendren et al. 2020a) [Mechanics & Industry; 21: 519 (2020)].
A self-consistent notation is adopted.

2.1 Introduction

Defects have an influence on the macroscopic behaviour of a material, each on a different scale. The overall behaviour of the material can be characterized by its microstructure. This transition from micro-to-macro can be modelled using averaging techniques (homogenization) in order to derive the effective properties of a material.

Homogenization studies often concentrate on the elastic behaviour of a micro-cracked material. In so-called *direct* methodology, cracks are represented as material discontinuities with parallel faces. The displacement jumps induced by the cracks allow deriving their contribution to the overall response. For instance, Kachanov (1993) and Nemat-Nasser and Hori (1993) have provided effective stiffness expressions for arbitrarily oriented microcracks. Eshelby's *equivalent inclusion method* (Eshelby 1957) also offers relevant solutions when considering cracks as flat ellipses (in 2D) or ellipsoids (in 3D). For instance, Mura (1987) has studied various ellipsoidal limit cases and Mori and Tanaka (1973) have enhanced the representation to the case of multiple interacting inhomogeneities. Note that energy-based bounds developed by Ponte Castañeda and Willis (1995) allow accounting for different spatial cracks distribution.

Based on the physical analogy with elasticity (as in pioneering works of Bristow 1960, see also Torquato 2002), some authors have extended these modelling approaches to thermal, electrical and permeability properties of cracked media (Wang and Jiang 2003, Sævik *et al.* 2013, Sevostianov and Kachanov 2019). For steady-state heat conduction, Sevostianov (2006) and others (Vu *et al.* 2015, Tran *et al.* 2018) apply the *direct* methodology based on temperature jump across insulating crack lips. For Hoenig (1983), Hatta and Taya (1986), Benveniste and Miloh (1989) and more recently Shafiro and Kachanov (2000), the *equivalent inclusion method* appears again as a key issue. While several studies account for the arbitrary value of matrix/inclusion conductivity and arbitrary crack's orientation or shape, most of the existing papers generally provide thermal conductivity of microcracked media in the non-interacting case. Nguyen *et al.* (2017) give closed-form expression for different schemes but consider only one orientation of the crack. Nevertheless, that is not the only challenge. Opening or closing of microcrack (also known as *unilateral effect*) can have a different influence on the material, in turn on the overall properties. Consequences of both induced anisotropy and unilateral effect on the elastic problem have been studied by few authors (Kachanov 1993, Deudé *et al.* 2002), but the same cannot be said for the heat conduction problem.

The modelling of the steady-state behaviour within microcracked media can also be achieved through numerical simulation. Carson *et al.* (2003) apply Finite Element Method (FEM) to find the conductivity of non-insulated porous of various shapes and sizes, while Tang *et al.* (2012) propose a similar modelling for concrete with conductive heterogeneities. Shen *et al.* (2015) use a plastic damage model to create cracks under tensile load and then consider steady-state conduction to find the conductivity of the microcracked concrete with high aggregate volume. One can cite also works of Tran *et al.* (2018) based on

an adaptive scheme Boundary Element Method (BEM) to find conductivity of a domain containing several cracks. Once again, we note that the crack orientation and unilateral effect are not given enough attention.

The present work intends to propose an Eshelby-like modelling approach for the steady-state heat transfer in a 2D microcracked medium. The effective thermal conductivity is derived based on the geometry of cracks considered as thin aspect ratio inclusions, and on the relevant choice of cracks properties according to their status (open or closed). The theoretical basis of the 2D linear thermal problem is stated in Section 2.2. As a demonstration, for different estimations (dilute and Mori-Tanaka schemes and Ponte Castañeda-Willis bound), closed-form expressions for a single-family of parallel cracks are presented in Section 2.3. In addition to the analytical solution, we also propose a numerical analysis of the thermal problem by means of finite element simulations. Modelling and description of the simulated area are given in Section 2.4. The results obtained from micromechanics and numerical simulation are finally compared and discussed in Section 2.5.

2.2 Theoretical Framework

We use the same framework used in Chapter 1 but for a 2D RVE (Fig. 2.1a). The cracks are modelled as a flat oblate ellipse (mean semi-axes a and c with $c \ll a$; Fig. 2.1b) with unit normal $\mathbf{n}$ and 2D volume fraction $f_c = \pi\ d\ \omega$ (see Appendix B.1). Here $d = \mathcal{N}a^2$ is the scalar crack density ($\mathcal{N}$ is the number of cracks per unit area) as defined by Budiansky and O'Connell (1976) and $\omega = {}^{c}/_{a} \ll 1$ is their mean aspect ratio.

The depolarization tensor $\mathbf{S}_E$ and its factors are given in Torquato 2002 (also see Appendix B.2). In our case, the said tensor for a flat oblate ellipse can be given as:

$$\mathbf{S}_E\ (\omega)\ =\ \frac{1}{1+\omega}\ \mathbf{n}\otimes\mathbf{n}\ +\ \frac{\omega}{1+\omega}\ (\mathbf{I}-\mathbf{n}\otimes\mathbf{n}), \qquad \forall\ \omega \ll 1 \tag{2.1}$$

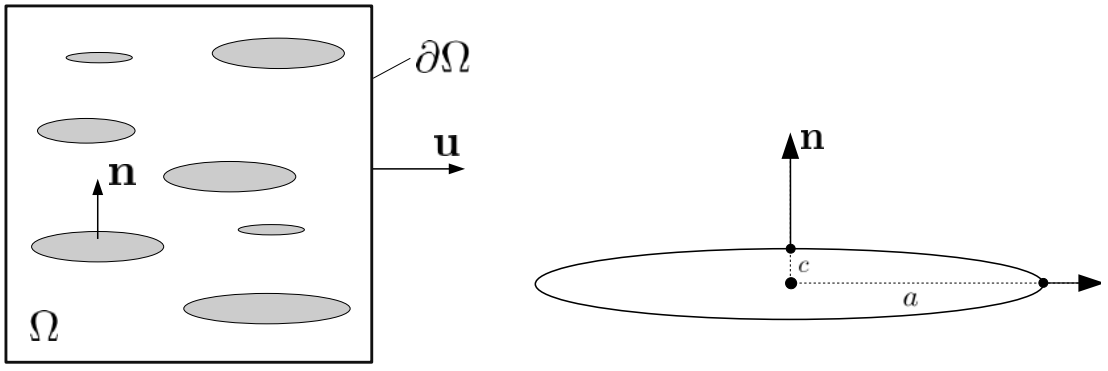

(a) (b)

Figure 2.1: (a) RVE with single family of parallel microcracks, (b) crack geometry.

2.3 Calculation of the effective thermal conductivity

We impose a uniform macroscopic thermal gradient G at the outer boundary $\delta\Omega$ of the RVE. This is similar to the classical strain-based formulation in elasticity. As a first, we will estimate the effective conductivity through different schemes and bounds. For a single family of cracks, Eq. (1.13) can be rewritten as

$$\boldsymbol{\lambda}_{hom} = \boldsymbol{\lambda}_m + f_c \, (\boldsymbol{\lambda}_c - \boldsymbol{\lambda}_m) \cdot \langle \mathbf{A} \rangle_c \tag{2.2}$$

When there is a **dilute** concentration of cracks (small d), it is considered that there is no interaction between them. The remote condition in this case can be given by $G_\infty = G$. Hence, the localization tensor can be given by:

$$\langle \mathbf{A} \rangle_c^{dil} = \Big[\mathbf{I} - \big(1 - \xi\big) \, \mathbf{S}_E \Big]^{-1} \quad \text{with} \quad \xi = \frac{\lambda_c}{\lambda_m} \tag{2.3}$$

Substituting (2.3) in (2.2), we get the general expression:

$$\boldsymbol{\lambda}_{hom}^{dil} = \boldsymbol{\lambda_m} \cdot \Big[\mathbf{I} - \pi \, d \, \mathbf{R} \Big] \tag{2.4}$$

where tensor $\mathbf{R}$ is defined as:

$$\mathbf{R}\,(\omega, \xi) = \omega \, \big(1 - \xi\big) \, \Big[\mathbf{I} - \mathbf{S}_E \, \big(1 - \xi\big) \Big]^{-1}, \quad \forall \, \omega \ll 1, \forall \, \xi \tag{2.5}$$

The above equation is valid for all the mean aspect ratio $\omega \ll 1$ and all the ratio ξ of scalar conductivity between defects and matrix. The present study focuses on the case of flat ellipse-shaped microcracks ($c \ll a$) for which aspect ratio tends to zero. Besides, we intend to account for different crack status:

- open cracks: one has $\lambda_c = 0$, so $\xi = 0$ and $\mathbf{R}\,(\omega \to 0, \xi = 0) = \mathbf{n} \otimes \mathbf{n}$,
- closed crack : one has $\lambda_c = \lambda^* \neq 0$, so $\xi \neq 0$ and $\mathbf{R}\,(\omega \to 0, \xi \neq 0) = \mathbf{0}$.

Accordingly (2.4) can be simplified into:

$$\boldsymbol{\lambda}_{hom}^{dil} = \begin{cases} \boldsymbol{\lambda_m} \cdot \Big[\mathbf{I} - \pi \; d \;\; \mathbf{n} \otimes \mathbf{n} \Big] & \text{, if cracks are open} \\ \boldsymbol{\lambda_m} & \text{, if cracks are closed} \end{cases} \tag{2.6}$$

When we are to consider some interactions between cracks, the **Mori-Tanaka** scheme may provide an interesting solution (Mori and Tanaka 1973). The boundary condition here is given by $G_\infty = \langle g \rangle_m$ and the localization tensor reads:

$$\langle \mathbf{A} \rangle_c^{MT} = \langle \mathbf{A} \rangle_c^{dil} \cdot \Big[(1 - f_c) \, \mathbf{I} + f_c \, \langle \mathbf{A} \rangle_c^{dil} \Big]^{-1} \tag{2.7}$$

This leads to:

$$\boldsymbol{\lambda}_{hom}^{MT} = \boldsymbol{\lambda_m} \cdot \Big[\mathbf{I} + \pi\, d\, \mathbf{R}\Big]^{-1} \tag{2.8}$$

As before, the specific behaviour of flat cracks according to their status gives the following:

$$\boldsymbol{\lambda}_{hom}^{MT} = \begin{cases} \boldsymbol{\lambda_m} \cdot \left[\mathbf{I} - \pi\, d\, \dfrac{1}{1+\pi\, d}\ \mathbf{n}\otimes\mathbf{n}\right] & \text{, if cracks are open} \\ \boldsymbol{\lambda_m} & \text{, if cracks are closed} \end{cases} \tag{2.9}$$

Ponte Castañeda-Willis developed an energy-based upper bound to find effective stiffness (Ponte Castañeda and Willis 1995). This bound takes into account the shape of the inclusion (through $\mathbf{S}_E$) and also the spatial distribution of cracks through an additional tensor $\mathbf{S}_d$. The simplified localization tensor can be given by:

$$\langle \mathbf{A} \rangle_c^{PCW} = \langle \mathbf{A} \rangle_c^{dil} \cdot \Big(\mathbf{I} + f_c\, (1-\xi)\, \mathbf{S}_d \cdot \langle \mathbf{A} \rangle_c^{dil}\Big)^{-1} \tag{2.10}$$

For simplicity, a circular spatial distribution is adopted, for which $\mathbf{S}_d = \dfrac{1}{2}\,\mathbf{I}$. Now Eq. (2.2) can be written as:

$$\boldsymbol{\lambda}_{hom}^{PCW} = \boldsymbol{\lambda}_m \cdot \left[\mathbf{I} - \pi\, d\, \mathbf{R} \cdot \left(\mathbf{I} + \frac{\pi\, d}{2}\, \mathbf{R}\right)^{-1}\right] \tag{2.11}$$

Based on the state of the flat defects, one gets:

$$\boldsymbol{\lambda}_{hom}^{PCW} = \begin{cases} \boldsymbol{\lambda_m} \cdot \left[\mathbf{I} - \pi\, d\, \dfrac{1}{1+\frac{\pi\, d}{2}}\ \mathbf{n}\otimes\mathbf{n}\right] & \text{, if cracks are open} \\ \boldsymbol{\lambda_m} & \text{, if cracks are closed} \end{cases} \tag{2.12}$$

Note that PCW bound will provide the same result as dilute and MT schemes when no spatial distribution is considered for the former and elliptical distribution for the latter. Similar developments for effective thermal resistivity can be found in Appendix B.3.

Some main comments can be made regarding these theoretical developments. First, the three modelling approaches show crack induced anisotropy for open cracks. Yet, Eqs. (2.6), (2.9) and (2.12) provide different expressions of the effective conductivity tensor through the tensorial term $\mathbf{n}\otimes\mathbf{n}$. We also observe that as $d \to 0$, all estimations lead to the same result which corresponds to the matrix conductivity $\left(\boldsymbol{\lambda}_{hom}^{dil}, \boldsymbol{\lambda}_{hom}^{MT}, \boldsymbol{\lambda}_{hom}^{PCW} \to \boldsymbol{\lambda}_m\right)$. On the other hand, we observe a complete deactivation of microcracking when the defects are closed $\left(\boldsymbol{\lambda}_{hom}^{dil} = \boldsymbol{\lambda}_{hom}^{MT} = \boldsymbol{\lambda}_{hom}^{PCW} = \boldsymbol{\lambda}_m\right)$. Fig. B.1a in Appendix B.3 shows the prediction of the effective thermal properties for increasing crack density.

2.4 Numerical simulations

In the following, numerical simulations are performed using finite element software ABAQUS. $(\mathbf{t}, \mathbf{v})$ denotes an orthonormal coordinate system. The simulated area $\mathcal{A}$ is a square (size $L = 1$ m) that follows steady-state heat conduction. The matrix is designed as an unit 2D shell with its own scalar conductivity λ_m. Assuming there are $\mathcal{N} = 10$ cracks in the area, the radius of the crack can be given by $a = \sqrt[2]{\frac{d}{\mathcal{N}}}$. In what follows, the range of considered density is less than 0.1, therefore, the maximum value of crack radius is 0.1 m.

Cracks are usually represented as seams for the open state (duplicated nodes). Yet, this cannot account for the heat transfer during crack closure. So, the crack is modelled here as an elliptical inclusion (created as a partition on the 2D shell) with normal $\mathbf{n}$ and scalar conductivity λ_c. Since creating a crack with zero aspect ratio is not possible ($\Omega_c = 0$), the cracks are designed with an aspect ratio $0 \neq \omega \ll 1$ (so $f_c \ll 1$). For a given f_c, the value of the scalar conductivity λ_c determines if the cracks are open ($\lambda_c = 0$) or closed ($\lambda_c = \lambda^* \neq 0$). Such a description of the crack geometry and the unilateral effect is in line with the theoretical framework used in Section 2.2. The cracks are positioned inside the simulated area using circular spatial distribution (in agreement with spatial distribution assumed for PCW bound). Since we want to study the influence of the crack's orientation on conductivity, further simulations are done by rotating the whole group of cracks which maintains a constant distance between them for all orientations. To be precise, the so-called *Reference Configuration* (RC) corresponds to the distribution of cracks rather grouped near the centre of $\mathcal{A}$ to reduce edge effects (Fig. 2.2). While keeping the circular spatial distribution, other configurations are also studied in the following to show the influence of cracks location.

The generalized scalar conductivity of a material $\lambda(\mathbf{v})$ related to the direction of unit vector $\mathbf{v}$ is given in the left part of Eq. (1.44) when the material is subjected to uniform

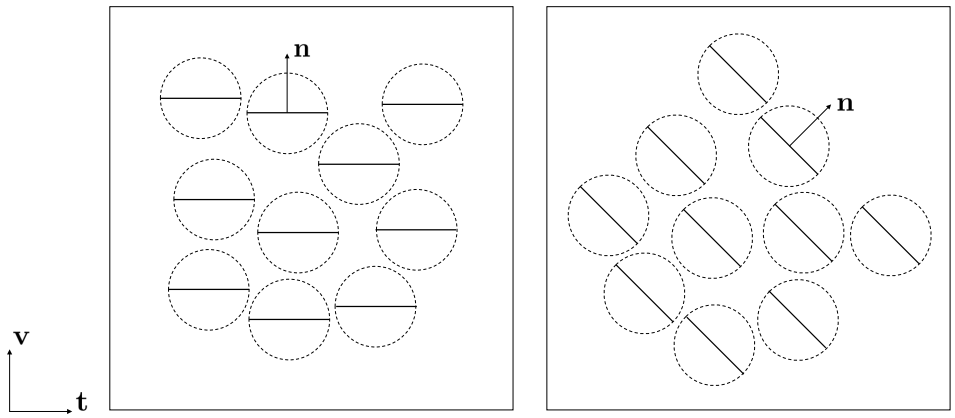

(a) $(\mathbf{n}, \mathbf{v}) = 0°$ (b) $(\mathbf{n}, \mathbf{v}) = 45°$

FIGURE 2.2: Simulated area showing spatial distribution of cracks for the Reference Configuration (RC).

temperature gradient $G = G_{\mathbf{v}}\ \mathbf{v}$. For the numerical model, zero flux condition is imposed on the left and right edges (with outer normals $\pm\ \mathbf{t}$) of area $\mathcal{A}$. At the same time, temperatures T_1 and T_2 ($\Delta T_{\mathbf{v}} = T_1 - T_2 > 0$) are applied respectively on the top and bottom edges (with outer normals $\pm\ \mathbf{v}$) of the cell; the temperature on each side is uniform. Such latter boundary condition, namely temperature gradient $G = G_{\mathbf{v}}\ \mathbf{v} = \dfrac{\Delta T_{\mathbf{v}}}{L}\ \mathbf{v}$, creates an overall heat flux $Q\,(= Q_{\mathbf{t}}\ \mathbf{t} + Q_{\mathbf{v}}\ \mathbf{v})$ inside the simulated area. On a global point of view, the two edges with zero flux act as adiabatic walls, allowing the heat flux Q to be mainly oriented along the $\mathbf{v}$ direction. From definition (1.44), the numerical effective conductivity in direction $\mathbf{v}$ is then provided by:

$$\lambda^{\text{num}}(\mathbf{v}) = \frac{Q_{\mathbf{v}}}{G_{\mathbf{v}}} \tag{2.13}$$

where $Q_{\mathbf{v}}$ is the average heat flux along the $\mathbf{v}$ direction. It can be calculated as $Q_{\mathbf{v}} = \dfrac{1}{L}\displaystyle\int_0^L \text{HFL2}\ d\mathbf{t}$ with HFL2 being the heat flux density in $\mathbf{v}$ direction along the path on the top/bottom edge. Alternatively, $Q_{\mathbf{v}}$ can be found using Reaction Flux RFL_i calculated on each node i on the top/bottom edge when considering unit dimension in the transverse direction, i.e. $Q_{\mathbf{v}} = \dfrac{1}{L}\displaystyle\sum_{i=1}^{n} \text{RFL}_i$.

The finite element type used for both the matrix and crack is quadratic triangular DC2D6 (see Fig. 2.3 for RC; $(\mathbf{n}, \mathbf{v}) = 45°$). Fixing 100 elements inside each crack, the influence of the size of the matrix elements on the heat flux has been studied (Tab. 2.1). We have used a very fine mesh to prevent improper scattering of the flux around the crack tips. In that case, the model has approximately 73500 elements and 148000 nodes including 201 nodes on the outer edges. Note that the computation time

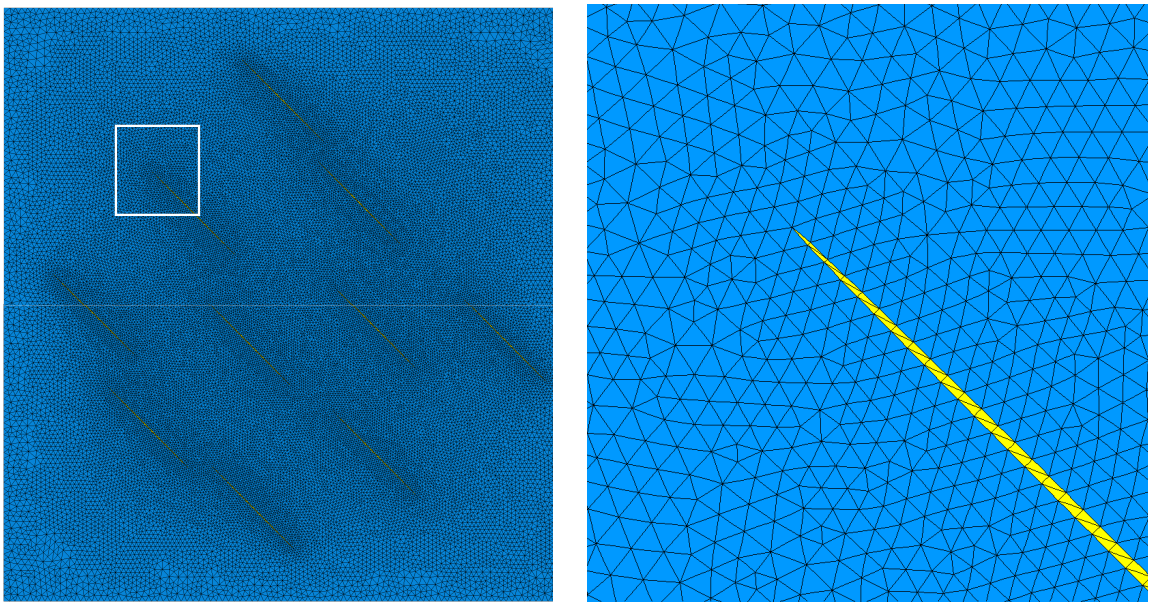

(a) Global mesh (b) Magnification around a crack tip

FIGURE 2.3: Simulated area mesh (RC; $(\mathbf{n}, \mathbf{v}) = 45°$).

TABLE 2.1: Influence of matrix element size on the average heat flux $Q_{\mathbf{v}}$ (RC; $(\mathbf{n}, \mathbf{v}) = 0°$)

Size of the matrix elements	0.1	0.05	0.025	0.01
Total no of elements	13804	42950	52976	73466
Heat flux $Q_{\mathbf{v}}$, W.m^{-2}	10484.4	10468.1	10468.0	10468.4

remains acceptable (less than a minute). Moreover, estimations of $\lambda^{\text{num}}(\mathbf{v})$ obtained for different cracks distributions have been compared for the most critical case, i.e. $(\mathbf{n}, \mathbf{v}) = 0°$ (Fig 2.4). From Tables 2.2 and 2.3, it is observed that cracks distribution and number of cracks (refer to Fig. 2.5 for configurations with different number of cracks) have no major influence on the resulting conductivity. Accordingly, the RC with 10 cracks will be considered for all further simulations done in the study.

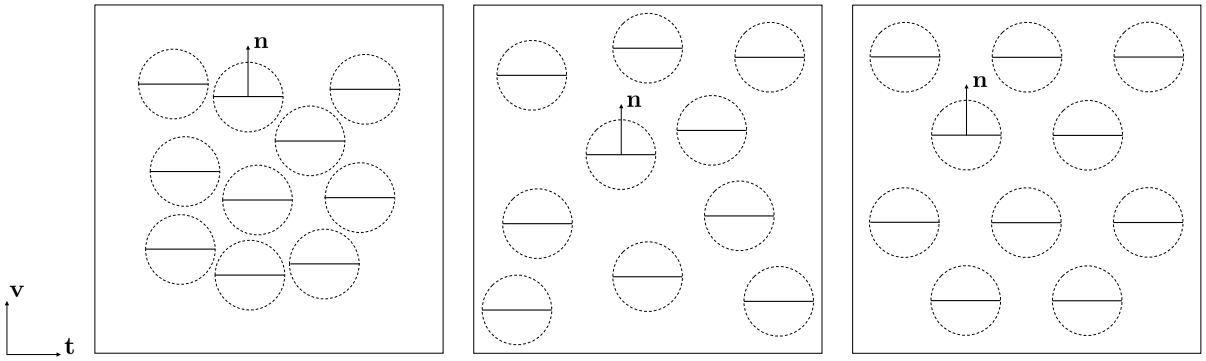

(a) Reference Configuration (b) Configuration 1 (c) Configuration 2

FIGURE 2.4: Influence of cracks position for $(\mathbf{n}, \mathbf{v}) = 0°$.

TABLE 2.2: Influence of cracks distributions ($(\mathbf{n}, \mathbf{v}) = 0°$)

Configuration	$\lambda^{\text{num}}/\lambda_m$	Deviation w.r. RC
Reference configuration (RC)	0.727	-
Configuration 1	0.730	0.47 %
Configuration 2	0.732	0.66 %

TABLE 2.3: Influence of number of cracks ($(\mathbf{n}, \mathbf{v}) = 0°$)

No. of cracks	$Q_{\mathbf{v}}$, W.m^{-2}	Deviation w.r. 10 cracks
1	10423.9	2.63 %
2	10885.9	1.73 %
5	10553.6	1.36 %
10	10697.6	-
15	10790.4	0.86 %
20	10677.1	0.29 %

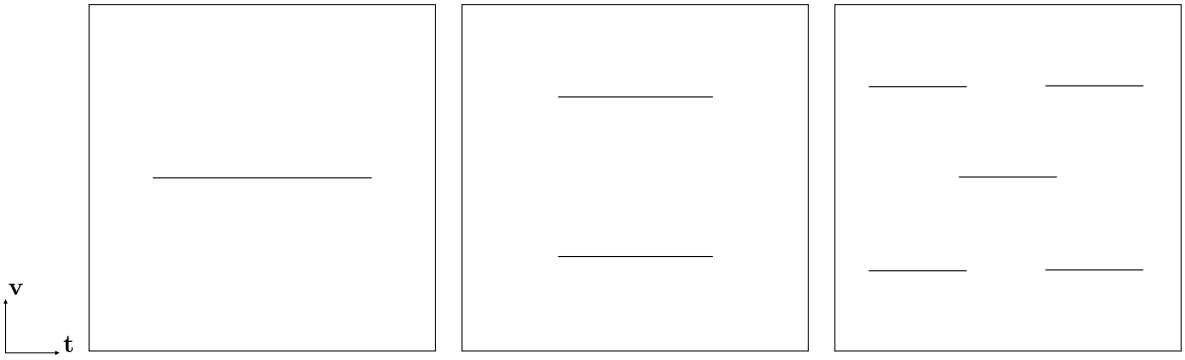

(a) 1 crack (b) 2 cracks (c) 5 cracks

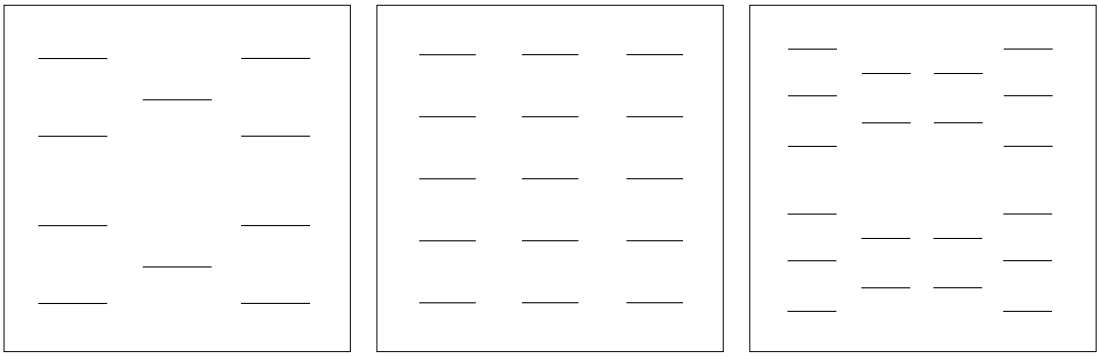

(d) 10 cracks (e) 15 cracks (f) 20 cracks

FIGURE 2.5: Configurations with different number of cracks ($(\mathbf{n}, \mathbf{v}) = 0°$)

As first illustration, Fig. 2.6 shows the heat flux vector at integration points for density $d = 0.1$ (RC; $(\mathbf{n}, \mathbf{v}) = 45°$). For the open case ($\lambda_c = 0$, Fig. 2.6a), the cracks act as a thermal barrier according to the adiabatic behavior on their lips, whereas, for the closed case ($\lambda_c = 50\%\ \lambda_m$, Fig. 2.6b), heat transfer exhibits continuity.

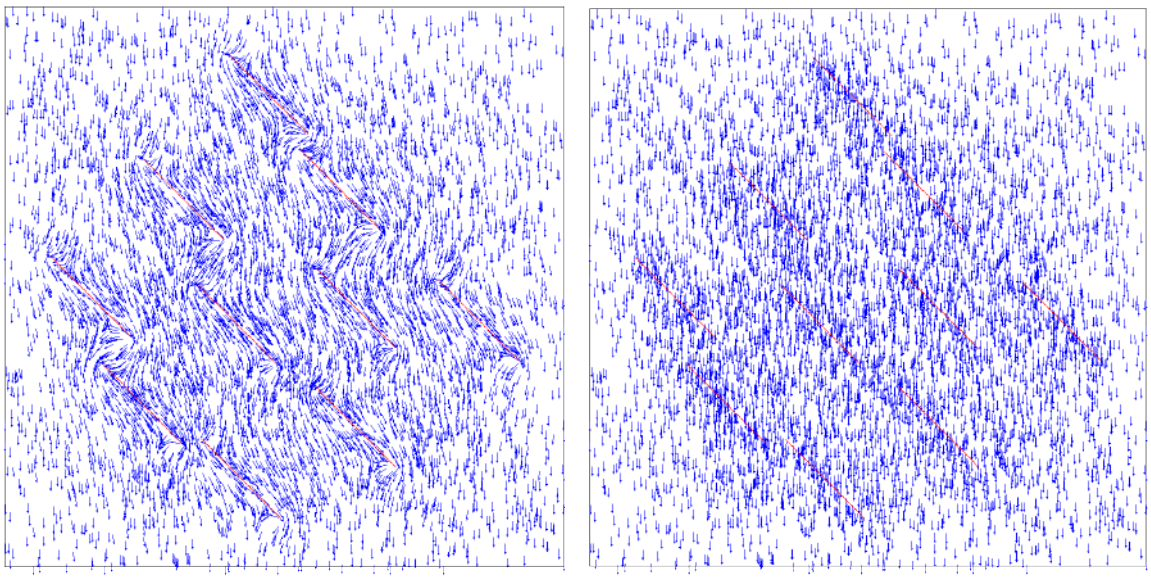

(a) Open crack (b) Closed crack ($\lambda^* = 50\%\ \lambda_m$)

FIGURE 2.6: Heat flux vectors at integration points inside the simulated area (RC; $(\mathbf{n}, \mathbf{v}) = 45°; d = 0.1; a = 0.1$ m; $\omega = 0.001$).

2.5 Results and discussion

This section intends to compare theoretical developments and FE numerical simulations. From (1.44) and (1.6), the theoretical scalar conductivity $\lambda(\mathbf{v})$ comes to:

$$\lambda^{\text{th}}(\mathbf{v}) = \mathbf{v} \cdot \boldsymbol{\lambda}_{hom} \cdot \mathbf{v} \tag{2.14}$$

This can be estimated for different schemes ($\text{th} = \{dil, MT, PCW\}$) and compared to $\lambda^{\text{num}}(\mathbf{v})$.

Recalling previous results from Section 2.3, open cracks contribute to the degradation of the thermal conductivity, mainly along the direction $\mathbf{n}$ normal to the crack surface. This case is true for the simulations as well (Fig. 2.7). Both the theoretical and simulated results show us damage-induced anisotropy irrespective of the scheme or crack density. As pointed out earlier, for the theoretical models, we see that as $d \to 0$, $\boldsymbol{\lambda}_{hom}^{dil} \approx \boldsymbol{\lambda}_{hom}^{MT} \approx \boldsymbol{\lambda}_{hom}^{PCW}$ ($d = 0.1$ in Fig. 2.7a, $d = 0.05$ in Fig. 2.7b). This can be attributed to the fact that as d decreases, the size of the crack decreases (respectively from $a = 0.1$ m to $a = 0.07$ m), making the interaction between the cracks less influential and, at one point, there is no interaction between the cracks essentially leading to a dilute configuration. We also see that as the crack becomes smaller, so does its influence on the conductivity ($\lambda(\mathbf{n}) \approx 0.73$ λ_m for $a = 0.1$ m whereas $\lambda(\mathbf{n}) \approx 0.86$ λ_m for $a = 0.07$ m). Fig. 2.7 also illustrates the consistency between the theoretical and simulated results. It is interesting to observe that for lesser angles $(\mathbf{n}, \mathbf{v}) < 45°$, simulated results tend towards PCW and for higher angles, they approach the dilute case. Indeed, interactions are greater when the cracks are mostly orthogonal to the heat flux. But, if cracks tend to be aligned with the direction of the temperature gradient then the influence of cracks decreases and heat flux is less disturbed, tending to the dilute case (Fig. 2.8).

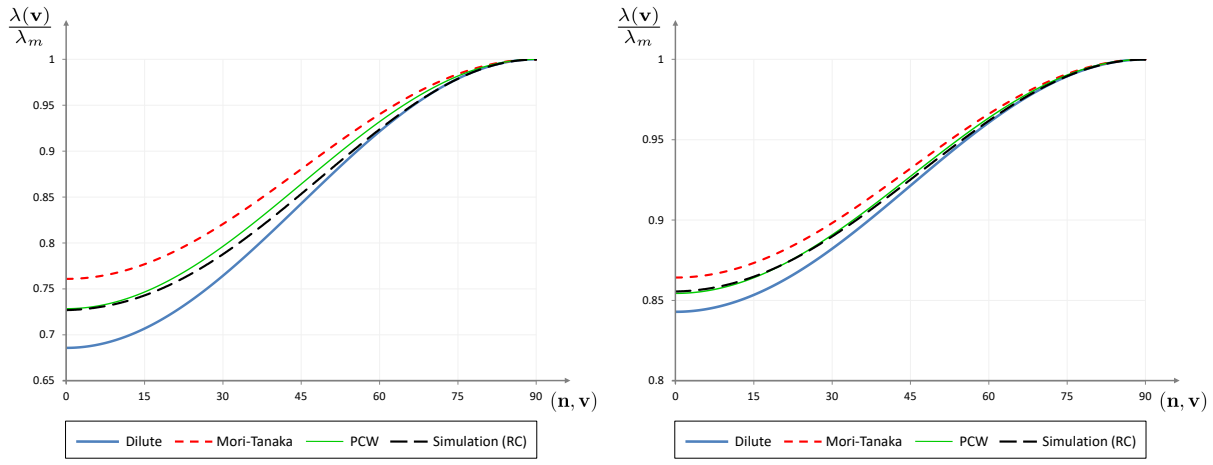

(a) $d = 0.1$ ($a = 0.1$ m) (b) $d = 0.05$ ($a = 0.07$ m)

FIGURE 2.7: Generalized thermal conductivity $\lambda(\mathbf{v})$ in 2D normalized by its initial value for a material weakened by a single array of parallel open microcracks of unit normal $\mathbf{n}$.

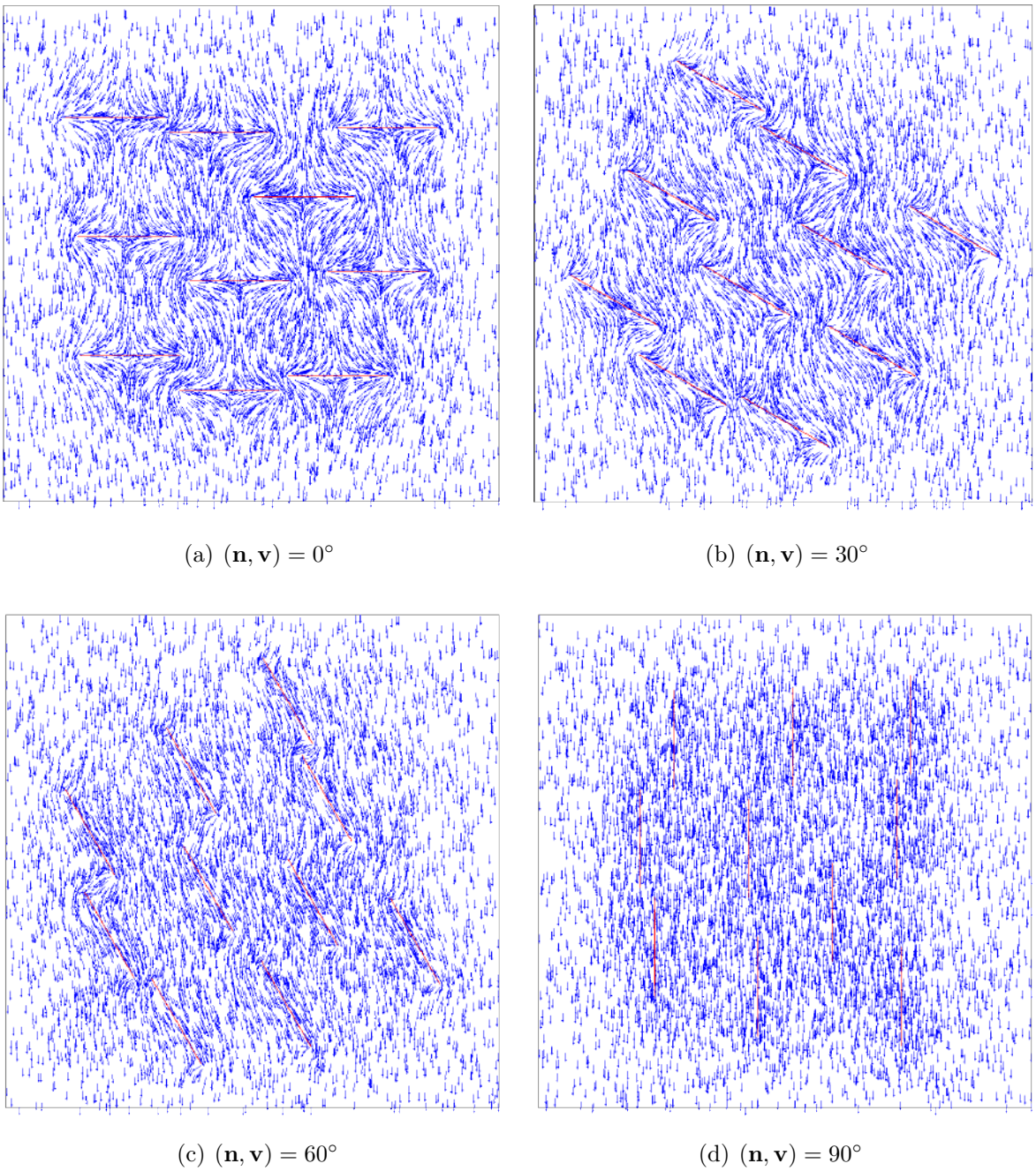

(a) $(\mathbf{n}, \mathbf{v}) = 0°$ (b) $(\mathbf{n}, \mathbf{v}) = 30°$

(c) $(\mathbf{n}, \mathbf{v}) = 60°$ (d) $(\mathbf{n}, \mathbf{v}) = 90°$

FIGURE 2.8: Heat flux vectors at integration points for various orientations of open cracks (RC; $d = 0.1$; $a = 0.1$ m; $\omega = 0.001$).

On the other hand, dilute, Mori-Tanaka and PCW approaches show that closed cracks do not contribute to the degradation of conductivity (see Eqs. (2.6), (2.9) and (2.12)), i.e. the effective conductivity in any direction is recovered to its initial value at the cracks closure. So the generalized scalar conductivity in unit direction $\mathbf{v}$ for closed cracks can be given as: $\lambda(\mathbf{v}) = \lambda_m, \ \forall \, \mathbf{v}$. Just like the open crack, simulated and theoretical results are consistent for the closed crack (Fig. 2.9). We also see that the former has only a negligible amount of degradation of thermal conductivity (less than 0.035% for $d = 0.1$ and less than 0.02% for $d = 0.05$ when considering $\lambda^* = 50\% \ \lambda_m$).

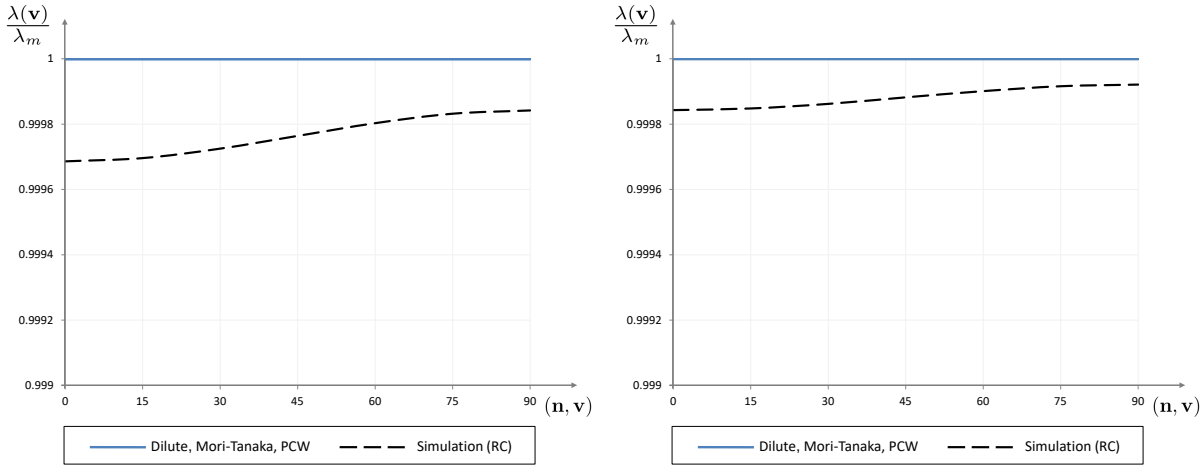

(a) $d = 0.1$ ($a = 0.1$ m) (b) $d = 0.05$ ($a = 0.07$ m)

FIGURE 2.9: Generalized thermal conductivity $\lambda(\mathbf{v})$ in 2D normalized by its initial value for a material weakened by a single array of parallel closed microcracks of unit normal $\mathbf{n}$ (RC; $\lambda^* = 50\%\ \lambda_m$).

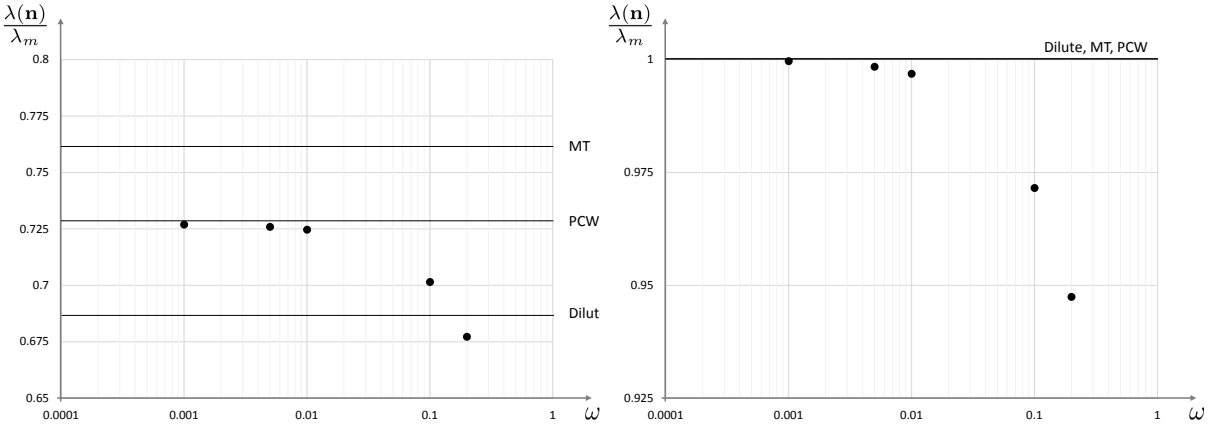

(a) Open cracks (b) Closed cracks

FIGURE 2.10: Normal thermal conductivity $\lambda(\mathbf{n})$ in 2D normalized by its initial value for various aspect ratios ($d = 0.1; a = 0.1$ m); points represent simulation results (RC); $\log_{10}$ scale is used for abscissa.

From Eqs. (2.6), (2.9) and (2.12), we know that the theoretical results are not a function of the aspect ratio ω since they all correspond to the limit case $\omega \to 0$ $\left(\boldsymbol{\lambda}_{hom}^{dil}, \boldsymbol{\lambda}_{hom}^{MT}\right.$ and $\left.\boldsymbol{\lambda}_{hom}^{PCW}\right.$ only depend on λ_m, d and $\mathbf{n}$). But as discussed earlier, it is not possible to simulate an ellipse with zero aspect ratio. So it seems natural to study the influence of the aspect ratio on the simulated results. Since the maximum degradation is along the direction $\mathbf{n}$ normal to the crack, we intend to focus only on $\lambda(\mathbf{n})$. Fig. 2.10a corresponds to open crack and Fig. 2.10b corresponds to closed crack with fixed values of dilute, MT and PCW denoted as reference. In both cases, the simulated results are really sensitive to the aspect ratio ω and get closer to the PCW bound when $\omega \to 0$. Especially in the closed case, the simulations tend to the full recovery of $\lambda(\mathbf{n})$, same as the theoretical models. Note that all the simulations linked to varying aspect ratio are performed by varying the crack thickness c and keeping the crack density d and radius a as constants.

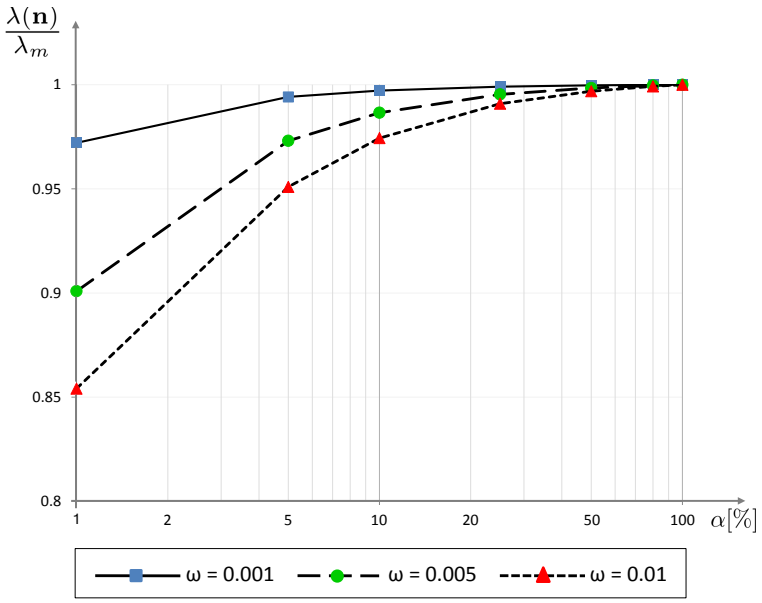

FIGURE 2.11: Influence of scalar conductivity λ^* on the normal thermal conductivity $\lambda(\mathbf{n})$ in 2D normalized by its initial value (RC; $d = 0.1; a = 0.1$ m); $\log_{10}$ scale is used for abscissa.

Also, the theoretical results for the closed case do not depend on the fictitious scalar conductivity λ^*. This may not be true for the simulations. So, a series of simulations were performed with varying λ^* and for different aspect ratios (d and a are still constants). The values for λ^* are given as a proportion of λ_m such that $\lambda^* = \alpha\ \lambda_m$ with $\alpha = \{1,$ 5, 10, 25, 50, 80, 100$\}$[%]. Fig. 2.11 shows that there is a clear influence of the scalar conductivity λ^* on the numerical thermal conductivity. For $\alpha \leq 10\%$, we see a drastic decrease in the conductivity, this is due to the fact that we are slowly approaching the open case ($\alpha = 0$). We also observe that as $\omega \to 0$ the influence of λ^* diminishes and representation of closed cracks by means of an ellipse with fictitious scalar conductivity λ^* becomes independent of the λ^* value, just like the theoretical results.

2.6 Conclusion and perspectives

The consistency of theoretical and numerical results have been demonstrated through the following points. For open cracks, we observe that the microcracked medium exhibits an induced anisotropy with the major degradation of the conductivity in the direction normal to the cracks. Also, the increase in cracks density accentuates the differences between the estimates (Fig. B.1a). We note that the simulations results are close to PCW results. On the other hand, cracks closure leads to the deactivation of their related effects on thermal properties. Finally, the sensitivity of numerical results based on the aspect ratio of defects and scalar conductivity of closed defects has been shown.

Chapter 3

Thermoelastic properties in 3D

Abstract

Chapters 1 and 2 were focused on the pure thermal problem. In order to completely account for the thermomechanical issues, it is imperative to study thermoelasticity as well. Homogenization of microcracked media is largely dedicated to the determination of the effective elastic properties. Accounting for thermomechanical cases, extension of such approach to thermoelastic behaviour is not investigated much. Within the classical homogenization framework, this chapter aims at implementing several micromechanical techniques to establish the closed-form expressions of effective thermoelastic properties of a microcracked medium (thermal tensors and specific heat capacities). These expressions have not been explicitly provided before in the literature and may provide some relevant elements for the experimental or numerical study of the thermomechanical behaviour of brittle materials. This work considers randomly distributed microcracks and specially accounts for the influence of the unilateral effect (opening and closure of cracks) on the said properties. The theoretical representations are obtained using the dilute and Mori-Tanaka schemes and Ponte Castañeda-Willis bounds, either using strain or stress boundary conditions.

Present chapter corresponds to the submitted research paper (Rangasamy Mahendren et al. 2020b) [Euro. J. Mech. A/Solids; submitted].
A self-consistent notation is adopted.

3.1 Introduction

Most of brittle materials initially exhibit several microcracks at the microstructural level due to their manufacturing process. For instance, shrinkage in cement-based materials or cooling phase for high-temperature sintered or brazed ceramics are typical causes for such degradation. Exposure to thermomechanical loads or any environmental service conditions may also either create or increase the amount of these defects. In all cases, the presence of microcracks have a significant influence on the materials overall properties and more generally on the structures behaviour. Investigation of the effective properties of microcracked media thus appears as really important for several industrial applications.

Estimations of random microcracked media elastic properties by means of homogenization models abound in the literature Mura (1987), Nemat-Nasser and Hori (1993), Dormieux and Kondo (2016). Mean field theories provide the average strains (resp. stresses) in each phase, and in turn the relationship between micro and macroscopic quantities and effective stiffness (resp. compliance) (Hill 1963 1965). Precisely, the eigenstrain method (also called Eshelby's equivalent inclusion method) offers a relevant framework to account for the structural morphology of heterogeneous media. Solutions rely on the inclusion and inhomogeneity problems as reported by Eshelby (1957). Cracks are treated as flat ellipsoidal cavities embedded in an infinite matrix subjected to uniform macroscopic boundary conditions. The most widely used model is undoubtely the dilute scheme, developed for low levels of microcracking density (Nemat-Nasser and Hori 1993, Kachanov 1993). When considering interactions between cracks, one can briefly mention several approximate schemes : self-consistent (Budiansky and O'Connell 1976, Horii and Nemat-Nasser 1983), differential (Hashin 1988, Zimmerman 1985), Mori-Tanaka (MT) (Mori and Tanaka 1973, Benveniste 1987) and effective fields methods (Kanaun 1980) or models based on Maxwell's theory (Sevostianov and Giraud 2013). Upper and lower bounds of overall elastic properties have also been derived using variational energy approaches (Ponte Castañeda and Willis 1995, Dormieux and Kondo 2009). It is worth noting that the effective properties not only depend on the matrix properties and the damage density but also on the shape and spatial distribution of the cracks. Above-mentioned methods take into account spatial distribution differently. For example, the MT scheme assumes a distribution identical to the shape of the inclusion whereas the Ponte Castañeda-Willis (PCW) bound allows one to choose the spatial distribution (ellipsoidal, spherical, etc.)

Another challenge in finding the effective properties is the microcracks unilateral effect. Depending on whether they are open or closed (due to tension or compression local loads), the microcracks contribution to the materials behaviour differ, leading in particular to a recovery (partial or total) of the effective properties at the closure of microcracks (Reinhardt 1984, Morvan and Baste 1998). The simultaneous account of such specific feature with arbitrarily orientation of defects and related induced anisotropy is even a more complex task (Chaboche 1992, Cormery and Welemane 2002). As many practical issues require the proper modelling of these phenomena, homogenization appears again

as an essential tool for predicting the resulting anisotropic multilinear elasticity of micro-craked media. In direct approaches, microcracks are considered as discontinuous plane surfaces. Then special recourse is made to solutions from classical fracture mechanics (so-called Griffith crack problem) to determine displacement jumps between their lips (Kachanov 1993, Andrieux *et al.* 1986, Pensée and Kondo 2001, Goidescu *et al.* 2013). Although opening and closing of cracks are naturally treated through the modification of displacement discontinuities, such modelling option is most often limited to the case of non-interacting defects. This motivates the application of the eigen strain method and the representation of cracks as the limit case of thin ellipsoidal inclusions with aspect ratio tending to zero. In that case, while the open status of cracks can naturally be accounted as an inclusion with zero elasticity, some questions arise for the closed state. Deudé *et al.* (2002) suggest to design the latter case as a fictitious isotropic material with same bulk modulus as the matrix and zero shear modulus. This reflects the ability of frictionless cracks to transfer only normal stresses at their closure. As said before, the main interest of such Eshelby approach stands in the possible extension to the case of interacting cracks by means of aforementioned estimation schemes and variational bounds (Dormieux and Kondo 2009).

From this, it can be said that linear elasticity has been studied extensively both for composite materials and microcracked media. Yet, cracks are known to affect also thermo-elastic, electric, magnetic, diffusive and conductive properties as well. Existing homogenization framework can be applied to derive the said properties (Wang and Jiang 2003, Dormieux *et al.* 2006, Su *et al.* 2008, Sevostianov and Kachanov 2019, Chapter 1) The case of thermoelasticity, and specially thermostatics (systems at uniform temperature), is closely linked to elasticity. Hence, thermoelastic effective properties of composite materials have long been established in the spirit of Hill's theory (Hill 1963 1965). Since pioneering works of Levin (1967), Rosen and Hashin (1970), Laws (1973), extensive research has been done on this topic (see references books of Torquato 2002, Buryachenko 2007, François *et al.* 2012) and both approximations of effective properties and energetic bounds have been derived and compared (Karch 2014, Böhm 2019). For the special case of two-phase composites, the so-called Levin's theorem (Levin 1967) (see also Rosen and Hashin 1970, Laws 1973) even allows the calculation of thermoelastic effective properties directly in terms of effective elastic ones.

Considering microcracks as a special case of thin inclusions, it is known that expressions of the overall thermal properties for brittle materials can be computed by the same methodologies as for the composites. Moreover, the important research on elasticity for these materials has often been considered sufficient to cover the thermoelastic behaviour simultaneously. This explains why studies are very scarce when it comes to effective thermoelastic properties of materials with crack-like inclusions. However, homogenized expressions, that have not been explicitly given before in the literature, may be useful for the study of the thermomechanical behaviour of brittle materials by allowing comparisons

with experimental or numerical studies.

This work thus intends to implement homogenization techniques for 3D microcracked media and derive closed-form expressions of their effective thermoelastic properties for several classical models. Considering both strain and stress-based formulations, this study accounts for the case of an isotropic matrix weakened by arbitrarily oriented microcracks. Attention is also paid to the open or closed status of cracks and their different influence on the overall properties. Such representation of the specific unilateral behaviour of crack defects is an important contribution of the work. After a short recall of the theoretical framework (Section 3.2), this paper provides analytical expressions of effective thermoelastic strain-based (Sections 3.3, 3.4 and 3.5) and stress-based (Section 3.6) properties for several estimation approaches based on eigenstrain homogenization method. The different models implemented take into account (Mori-Tanaka scheme and Ponte Castañeda-Willis bound) or not (dilute scheme) some interactions between microcracks.

3.2 Theoretical Framework

3.2.1 Homogenenization of heterogeneous media

The present work deals with infinitesimal thermoelastic transformations. Considering the strain tensor $\boldsymbol{\varepsilon}$ and absolute temperature T as observable variables and assuming an initial $(\boldsymbol{\varepsilon}_0 = \mathbf{0}, T_0)$ natural state, the specific free energy (per unit volume) of the medium can be expressed as (Germain *et al.* 1983, Maitournam 2017):

$$W(\boldsymbol{\varepsilon}, T) = \frac{1}{2}\boldsymbol{\varepsilon} : \mathbb{C} : \boldsymbol{\varepsilon} - \boldsymbol{\kappa} : \boldsymbol{\varepsilon}\ \Delta T - \frac{1}{2}\frac{c_\varepsilon}{T_0}\ \Delta T^2 \tag{3.1}$$

with $\mathbb{C}$ the fourth order stiffness tensor, $\Delta T = T - T_0$ the temperature difference, $\boldsymbol{\kappa}$ the second order thermal stress tensor and c_ε the scalar specific heat capacity (per unit volume) at constant strain. Similarly, it is possible to introduce the complementary formalism based on the specific free enthalpy (per unit volume):

$$U(\boldsymbol{\sigma}, T) = \frac{1}{2}\boldsymbol{\sigma} : \mathbb{S} : \boldsymbol{\sigma} + \boldsymbol{\alpha} : \boldsymbol{\sigma}\ \Delta T + \frac{1}{2}\frac{c_\sigma}{T_0}\ \Delta T^2 \tag{3.2}$$

where $\boldsymbol{\sigma}$ denotes the stress tensor, $\mathbb{S}$ the fourth order compliance tensor, $\boldsymbol{\alpha}$ the second order thermal strain tensor (also called dilatation tensor) and c_σ the scalar specific heat capacity (per unit volume) at constant stress. Elastic tensors are inverse of each other, $\mathbb{C} : \mathbb{S} = \mathbb{I} = \mathbf{I} \underline{\otimes} \mathbf{I}$ (with $\mathbb{I}$ and $\mathbf{I}$ being the fourth and second order symmetric identity tensors respectively), while thermal tensors are linked by $\boldsymbol{\kappa} = \mathbb{C} : \boldsymbol{\alpha}$ and $c_\sigma = c_\varepsilon + T_0\ \boldsymbol{\alpha} : \boldsymbol{\kappa}$. From (3.1) and (3.2), constitutive relations for the thermoelastic medium come to (s the

entropy and ρ the material density) :

$$\boldsymbol{\sigma} = \mathbb{C} : \boldsymbol{\varepsilon} - \boldsymbol{\kappa}\, \Delta T \quad \text{and} \quad s = \frac{1}{\rho}\left(\boldsymbol{\kappa} : \boldsymbol{\varepsilon} + \frac{c_\varepsilon}{T_0}\, \Delta T\right) \tag{3.3}$$

and

$$\boldsymbol{\varepsilon} = \mathbb{S} : \boldsymbol{\sigma} + \boldsymbol{\alpha}\, \Delta T \quad \text{and} \quad s = \frac{1}{\rho}\left(\boldsymbol{\alpha} : \boldsymbol{\sigma} + \frac{c_\sigma}{T_0}\, \Delta T\right) \tag{3.4}$$

Let us consider a 3D Representative Volume Element (RVE, of volume Ω) of a micro-cracked medium composed of an isotropic matrix material weakened by several families of microcracks. Boundary conditions applied to the outer boundary $\delta\Omega$ of the RVE are either uniform macroscopic strain ($\mathbf{E}$ imposed at $\delta\Omega$) or uniform macroscopic stress ($\boldsymbol{\Sigma}$ imposed at $\delta\Omega$), and uniform temperature $T \neq T_0$. Under equilibrium conditions, the macroscopic stress $\boldsymbol{\Sigma}$ (respectively macroscopic strain $\mathbf{E}$) corresponds to the average value of its microscopic quantity $\boldsymbol{\sigma}$ (resp. $\boldsymbol{\varepsilon}$) (François *et al.* 2012, Böhm 2019, Zaoui 2002):

$$\boldsymbol{\Sigma} = \frac{1}{\Omega}\int_\Omega \boldsymbol{\sigma}\, d\Omega = \langle \boldsymbol{\sigma} \rangle \qquad \text{and} \qquad \mathbf{E} = \langle \boldsymbol{\varepsilon} \rangle \tag{3.5}$$

and the temperature change ΔT is uniform throughout the RVE. In the present linear framework, microscopic fields are simply related to boundary data (Hill 1963):

$$\boldsymbol{\varepsilon}(x) = \mathbb{A}(x) : \mathbf{E} + \mathbf{a}\Delta T \quad \text{or} \quad \boldsymbol{\sigma}(x) = \mathbb{B}(x) : \boldsymbol{\Sigma} + \mathbf{b}\Delta T \qquad \forall\, x \in \Omega \tag{3.6}$$

where $\mathbb{A}$ and $\mathbb{B}$ (respectively $\mathbf{a}$ and $\mathbf{b}$) are the symmetric fourth (resp. second) order strain localization and stress concentration (resp. thermal strain localization and stress concentration) tensors, such that

$$\langle \mathbb{A} \rangle = \langle \mathbb{B} \rangle = \mathbb{I} \quad \text{and} \quad \langle \mathbf{a} \rangle = \langle \mathbf{b} \rangle = \mathbf{0} \tag{3.7}$$

Combination of constitutive laws Eqs. (3.3) and (3.4) with average relations (3.5) leads to the overall behaviour of the RVE:

$$\boldsymbol{\Sigma} = \mathbb{C}_{hom} : \mathbf{E} - \boldsymbol{\kappa}_{hom}\, \Delta T \qquad \text{and} \qquad \langle s \rangle = \frac{1}{\rho}\left(\boldsymbol{\kappa_{hom}} : \mathbf{E} + \frac{c_{\varepsilon,hom}}{T_0}\, \Delta T\right) \tag{3.8}$$

and

$$\mathbf{E} = \mathbb{S}_{hom} : \boldsymbol{\Sigma} + \boldsymbol{\alpha}_{hom}\, \Delta T \qquad \text{and} \qquad \langle s \rangle = \frac{1}{\rho}\left(\boldsymbol{\alpha}_{hom} : \boldsymbol{\Sigma} + \frac{c_{\sigma,hom}}{T_0}\, \Delta T\right) \tag{3.9}$$

where $\mathbb{C}_{hom}$ (resp. $\mathbb{S}_{hom}$) the effective stiffness (resp. compliance) tensor, $\boldsymbol{\kappa}_{hom}$ (resp. $\boldsymbol{\alpha}_{hom}$) the effective thermal stress (resp. thermal strain) tensor and $c_{\varepsilon,hom}$ (resp. $c_{\sigma,hom}$) the effective specific heat capacity at constant strain (resp. stress). Lets denote $\mathbb{C}_m$, $\mathbb{S}_m$, $\boldsymbol{\kappa}_m$, $\boldsymbol{\alpha}_m$, $c_{\varepsilon,m}$ and $c_{\sigma,m}$ as the stiffness, compliance, thermal stress and thermal strain tensors and specific heat capacities at constant strain and stress of the matrix respectively,

and $\mathbb{C}_{c,i}$, $\mathbb{S}_{c,i}$, $\boldsymbol{\kappa}_{c,i}$, $\boldsymbol{\alpha}_{c,i}$, $c_{\varepsilon,c,i}$ and $c_{\sigma,c,i}$ as the stiffness, compliance, thermal stress and thermal strain tensors and specific heat capacities at constant strain and stress of the i^{th} (i =1...N) family of parallel cracks respectively. Assuming phase-wise uniform properties, the effective behaviour of the microcracked RVE can be approximated by means of phase averages (Zaoui 2002, Ponte Castañeda 2002, Willis 2002, Böhm 2019):

- for elasticity tensors:

$$\mathbb{C}_{hom} = \langle \mathbb{C} : \mathbb{A} \rangle = \mathbb{C}_m + \sum_{i=1}^{N} f_{c,i} \left(\mathbb{C}_{c,i} - \mathbb{C}_m \right) : \langle \mathbb{A} \rangle_{c,i} \tag{3.10}$$

and

$$\mathbb{S}_{hom} = \langle \mathbb{S} : \mathbb{B} \rangle = \mathbb{S}_m + \sum_{i=1}^{N} f_{c,i} \left(\mathbb{S}_{c,i} - \mathbb{S}_m \right) : \langle \mathbb{B} \rangle_{c,i} \tag{3.11}$$

- for thermal dilatometric tensors:

$$\boldsymbol{\kappa}_{hom} = \langle \boldsymbol{\kappa} - \mathbb{C} : \mathbf{a} \rangle = \langle \boldsymbol{\kappa} : \mathbb{A} \rangle = \boldsymbol{\kappa}_m + \sum_{i=1}^{N} f_{c,i} \left(\boldsymbol{\kappa}_{c,i} - \boldsymbol{\kappa}_m \right) : \langle \mathbb{A} \rangle_{c,i} \tag{3.12}$$

and

$$\boldsymbol{\alpha}_{hom} = \langle \boldsymbol{\alpha} + \mathbb{S} : \mathbf{b} \rangle = \langle \boldsymbol{\alpha} : \mathbb{B} \rangle = \boldsymbol{\alpha}_m + \sum_{i=1}^{N} f_{c,i} \left(\boldsymbol{\alpha}_{c,i} - \boldsymbol{\alpha}_m \right) : \langle \mathbb{B} \rangle_{c,i} \tag{3.13}$$

- for specific heat capacities:

$$c_{\varepsilon,hom} = \langle c_\varepsilon + T_0 \, \boldsymbol{\kappa} : \mathbf{a} \rangle = c_{\varepsilon,m} + \sum_{i=1}^{N} f_{c,i} \left(c_{\varepsilon,c,i} - c_{\varepsilon,m} + T_0 \left(\boldsymbol{\kappa}_{c,i} - \boldsymbol{\kappa}_m \right) : \langle \mathbf{a} \rangle_{c,i} \right) \tag{3.14}$$

and

$$c_{\sigma,hom} = \langle c_\sigma + T_0 \, \boldsymbol{\alpha} : \mathbf{b} \rangle = c_{\sigma,m} + \sum_{i=1}^{N} f_{c,i} \left(c_{\sigma,c,i} - c_{\sigma,m} + T_0 \left(\boldsymbol{\alpha}_{c,i} - \boldsymbol{\alpha}_m \right) : \langle \mathbf{b} \rangle_{c,i} \right) \tag{3.15}$$

In Eqs. (3.10)-(3.15), $f_{c,i}$ is the cracks volume fraction of the i^{th} family, $\langle \cdot \rangle_r = \frac{1}{\Omega_r} \int_{\Omega_r} \cdot \, d\Omega$ denotes the mean value over the volume of the phase $r = \{m, c\}$ (m for matrix and c for cracks) and conditions $\mathbb{C}_r : \mathbb{S}_r = \mathbb{I}$, $\boldsymbol{\kappa}_r = \mathbb{C}_r : \boldsymbol{\alpha}_r$ and $c_{\sigma,r} = c_{\varepsilon,r} + T_0 \, \boldsymbol{\alpha}_r : \boldsymbol{\kappa}_r$ hold for each phase r. At that point, effective tensors $\mathbb{C}_{hom}$, $\boldsymbol{\kappa}_{hom}$ and $c_{\varepsilon,hom}$ (derived from strain-based boundary condition with uniform ΔT) and $\mathbb{S}_{hom}$, $\boldsymbol{\alpha}_{hom}$ and $c_{\sigma,hom}$ (derived from stress-based boundary condition with uniform ΔT) strictly describe the same equivalent homogeneous media, so that these tensors follow the relations $\mathbb{C}_{hom} : \mathbb{S}_{hom} = \mathbb{I}$, $\boldsymbol{\kappa}_{hom} = \mathbb{C}_{hom} : \boldsymbol{\alpha}_{hom}$ and $c_{\sigma,hom} = c_{\varepsilon,hom} + T_0 \, \boldsymbol{\alpha}_{hom} : \boldsymbol{\kappa}_{hom}$.

As demonstrated through Eqs. (3.10)-(3.13), elastic and thermoelastic problems are closely connected. Within the mean-field framework, the knowledge of elastic cracks local-

ization $\langle \mathbb{A} \rangle_{c,i}$ and concentration $\langle \mathbb{B} \rangle_{c,i}$ tensors required for the determination of elasticity tensors $\mathbb{C}_{hom}$ and $\mathbb{S}_{hom}$ are sufficient for describing the dilatometric tensors $\boldsymbol{\kappa}_{hom}$ and $\boldsymbol{\alpha}_{hom}$. Some simplifications arise for two-phase materials. Using Levin's formulae, one can express thermal strain localization and stress concentration tensors as functions of elasticity tensors. The derivation of all thermal quantities ($\boldsymbol{\kappa}_{hom}$, $\boldsymbol{\alpha}_{hom}$, $c_{\varepsilon,hom}$ and $c_{\sigma,hom}$) reduces then to the determination of a purely mechanical problem (Levin 1967, Rosen and Hashin 1970, Laws 1973, Benveniste and Dvorak 1990, Böhm 2019). When considering several families of cracks, one has to use thermal strain localization $\langle \mathbf{a} \rangle_{c,i}$ and stress concentration $\langle \mathbf{b} \rangle_{c,i}$ tensors to evaluate the specific heat capacities at constant strain or stress respectively (Laws 1973).

3.2.2 Application to the case of microcracks

In the present study, the RVE is made of an initially isotropic homogeneous matrix with stiffness and compliance given by $\mathbb{C}_m = 3k_m\,\mathbb{J} + 2\mu_m\,\mathbb{K}$ and $\mathbb{S}_m = \frac{1}{3k_m}\,\mathbb{J} + \frac{1}{2\mu_m}\,\mathbb{K}$ where k_m and μ_m are the bulk and shear modulus of the matrix respectively. Its thermal strain and thermal stress are given by $\boldsymbol{\alpha}_m = \alpha_m\,\mathbf{I}$ and $\boldsymbol{\kappa}_m = \kappa_m\,\mathbf{I}$ (α_m is the Coefficient of Thermal Expansion (CTE), $\kappa_m = 3k_m\alpha_m$) respectively. Such matrix is weakened by randomly distributed families of microcracks with random orientation (Fig. 1.1a). Such defect can be represented as a flat oblate ellipsoid (mean semi-axes a and c, Fig. 1.1b). For the i^{th} family of parallel microcracks, $\mathbf{n}_i$ denotes their unit vector normal to the crack's plane, $\omega_i = {}^{c_i}/_{a_i}$ as their mean aspect ratio, $d_i = \mathcal{N}_i\,a_i^3$ as the scalar crack density ($\mathcal{N}_i$ is the number of cracks in the i^{th} family per unit volume, Budiansky and O'Connell 1976). Moreover, penny-shaped crack configuration corresponds to the limit case of thin inclusions, so that the overall behaviour of the microcracked RVE will be established when considering $\omega_i \to 0$.

As detailed previously, closed-form expressions of thermoelastic properties can be obtained once localization and concentration tensors (i.e. $\langle \mathbb{A} \rangle_{c,i}$ and $\langle \mathbb{B} \rangle_{c,i}$ resp.) are estimated. Works of Eshelby (1957) on the single inhomogeneity problem developed for an ellipsoidal inclusion give solution to this problem. Unlike the strain and stress fields, the temperature is assumed to be uniform on the entire RVE. Also, the displacement and temperature are assumed to be continuous at the interface (i.e. crack boundary). Indeed, the strain and stress local fields in the crack can be approximated by their respective uniform local fields obtained by embedding an ellipsoidal inclusion in an infinite matrix subjected to uniform macroscopic boundary conditions denoted as $\mathbf{E}_\infty$ and $\boldsymbol{\Sigma}_\infty$. Taking all this into account, the estimated solution for finding the localization and concentration tensors $\langle \mathbb{A} \rangle_{c,i}^{est}$ and $\langle \mathbb{B} \rangle_{c,i}^{est}$ depends on the Eshelby tensor $\mathbb{S}_i^E$. Using Walpole base for transversely isotropic fourth order tensors (described in Appendix C.1, Walpole 1981), the Eshelby tensor for a penny-shaped microcrack with unit normal $\mathbf{n}_i$ and aspect ratio ω_i embedded in an isotropic matrix (ν_m its Poisson's ratio) comes to (Mura 1987, Hill 1963):

$$\mathbb{S}_i^E = \left[\frac{3}{8(1-\nu_m)}\pi\omega_i,\ 1 - \frac{1-2\nu_m}{4(1-\nu_m)}\pi\omega_i,\ \frac{7-8\nu_m}{16(1-\nu_m)}\pi\omega_i,\ 1 - \frac{2-\nu_m}{4(1-\nu_m)}\pi\omega_i, \right. \\ \left. \frac{\nu_m}{1-\nu_m} - \frac{1+4\nu_m}{8(1-\nu_m)}\pi\omega_i,\ -\frac{1-2\nu_m}{8(1-\nu_m)}\pi\omega_i \right] \tag{3.16}$$

The final step is to account for the cracks' unilateral behaviour, i.e. their ability to be either open or closed depending on the load. For both status, the cracks are considered to be isotropic ($\mathbb{C}_{c,i} = 3k_{c,i}\,\mathbb{J} + 2\mu_{c,i}\,\mathbb{K}$, $\mathbb{S}_{c,i} = \frac{1}{3k_{c,i}}\,\mathbb{J} + \frac{1}{2\mu_{c,i}}\,\mathbb{K}$, $\boldsymbol{\alpha}_{c,i} = \alpha_{c,i}\,\mathbf{I}$ and $\boldsymbol{\kappa}_{c,i} = \kappa_{c,i}\,\mathbf{I}$) but they behave differently based on the state of the crack:

- for the open case, we naturally consider that there is no elasticity i.e. $\mathbb{C}_{c,i} = \mathbb{O}$ ($k_{c,i} = 0$, $\mu_{c,i} = 0$) and no thermal strain i.e. $\boldsymbol{\alpha}_{c,i} = \mathbf{0}$ ($\alpha_{c,i} = 0$), so $\boldsymbol{\kappa}_{c,i} = \mathbf{0}$ ($\kappa_{c,i} = 0$) neither specific heat capacities at constant strain $c_{\varepsilon,c,i} = 0$ and constant stress $c_{\sigma,c,i} = 0$;

- following the works of Deudé *et al.* (2002), closed cracks are modelled as a fictitious isotropic material with bulk modulus $k_{c,i} = k_m$, shear modulus $\mu_{c,i} = 0$ (i.e. $\mathbb{C}_{c,i} = 3k_m\,\mathbb{J}$); such assumption is extended here to the thermal behaviour, that is $\alpha_{c,i} = \alpha^*$, so $\kappa_{c,i} = 3k_m\alpha^* = \kappa^*$, and $c_{\varepsilon,c,i} = c_\varepsilon^*$ and $c_{\sigma,c,i} = c_\sigma^*$. Developments are made for the general case where κ^*, α^*, c_ε^* and c_σ^* are scalars with the conditions $\kappa^* \neq 0$, $\alpha^* \neq 0$, $c_\varepsilon^* \neq 0$ and $c_\sigma^* \neq 0$. This is to ensure some level of continuity during crack closure (frictionless contact).

In what follows, the focus will be on the thermal issues, namely dilatometric tensors (Eqs. (3.12) and (3.13)) and specific heat capacities (Eqs. (3.14) and (3.15)) for microcracked media with unilateral effects. Three different homogenization approaches are derived, either for strain or stress-based framework. Related estimations of compliance and stiffness tensors (Eqs. (3.10) and (3.11)), already given in the literature, are simply recalled in Appendix C.2.

3.3 Strain-based formulation with uniform ΔT - Dilute scheme

By strain-based formulation, we mean to impose a uniform macroscopic strain $\mathbf{E}$ at the outer boundary $\delta\Omega$ and in addition the temperature difference ΔT is uniform inside the entire RVE.

We begin the calculation assuming a dilute crack density, which is to consider no interaction between cracks. Remote conditions on the Eshelby problem come in that case

to the macroscopic strain ($\mathbf{E}_\infty = \mathbf{E}$). Hence, strain localization tensor is given by:

$$\langle \mathbb{A} \rangle_{c,i}^{dil} = \left[\mathbb{I} + \mathbb{P}_i^E : \left(\mathbb{C}_{c,i} - \mathbb{C}_m \right) \right]^{-1} \tag{3.17}$$

where $\mathbb{P}_i^E = \mathbb{S}_i^E : \mathbb{S}_m$ is the first Hill tensor.

When the cracks are open, Eq. (3.17) becomes:

$$\langle \mathbb{A} \rangle_{c,i}^{dil/open} = \left[\mathbb{I} - \mathbb{S}_i^E \right]^{-1} \tag{3.18}$$

when it comes to as follows for the closed case:

$$\langle \mathbb{A} \rangle_{c,i}^{dil/closed} = \left[\mathbb{I} - \mathbb{S}_i^E : \mathbb{K} \right]^{-1} \tag{3.19}$$

Denoting $\psi_i = \dfrac{\kappa_{c,i}}{\kappa_m} = \dfrac{\alpha_{c,i}}{\alpha_m}$ and separating open ($\kappa_{c,i} = 0$, so $\psi_{c,i} = 0$) and closed ($\kappa_{c,i} = \kappa^*$ for which $\psi_{c,i} \neq 0$) families of cracks, Eq. (3.12) thus comes to:

$$\boldsymbol{\kappa}_{hom}^{dil} = \kappa_m \left[\mathbf{I} - \frac{4}{3}\pi \sum_{i/open} d_i \ \mathbf{I} : \omega_i \langle \mathbb{A} \rangle_{c,i}^{dil/open} - \frac{4}{3}\pi \sum_{i/closed} (1 - \psi_i) \ d_i \, \mathbf{I} : \omega_i \langle \mathbb{A} \rangle_{c,i}^{dil/open} \right] \tag{3.20}$$

since crack volume fraction appearing in Eqs. (3.10)-(3.15) is equal to $f_{c,i} = \frac{4}{3}\,\pi\, d_i\, \omega_i$. We can see that $\boldsymbol{\kappa}_{hom}^{dil}$ depends on the aspect ratio ω_i. In our case, cracks corresponds to the limit case of very thin inclusions. Denoting,

$$\mathbb{T}_i = \lim_{\omega_i \to 0} \ \omega_i \langle \mathbb{A} \rangle_{c,i}^{dil/open} \tag{3.21}$$

and

$$\mathbb{T}'_i = \lim_{\omega_i \to 0} \ \omega_i \langle \mathbb{A} \rangle_{c,i}^{dil/closed} \tag{3.22}$$

one has :

$$\boldsymbol{\kappa}_{hom}^{dil} = \kappa_m \left[\mathbf{I} - \frac{4}{3}\pi \sum_{i/open} d_i \ \mathbf{I} : \mathbb{T}_i - \frac{4}{3}\pi \sum_{i/closed} (1 - \psi_i) \ d_i \, \mathbf{I} : \mathbb{T}'_i \right] \tag{3.23}$$

Tensors $\mathbb{T}_i$ and $\mathbb{T}'_i$ are transversely isotropic tensors around the unit normal $\mathbf{n}_i$ of the i^{th} family of cracks. Given the related Walpole base (refer to Appendix C.1), relevant calculations provide:

$$\mathbb{T}_i = \frac{4(1-\nu_m)}{\pi} \left[0, \frac{1-\nu_m}{1-2\nu_m}, 0, \frac{1}{2-\nu_m}, \frac{\nu_m}{1-2\nu_m}, 0 \right] \tag{3.24}$$

and

$$\mathbb{T}'_i = \frac{4(1-\nu_m)}{\pi} \left[0, 0, 0, \frac{1}{2-\nu_m}, 0, 0 \right] \tag{3.25}$$

Since

$$\mathbf{I} : \mathbb{T}_i = \frac{4}{\pi}\left(\frac{1-\nu_m}{1-2\nu_m}\right)\left[(1-\nu_m)\,\mathbf{n}_i \otimes \mathbf{n}_i + \nu_m\,(\mathbf{I} - \mathbf{n}_i \otimes \mathbf{n}_i)\right] \tag{3.26}$$

$$\mathbf{I} : \mathbb{T}'_i = \mathbf{0} \tag{3.27}$$

above expression can be simplified as:

$$\boldsymbol{\kappa}^{dil}_{hom} = \kappa_m \left[\mathbf{I} - \frac{a_1}{a_2^{dil}} \sum_{i/open} d_i \left[(1-\nu_m)\,\mathbf{n}_i \otimes \mathbf{n}_i + \nu_m\,(\mathbf{I} - \mathbf{n}_i \otimes \mathbf{n}_i)\right]\right] \tag{3.28}$$

where $a_1 = \dfrac{16}{3}\left(\dfrac{1-\nu_m}{1-2\nu_m}\right)$ and $a_2^{dil} = 1$. The simple case of a single system of parallel microcracks is thus straightforward:

$$\boldsymbol{\kappa}^{dil}_{hom} = \begin{cases} \boldsymbol{\kappa}_m - \kappa_m \dfrac{a_1}{a_2^{dil}}\, d\, \left[\left(1-\nu_m\right)\mathbf{n}\otimes\mathbf{n} + \nu_m\left(\mathbf{I} - \mathbf{n}\otimes\mathbf{n}\right)\right] & \text{, if cracks are open} \\ \boldsymbol{\kappa}_m & \text{, if cracks are closed} \end{cases} \tag{3.29}$$

Regarding the effective specific heat, expression of thermal strain localization $\langle \mathbf{a} \rangle_{c,i}$ tensor for multiphase medium has been established by Benveniste *et al.* (1991) from a decomposition procedure of thermal and mechanical loads (see also Benveniste and Dvorak 1990). For the dilute case, one has:

$$\langle \mathbf{a} \rangle^{dil}_{c,i} = \left(\mathbb{I} - \langle \mathbb{A} \rangle^{dil}_{c,i}\right) : \left(\mathbb{C}_{c,i} - \mathbb{C}_m\right)^{-1} : \left(\boldsymbol{\kappa}_{c,i} - \boldsymbol{\kappa}_m\right) \tag{3.30}$$

Since $\mathbb{C}_{c,i} - \mathbb{C}_m = -\mathbb{C}_m$ (respectively $\mathbb{C}_{c,i} - \mathbb{C}_m = -\mathbb{C}_m : \mathbb{K} = -2\mu_m\mathbb{K}$) for open (resp. closed) state of microcracks, Eq. (3.14) can thus be written on the form for thin inclusions:

$$c^{dil}_{\varepsilon,hom} = c_{\varepsilon,m} - \frac{4}{3}\,\pi\,T_0\,\kappa_m^2 \left(\sum_{i/open} d_i X_i + \sum_{i/closed} d_i (1-\psi_i)^2 X'_i\right) \tag{3.31}$$

where

$$X_i = \lim_{\omega_i \to 0}\ \omega_i\, \mathbf{I} : \left(\mathbb{I} - \langle \mathbb{A} \rangle^{dil/open}_{c,i}\right) : \mathbb{C}_m^{-1} : \mathbf{I} = -\mathbf{I} : \mathbb{T}_i : \mathbb{C}_m^{-1} : \mathbf{I} = -\frac{4}{\pi}\,\frac{\alpha_m}{\kappa_m}\,\frac{1+\nu_m^2}{1-2\nu_m} \tag{3.32}$$

and

$$X'_i = \lim_{\omega_i \to 0}\ \omega_i\, \mathbf{I} : \left(\mathbb{I} - \langle \mathbb{A} \rangle^{dil/closed}_{c,i}\right) : \left(-2\mu_m\mathbb{K}\right)^{-1} : \mathbf{I} = -\mathbf{I} : \mathbb{T}'_i : \left(2\mu_m\mathbb{K}\right)^{-1} : \mathbf{I} \tag{3.33}$$

Though the calculation of X_i remains simple, a problem arises for the case of X'_i since $(2\mu_m\mathbb{K})^{-1}$ is not defined. As suggested by Dormieux and Kondo (2009), the idea to get around this is to introduce a function $\mathbb{F}(b) = (b\mathbb{J} + 2\mu_m\mathbb{K})^{-1}$, not defined in $b = 0$, but

such that $\mathbb{F}(b) \to (2\mu_m \mathbb{K})^{-1}$ when $b \to 0$. Since,

$$\mathbb{T}'_i : \mathbb{F}(b) = \frac{2(1-\nu_m)}{\mu_m \, \pi} \left[0, 0, 0, \frac{1}{2-\nu_m}, 0, 0\right] \tag{3.34}$$

does not depend on $b \neq 0$, we can thus show that:

$$\mathbb{T}'_i : \mathbb{F}(b) : \mathbf{I} = \mathbf{0} \tag{3.35}$$

and $X'_i = 0$. Overall specific heat at constant strain is finally provided by:

$$c^{dil}_{\varepsilon,hom} = c_{\varepsilon,m} + a_1(1+\nu_m) \; T_0 \; \alpha_m \, \kappa_m \sum_{i/open} d_i \tag{3.36}$$

In the special case of one family (see Appendix C.3.1), one gets easily:

$$c^{dil}_{\varepsilon,hom} = \begin{cases} c_{\varepsilon,m} + T_0 \; \alpha_m \, \kappa_m \, \dfrac{a_1}{a_2^{dil}} \; d \; (1+\nu_m) & \text{, if cracks are open} \\ c_{\varepsilon,m} & \text{, if cracks are closed} \end{cases} \tag{3.37}$$

3.4 Strain-based formulation with uniform ΔT - Mori-Tanaka scheme

As interpreted by Benveniste (1987), the Mori-Tanaka (MT) scheme (Mori and Tanaka 1973) accounts for some interactions between cracks by considering the defects embedded in an infinite media (with matrix properties) that is subjected to the average strain over the matrix phase ($\mathbf{E}_\infty = \langle \boldsymbol{\varepsilon} \rangle_m$). Averaging rule (3.5) leads to the following localization tensor:

$$\langle \mathbb{A} \rangle^{MT}_{c,i} = \langle \mathbb{A} \rangle^{dil}_{c,i} : \left[f_m \, \mathbb{I} + \sum_{j=1}^{N} f_{c,j} \; \langle \mathbb{A} \rangle^{dil}_{c,j} \right]^{-1} = \langle \mathbb{A} \rangle^{dil}_{c,i} : \mathbb{G} \tag{3.38}$$

From Eq. (3.12), it comes:

$$\boldsymbol{\kappa}^{MT}_{hom} = \kappa_m \mathbf{I} : \left[\mathbb{G}^{-1} - \frac{4}{3}\pi \sum_{i/open} d_i \mathbb{T}_i - \frac{4}{3}\pi \sum_{i/closed} d_i (1-\psi_i) \mathbb{T}'_i \right] : \mathbb{G} = \kappa_m \mathbf{I} : \mathbb{X} : \mathbb{G} \tag{3.39}$$

where

$$\mathbb{X} = \mathbb{I} + \frac{4}{3}\pi \sum_{i/closed} d_i \psi_i \mathbb{T}'_i \tag{3.40}$$

Due to condition (3.27), $\mathbf{I} : \mathbb{X} = \mathbf{I}$. Moreover, $\mathbb{G}$ comes to:

$$\mathbb{G} = \left[\mathbb{I} + \frac{4}{3}\pi \sum_{i/open} d_i \, \mathbb{T}_i + \frac{4}{3}\pi \sum_{i/closed} d_i \, \mathbb{T}'_i \right]^{-1} \tag{3.41}$$

At last, the effective thermal strain tensor for the Mori-Tanaka scheme writes:

$$\boldsymbol{\kappa}_{hom}^{MT} = \boldsymbol{\kappa_m} : \left[\mathbb{I} + \frac{4}{3}\pi \sum_{i/open} d_i \, \mathbb{T}_i + \frac{4}{3}\pi \sum_{i/closed} d_i \, \mathbb{T}'_i \right]^{-1} \tag{3.42}$$

One could note that for a single family of cracks, Eq. (3.42) becomes:

$$\boldsymbol{\kappa}_{hom}^{MT} = \begin{cases} \boldsymbol{\kappa}_m - \kappa_m \dfrac{a_1}{a_2^{MT}} \, d \, \left[(1-\nu_m) \, \mathbf{n} \otimes \mathbf{n} + \nu_m (\mathbf{I} - \mathbf{n} \otimes \mathbf{n}) \right] & \text{, if cracks are open} \\ \boldsymbol{\kappa}_m & \text{, if cracks are closed} \end{cases} \tag{3.43}$$

where $a_2^{MT} = 1 + (1-\nu_m) \, a_1 \, d$.

Again, the heat capacity estimation requires the expression of the thermal strain localization tensor. For the Mori-Tanaka model, expression of $\langle \mathbf{a} \rangle_{c,i}$ is also provided by Benveniste *et al.* (1991) for several inclusions :

$$\langle \mathbf{a} \rangle_{c,i}^{MT} = \langle \mathbf{a} \rangle_{c,i}^{dil} - \langle \mathbb{A} \rangle_{c,i}^{MT} : \left(\sum_{j=1}^{N} f_{c,j} \, \langle \mathbf{a} \rangle_{c,j}^{dil} \right) = \langle \mathbf{a} \rangle_{c,i}^{dil} - \langle \mathbb{A} \rangle_{c,i}^{MT} : \mathbf{M} \tag{3.44}$$

Combining such tensor with expression (3.14) of the overall specific heat capacity and considering the limit case $\omega_i \to 0$ associated with condition (3.27), we can show that :

$$c_{\varepsilon,hom}^{MT} = c_{\varepsilon,hom}^{dil} + \frac{4}{3}\pi \, T_0 \, \kappa_m \sum_{i/open} d_i \, \mathbf{I} : \mathbb{T}_i : \mathbb{G} : \mathbf{M} \tag{3.45}$$

with tensor $\mathbb{G}$ given in Eq. (3.41). In line with dilute solution, a similar methodology based on function $\mathbb{F}(b)$ for closed case and condition (3.35) lead to following simplied form of second order tensor $\mathbf{M}$:

$$\mathbf{M} = -a_1(1+\nu_m) \, \alpha_m \sum_{j/open} d_j \, \mathbf{n}_j \otimes \mathbf{n}_j \tag{3.46}$$

It comes finally:

$$\begin{aligned} c_{\varepsilon,hom}^{MT} = c_{\varepsilon,hom}^{dil} - a_1^2 \, T_0 \, (1+\nu_m) \, \alpha_m \, \kappa_m \times \\ \sum_{i/open} d_i \Big[(1-\nu_m) \mathbf{n}_i \otimes \mathbf{n}_i + \nu_m (\mathbf{I} - \mathbf{n}_i \otimes \mathbf{n}_i) \Big] : \mathbb{G} : \sum_{j/open} d_j \, \mathbf{n}_j \otimes \mathbf{n}_j \end{aligned} \tag{3.47}$$

When considering a single cracks family (see Appendix C.3.2), Eq. (3.47) writes:

$$c_{\varepsilon,hom}^{MT} = \begin{cases} c_{\varepsilon,m} + T_0 \, \alpha_m \, \kappa_m \, \dfrac{a_1}{a_2^{MT}} \, d \, (1+\nu_m) & \text{, if cracks are open} \\ c_{\varepsilon,m} & \text{, if cracks are closed} \end{cases} \tag{3.48}$$

It should be noted that results given in Eqs. (3.29) and (3.37) for dilute scheme and (3.43) and (3.48) for Mori-Tanaka scheme in the particular case of a single system of cracks (corresponding to binary composite) can also be obtained through the application of Levin's approach.

3.5 Strain-based formulation with uniform ΔT - Ponte Castañeda-Willis upper bound

Ponte Castañeda and Willis (PCW) have applied Hashin-Shtrikman variational principles for composite materials with ellipsoidal inclusions. From this, they provided an explicit strain-based upper bound for the effective stiffness (Ponte Castañeda and Willis 1995). Their formulation also accounts for the inclusion shape and spatial distribution independently by means of fourth order interaction $\mathbb{P}_j^E$ and spatial crack distribution $\mathbb{S}_c^d$ $\left(=\mathbb{P}_c^d : \mathbb{C}_m\right)$ tensors respectively. In this estimate, the strain localization tensor can be written as:

$$\langle \mathbb{A} \rangle_{c,i}^{PCW} = \langle \mathbb{A} \rangle_{c,i}^{dil} : \left(f_m \, \mathbb{I} + \sum_{j=1}^{N} f_{c,j} \left[\mathbb{I} + \left(\mathbb{P}_j^E - \mathbb{P}_c^d \right) : \left(\mathbb{C}_{c,j} - \mathbb{C}_m \right) \right] : \langle \mathbb{A} \rangle_{c,j}^{dil} \right)^{-1} = \langle \mathbb{A} \rangle_{c,i}^{dil} : \mathbb{H} \tag{3.49}$$

We assume the spatial distribution to be spherical and for such case the fourth order isotropic tensor $\mathbb{P}_c^d$ can be expressed as:

$$\mathbb{P}_c^d = \frac{\beta_1}{3k_m}\mathbb{J} + \frac{\beta_2}{2\mu_m}\mathbb{K} \quad \text{with} \quad \beta_1 = \frac{1}{3}\left(\frac{1+\nu_m}{1-\nu_m}\right) \quad \text{and} \quad \beta_2 = \frac{2}{15}\left(\frac{4-5\nu_m}{1-\nu_m}\right) \tag{3.50}$$

From expression of $\langle \mathbb{A} \rangle_{c,i}^{dil}$, tensor $\mathbb{H}$ is as follows:

$$\mathbb{H}^{-1} = \mathbb{I} - \sum_{j=1}^{N} f_{c,j} \, \mathbb{P}_c^d : \left(\mathbb{C}_{c,j} - \mathbb{C}_m \right) : \langle \mathbb{A} \rangle_{c,j}^{dil} \tag{3.51}$$

Since $\mathbb{P}_c^d = \mathbb{S}_c^d : \mathbb{C}_m^{-1}$ and $\mathbb{S}_c^d : \mathbb{K} = \beta_2 \, \mathbb{K}$, Eq. (3.51) can be simplified in:

$$\mathbb{H}^{-1} = \mathbb{I} + \frac{4}{3}\pi \sum_{j/open} d_j \, \mathbb{S}_c^d : \mathbb{T}_j + \frac{4}{3}\pi \sum_{j/closed} \beta_2 \, d_j \, \mathbb{T}'_j \tag{3.52}$$

where it should be noted that:

$$\mathbb{T}'_i = \lim_{\omega_i \to 0} \omega_i \, \langle \mathbb{A} \rangle_{c,i}^{dil/closed} = \lim_{\omega_i \to 0} \omega_i \, \mathbb{K} : \langle \mathbb{A} \rangle_{c,i}^{dil/closed} \tag{3.53}$$

In that case and always under condition (3.27), the effective thermal strain tensor of Eq. (3.12) is given by:

$$\boldsymbol{\kappa}_{hom}^{PCW} = \boldsymbol{\kappa}_m : \left[\mathbb{I} - \frac{4}{3}\pi \left(\sum_{i/open} d_i \, \mathbb{T}_i \right) : \left(\mathbb{I} + \frac{4}{3}\pi \sum_{j/open} d_j \, \mathbb{S}_c^d : \mathbb{T}_j + \frac{4}{3}\pi \sum_{j/closed} \beta_2 \, d_j \, \mathbb{T}'_j \right)^{-1} \right] \tag{3.54}$$

Eq. (3.54) for a single family of cracks can be simplified as:

$$\boldsymbol{\kappa}_{hom}^{PCW} = \begin{cases} \boldsymbol{\kappa}_m - \kappa_m \dfrac{a_1}{a_2^{PCW}} \, d \, \left[(1-\nu_m) \, \mathbf{n} \otimes \mathbf{n} + \nu_m (\mathbf{I} - \mathbf{n} \otimes \mathbf{n}) \right] & \text{, if cracks are open} \\ \boldsymbol{\kappa}_m & \text{, if cracks are closed} \end{cases} \tag{3.55}$$

where $a_2^{PCW} = 1 + \dfrac{a_1 \, d}{15 \, (1-\nu_m)} \, [7 \, (1 - 2\nu_m) + 15\nu_m^2]$.

The determination of the thermal strain localization tensor $\langle \mathbf{a} \rangle_{c,i}^{PCW}$ in the case of multiphase media is a complex issue. It requires the extension to the case of thermoelasticity of the variational structure of Hashin-Shtrikman in the form of Willis (1977) which is based on energy minimization. Recent works of Fernández and Böhlke (2018), Valdiviezo-Mijangos *et al.* (2020) may help in this sense to explicitly develop Eq. (3.14) for the PCW estimate. In the present paper, the calculation will be limited to the case of a single family of cracks. For such a case of two-phase composite, combining first part of Eq. (3.12) with consistency conditions (3.7) allows to express the localisation tensor (Ponte Castañeda 2002, Willis 2002):

$$\langle \mathbf{a} \rangle_c^{PCW} = - \left(\mathbb{C}_c - \mathbb{C}_m \right)^{-1} : \left(\langle \mathbb{A} \rangle_c^{PCW} - \mathbb{I} \right)^T : \left(\boldsymbol{\kappa}_c - \boldsymbol{\kappa}_m \right) \tag{3.56}$$

where T denotes the transpose. When such a tensor is implemented inside Eq. (3.14), the open case can simply derived. However, contribution due to closed cracks depends linearly on $\mathbf{I} : (2\mu_m \mathbb{K})^{-1} : (\mathbb{T}' : \mathbb{H})^T : \mathbf{I}$ which is not defined. Using the function $\mathbb{F}(b)$ again solves the problem. It can be shown that $\mathbb{F}(b) : (\mathbb{T}' : \mathbb{H})^T$ does not depend on $b \neq 0$ and moreover that

$$\mathbb{F}(b) : (\mathbb{T}' : \mathbb{H})^T : \mathbf{I} = \mathbf{0} \tag{3.57}$$

From this, one gets (see Appendix C.3.3):

$$c_{\varepsilon,hom}^{PCW} = \begin{cases} c_{\varepsilon,m} + T_0 \, \alpha_m \, \kappa_m \dfrac{a_1}{a_2^{PCW}} \, d \, (1+\nu_m) & \text{, if cracks are open} \\ c_{\varepsilon,m} & \text{, if cracks are closed} \end{cases} \tag{3.58}$$

Note that the model of Mori-Tanaka (Eqs. (3.43) and (3.48)) and the bound of Ponte Castañeda-Willis (Eqs. (3.55) and (3.58)) tend to the dilute prediction (Eqs. (3.29) and (3.37) respectively) when $d \to 0$. As the microcracks density increases, the influence of defect interactions leads to greater differences between models. As an illustration, Fig.

3.1 shows the evolution of the quantity $\frac{a_1}{a_2}d$ which characterizes the dependency of $\boldsymbol{\kappa}_{hom}$ and $c_{\varepsilon,hom}$ with microcracks density in the different models.

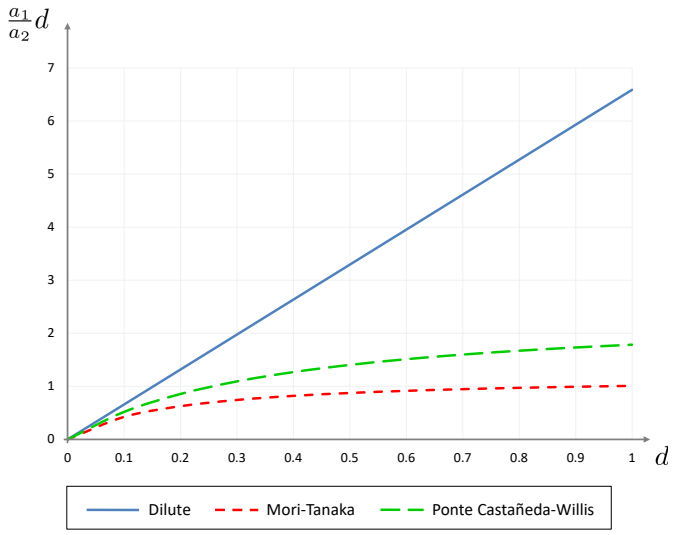

FIGURE 3.1: Influence of the crack density d on the ratio $\frac{a_1}{a_2}d$ for various models for a single family of cracks.

Some comments arise from the results obtained by means of strain-based formulation. Even though there are differences between the models, the dependency of thermoelastic properties upon the cracks orientation and unilateral behaviour were observed through all modeling approches. First, it is to note that the microcracked medium exhibits some induced anisotropy in its effective thermoelastic response. Such behaviour is highlighted through the second order thermal strain tensor and can be attributed to open cracks orientation for dilute case (Eq. (3.29)) and to both open and closed cracks orientations for MT (Eq. (3.43)) and PCW bound (Eq. (3.55)). The case of a single family of cracks leads for instance to a transverse isotropy around the normal $\mathbf{n}$ of defects. For all estimates, only open cracks influence the specific heat at constant strain, obviously in a scalar form. Moreover, the account of the unilateral effect allows to show that cracks closure tends to some recovery of the initial properties, both on thermal strain and specific heat. Unlike the pure elastic properties (Welemane and Cormery 2002), closed cracks do not affect the effective thermoelastic properties. This leads for instance to a total recovery of these properties in the particular case of a single system of parallel microcracks, with a thermoelastic response equal to that of the virgin matrix. Although it is strongly related to elasticity, the problem of thermoelastic properties has a strong analogy with that of steady-state heat conduction (Chapter 1). Like the latter, the degree of complexity ($\boldsymbol{\kappa}$ and $\boldsymbol{\alpha}$ of second order, c_ε and c_σ scalar) is less than that of the elastic problem ($\mathbb{C}$ and $\mathbb{S}$ of fourth order). Unlike the Eshelby-like tensor (depolarization tensor) which depends only on the crack shape (Eqs. (1.15) and (2.1)), the Eshelby tensor used for thermoelastic problem (also for elastic problem) depends on both crack shape and matrix properties (Eq. (3.16)). Yet, we lose information due to the contraction between second and fourth order tensors. This explains in particular the cancellation of the effects of closed microcracks.

3.6 Stress-based formulation with uniform ΔT

This section is dedicated to the derivation of thermoelastic effective quantities when considerind stress-based boundary conditions at $\delta\Omega$. Estimates and bound will now be based on the local fields induced by cracks embedded inside the matrix with uniform stress at infinity ($\boldsymbol{\Sigma}_\infty$) and uniform ΔT inside the RVE. Accordingly, the strain $\boldsymbol{\varepsilon}(x)$ tends to $\mathbb{S}_m : \boldsymbol{\Sigma}_\infty$ when $|x| \to \infty$. This makes the connection with strain boundary conditions considered in the Eshelby approach. From the average stress in this phase $\langle\boldsymbol{\sigma}\rangle_c = \mathbb{C}_c : \langle\boldsymbol{\varepsilon}\rangle_c$, estimates of concentration tensor $\mathbb{B}$ defined in Eq. (3.6) can be derived.

For the dilute scheme, conditions at infinity correspond to the macroscopic heat flux ($\boldsymbol{\Sigma}_\infty = \boldsymbol{\Sigma}$). So that:

$$\langle\mathbb{B}\rangle_{c,i}^{dil} = \mathbb{C}_{c,i} : \langle\mathbb{A}\rangle_{c,i}^{dil} : \mathbb{S}_m \tag{3.59}$$

In the model of Mori-Tanaka, the remote conditions correspond to the average stress over the matrix phase ($\boldsymbol{\Sigma}_\infty = \langle\boldsymbol{\sigma}\rangle_m$) and again, using the average rule, the stress concentration tensor is given by:

$$\langle\mathbb{B}\rangle_{c,i}^{MT} = \langle\mathbb{B}\rangle_{c,i}^{dil} : \left[f_m\, \mathbb{I} + \sum_{j=1}^{N} f_{c,j}\, \langle\mathbb{B}\rangle_{c,j}^{dil} \right]^{-1} = \langle\mathbb{B}\rangle_{c,i}^{dil} : \mathbb{G}' \tag{3.60}$$

As inspired by Ponte Castañeda and Willis (1995), Dormieux and Kondo (2009) derived a variational stress-based lower bound for the effective compliance using an energy approach. The stress concentration tensor for this case can be given by:

$$\langle\mathbb{B}\rangle_{c,i}^{PCW} = \langle\mathbb{B}\rangle_{c,i}^{dil} : \left(f_m\, \mathbb{I} + \sum_{j=1}^{N} f_{c,j} \left[\mathbb{I} + \left(\mathbb{Q}_j^E - \mathbb{Q}_c^d\right) : \left(\mathbb{S}_{c,j} - \mathbb{S}_m\right) \right] : \langle\mathbb{B}\rangle_{c,j}^{dil} \right)^{-1} = \langle\mathbb{B}\rangle_{c,i}^{dil} : \mathbb{H}' \tag{3.61}$$

where $\mathbb{Q}_i^E = \mathbb{C}_m - \mathbb{C}_m : \mathbb{P}_i^E : \mathbb{C}_m$ is the second Hill tensor and $\mathbb{Q}_c^d = \mathbb{C}_m - \mathbb{C}_m : \mathbb{P}_c^d : \mathbb{C}_m$. In the particular case of thin inclusions ($\omega_i \to 0$), it can be demonstrated that $\mathbb{G}' = \mathbb{H}' = \mathbb{I}$ and:

$$\langle\mathbb{B}\rangle_{c,i}^{dil/open} = \mathbb{O} \quad \text{and} \quad \langle\mathbb{B}\rangle_{c,i}^{dil/closed} = \mathbb{J} \tag{3.62}$$

Accordingly, this leads to strong simplifications for the thermal stress tensor, namely:

$$\boldsymbol{\alpha}_{hom}^{dil} = \boldsymbol{\alpha}_{hom}^{MT} = \boldsymbol{\alpha}_{hom}^{PCW} = \boldsymbol{\alpha}_m \tag{3.63}$$

In a complete analogous way, thermal stress concentration tensors required for the derivation of specific heat at constant stress may be defined (Laws 1973, Benveniste and Dvorak 1990, Benveniste *et al.* 1991):

$$\langle\mathbf{b}\rangle_{c,i}^{dil} = -\left(\mathbb{I} - \langle\mathbb{B}\rangle_{c,i}^{dil}\right) : \left(\mathbb{S}_{c,i} - \mathbb{S}_m\right)^{-1} : \left(\boldsymbol{\alpha}_{c,i} - \boldsymbol{\alpha}_m\right) \tag{3.64}$$

$$\langle \mathbf{b} \rangle_{c,i}^{MT} = \langle \mathbf{b} \rangle_{c,i}^{dil} - \langle \mathbb{B} \rangle_{c,i}^{MT} : \left(\sum_{j=1}^{N} f_{c,j} \, \langle \mathbf{b} \rangle_{c,j}^{dil} \right) \tag{3.65}$$

Moreover, for the case of a single family, we find from (3.7) and (3.13) the PCW formulation:

$$\langle \mathbf{b} \rangle_{c}^{PCW} = (\mathbb{S}_c - \mathbb{S}_m)^{-1} : \left(\langle \mathbb{B} \rangle_{c}^{PCW} - \mathbb{I} \right)^{T} : (\boldsymbol{\alpha}_c - \boldsymbol{\alpha}_m) \tag{3.66}$$

From (3.62), we thus get:

$$\langle \mathbf{b} \rangle_{c,i}^{dil} = \langle \mathbf{b} \rangle_{c,i}^{MT} = \langle \mathbf{b} \rangle_{c}^{PCW} = \mathbf{0} \tag{3.67}$$

whether the microcracks are open or closed, and then for the effective specific heat:

$$c_{\sigma,hom}^{dil} = c_{\sigma,hom}^{MT} = c_{\sigma,hom}^{PCW} = c_{\sigma,m} \tag{3.68}$$

It is thus shown that microcracks does not affect thermoelastic properties established by means of stress-based formulation, i.e. both dilatation and specific heat at constant stress, for the three considered estimates.

3.7 Conclusion

Given the classical mean-field framework, homogenization techniques have been used to calculate closed-form expressions of thermoelastic properties of microcracked media. Specially, strain and stress-based thermal tensors and heat capacities have been implemented for dilute and Mori-Tanaka schemes and for Ponte Castañeda-Willis bound.

For strain-based formulation, the specific features of microcracks influence the material thermoelastic response, both regarding their orientation (induced anisotropy) and their unilateral effect (recovery phenomena at the closure of microcracks). These tendencies were obtained for the three modelling approaches. On the other hand, stress-based boundary conditions lead to estimates of effective properties equal to those of the virgin material, showing no influence of microcracking.

The explicit derivation of these quantities in the specific case of cracks-like inclusion, either open or closed, thus provides a theoretical basis that can be compared either to experimental or numerical characterizations.

Chapter 4

Numerical simulation of thermal and thermoelastic properties

Abstract

This chapter will have collection of simulations based on Finite Element Modelling in 3D, on the thermal and thermoelastic properties. Current chapter is the numerical counterpart of the homogenization estimates of the Chapters 1 and 3. Following boundary conditions used in said chapters, the homogenized properties are predicted. To be consistent with theoretical approach similar assumptions are made here. The results are given for a RVE with a single family of parallel microcracks. The influence of the density of cracks, size, orientation and unilateral effect are all discussed. Finally, the results are compared with the theoretical expressions.

A self-consistent notation is adopted.

4.1 Introduction

This chapter intends to propose a comparison of previous theoretical results with numerical modelling. As discussed in the General introduction, much of the work on numerical homogenization of microcracking issues is based on FEM. It is productive for the cases of thermal and elastic problems which is the interest of this work. On the other hand, the software used (ABAQUS) allows efficient management of the construction of complex geometries, their meshing, their interaction between different volumes/parts of the model and their userfriendly interface. Visualizations produced by the software also make it easier to interpret the results.

4.2 Numerical framework

The simulated volume V is a cube with size 1 m^3 (V = 1 m $\times$1 m $\times$1 m). Let $(\mathbf{t}, \mathbf{v}, \mathbf{k})$ be their coordinate system, which corresponds to $(\mathbf{X}, \mathbf{Y}, \mathbf{Z})$ of ABAQUS. The matrix is a 3D solid with its own properties. If there are $\mathcal{N}$ cracks in the RVE, then the crack radius a can be found by $a = \sqrt[3]{d/\mathcal{N}}$, d being the scalar density of cracks. They are modelled as a thin oblate penny-shaped inclusions with normal $\mathbf{n}$ (Fig. 4.1a). Their aspect ratio $\omega = c/a$ is small, such that $\omega \ll 1$. The properties of the inclusions define if the cracks are open or closed. The open cracks are defined as non-conductive and with zero stiffness, while the closed cracks are considered having fictitious scalar properties for both the thermal and elastic properties. This assumption of the crack geometry and the unilateral effect is in line with the theoretical framework.

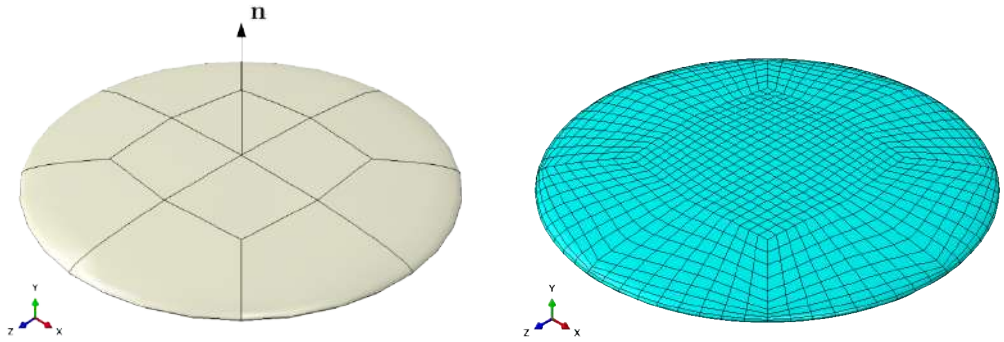

(a) (b)

FIGURE 4.1: Crack (a) geometry, (b) structured meshing in ABAQUS, with $\omega = 0.1$.

The cracks are randomly positioned inside the RVE in way they are not close to the edges (to prevent edge effects) and not too close to each other. Since the cracks are bigger, it is not possible to respect the spherical distribution like in 2D (Fig. 2.2), so elliptical distribution corresponding to MT is used. For the study, 10 cracks of equal shape and size are considered (Fig. 4.2). The RVE is obtained by combining the matrix and crack parts together. Due to their very thin shape, meshing the ellipsoidal inclusion is challenging. To facilitate smooth meshing, the inclusion is partitioned to provide a

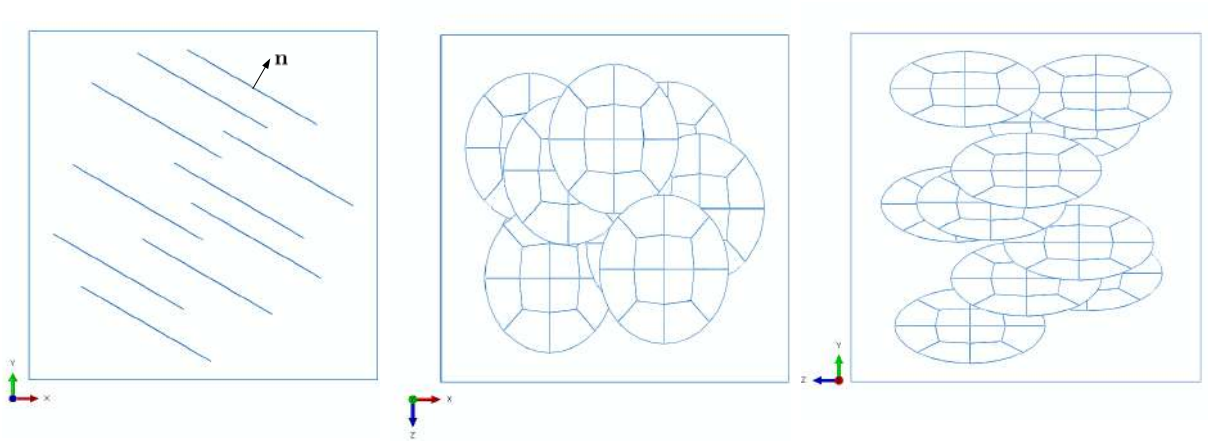

(a) (b) (c)

FIGURE 4.2: Different views showing the distribution of cracks in the simulated RVE for crack orientation $(\mathbf{n}, \mathbf{v}) = 30°$ with aspect ratio $\omega = 0.001$.

structured mesh (Fig. 4.1b). The partitions allow one to have the same mesh in all cracks and to have the same mesh distribution for different values of the aspect ratio. The finite element type used for the cracks is quadratic hexahedral while quadratic tetrahedral is used for the matrix (Fig. 4.3). Indeed, the number and arrangement of the cracks inside the matrix make it a complex volume that it is not possible to mesh otherwise than using a free meshing method associated to tetrahedral elements. The models have meshes upto 800000 elements and 1200000 nodes including 1681 (referred as N) nodes in each outer face. It should be noted that hexahedral (used for cracks) and tetrahedral (used for matrix) element shapes are incompatible, i.e. some nodes of neighbouring elements do not match. So, to ensure the continuity of the material (mesh), additional coupling equations must be created increasing the problem size. Simulations tests were performed to ensure that this method does not influence the results.

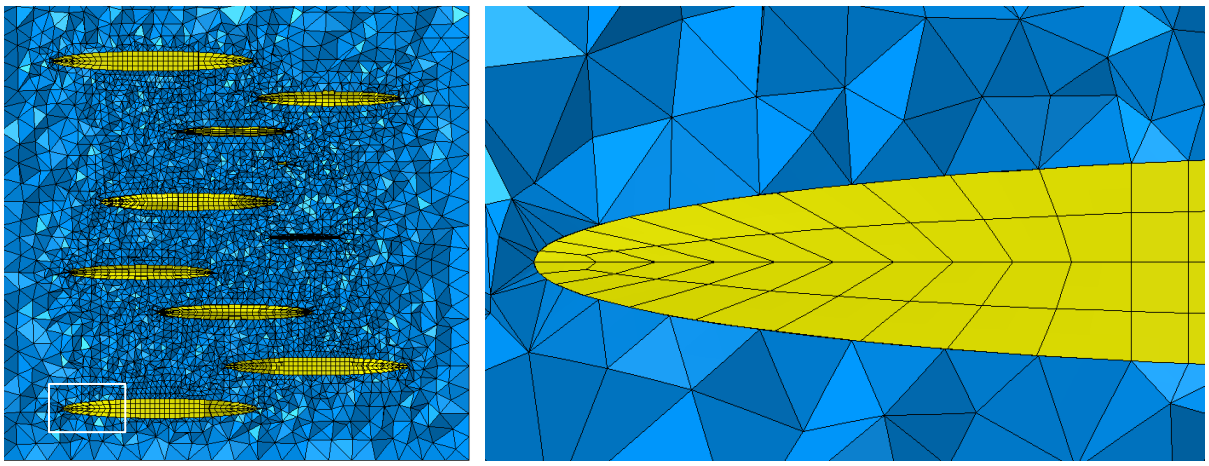

(a) Global mesh (b) Magnification around a crack tip

FIGURE 4.3: Mid cut section view of the simulated RVE showing the mesh, with $\omega = 0.1$ and $(\mathbf{n}, \mathbf{v}) = 0°$.

Same model (part) is used for all following analyzes with changes in boundary conditions, materials properties and output requests based on ones requirements. Unless specifically mentioned, the closed cracks are assumed to have 50% of the matrix property and all cracks are modelled with aspect ratio $\omega = 10^{-3}$ and density $d = 0.1$ (corresponding to $f_c = 0.04\%$). All simulations are performed in a predefined initial temperature field, $T_0 = 293$ K. Calculations were carried out with different multiprocessing servers with 24 to 32 cores having 64 to 128 GB of RAM. With 4 cores, the time duration of the thermal calculations are between 300 and 700 s, whereas the thermoelastic simulations with 12 cores take 890 to 4000 s.

More than 150 simulations were run to analyze the following influence cracks have on the effective properties:

- crack orientation $(\mathbf{n}, \mathbf{v}) = \{0°, 15°, 30°, 45°, 60°, 75°, 90°\}$
  − as in Chapter 2, cracks were rotated as a group and centred (the rotation of the cracks has only been studied in one plane, i.e. $(\mathbf{t}, \mathbf{v})$);

- influence of the density of cracks $d = \{0.05, 0.1\}$
  − cracks with different radius $a = 0.171$ m (for $d = 0.05$), $a = 0.215$ m (for $d = 0.1$);

- influence of the aspect ratio of cracks $\omega = \{0.001, 0.005, 0.01, 0.1, 0.2\}$
  − cracks with different minor radius $c = \omega\, a$, and $a = 0.215$ m, same crack element size considered for all aspect ratios used, analyzed only for the most critical angle $(\mathbf{n}, \mathbf{v}) = 0°$;

- influence of crack status : open or closed cracks
  − achieved through changing the crack property;

- influence of scalar closed crack properties
  − different closed crack property from $\{1, 5, 10, 25, 50, 80, 100\}[\%]$ of the matrix property, analyzed only for the most critical angle $(\mathbf{n}, \mathbf{v}) = 0°$.

Note that graphs in this chapter are given for 3 theoretical models (Dilute, MT, PCW) and simulations performed. Furthermore, since 3D simulations respect ellipsoidal crack distribution, the numerical results thus obtained can only be compared to dilute and MT.

4.3 Thermal conductivity

In the thermal problem, the finite element type used for the matrix and cracks are diffusive heat transfer second order elements namely DC3D10 and DC3D20 respectively. Let the scalar conductivity of the matrix be $\lambda_m = 180$ W/m/K. The open cracks are non-conductive, i.e. the scalar conductivity $\lambda_c = 0$. The closed cracks are conductive with conductivity $\lambda_c = \lambda^* \neq 0$. Just like Section 1.3 of the theoretical framework,

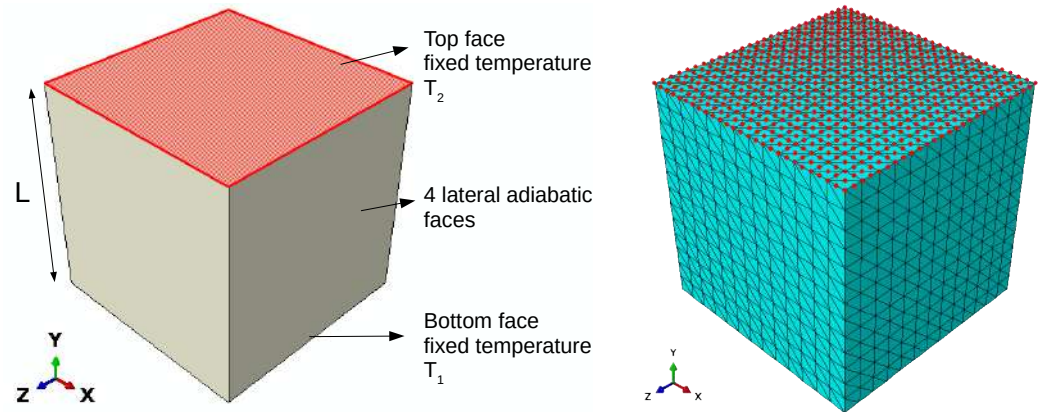

(a) (b)

FIGURE 4.4: Simulated RVE showing (a) the gradient boundary condition, (b) outer face nodes used for extracting results.

uniform temperature gradient $G\left(=G_{\mathbf{v}}\,\mathbf{v}=\frac{\Delta T_{\mathbf{v}}}{L}\,\mathbf{v}\right)$ is imposed to find the effective conductivity of the RVE. This boundary condition can be realized by applying temperatures $T_2 = 373$ K and $T_1 = 293$ K ($\Delta T_{\mathbf{v}} = T_2 - T_1 = 80$ K > 0) respectively on the top and bottom faces (with outward normals $\pm\,\mathbf{v}$) of the RVE (Fig. 4.4a). This difference in temperature creates a heat flux $Q(=Q_{\mathbf{t}}\,\mathbf{t}+Q_{\mathbf{v}}\,\mathbf{v}+Q_{\mathbf{k}}\,\mathbf{k})$ inside the RVE. Due to the adiabatic condition on the 4 lateral faces, the flux is mostly oriented in $\mathbf{v}$ direction. Recalling the numerical effective conductivity in the direction $\mathbf{v}$:

$$\lambda^{\text{num}}(\mathbf{v}) = \frac{Q_{\mathbf{v}}}{G_{\mathbf{v}}} \tag{4.1}$$

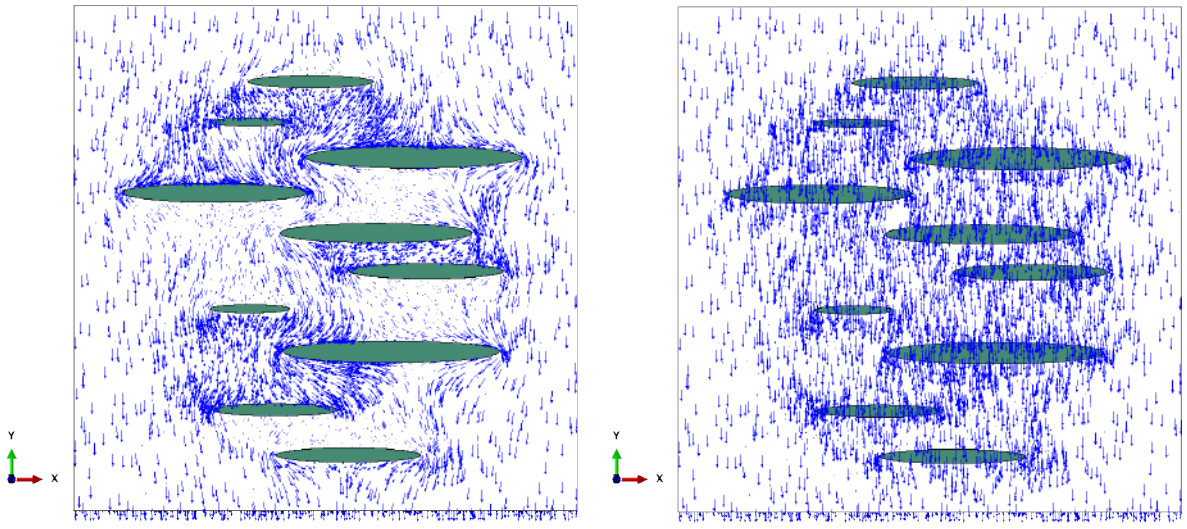

(a) Open crack (b) Closed crack ($\lambda^* = 50\%\ \lambda_m$)

FIGURE 4.5: Heat flux vectors at integration points in the mid cut section of the simulated RVE for $(\mathbf{n},\mathbf{v}) = 0°$; $d = 0.1$ m; $a = 0.215$ m; $\omega = 0.1$.

where $Q_{\mathbf{v}}$ is the average heat flux on the face ($+\mathbf{v}$ or $-\mathbf{v}$) along $\mathbf{v}$ direction. This quantity can be found using the Reaction flux RFL_i calculated on each node i on the top (Fig. 4.4b) or bottom face (with area A), $Q_{\mathbf{v}} = \dfrac{1}{A}\sum_{i=1}^{N} \mathrm{RFL}_i$.

Fig. 4.5 shows the heat flux through the cut section of the RVE. Just like in 2D case (Fig. 2.6a), here also the non-conductive cracks act as a thermal barrier significantly disrupting the flux (Fig. 4.5a). On the other hand in Fig. 4.5b, for the conductive closed cracks, heat flux vectors are not deviated by the cracks (Fig. 2.6b for 2D).

Results

Understanding the 3D results is not too complex as it follows same tendency as 2D (see Section 2.5). For information, PCW bound is shown on the following graphs, but it is not meant to be compared with simulations results. The main observations can be listed as:

- crack-induced anisotropy, namely transverse isotropy with maximum degradation in the direction $\mathbf{n}$ normal to the crack (Fig. 4.6),
- numerical results are closer to MT in 3D (due to ellipsoidal distribution, Fig. 4.6) where in 2D results to PCW (due to spherical distribution, Fig. 2.7),
- closed crack does not contribute to the degradation of conductivity (Fig. 4.7),
- simulated results are sensitive to aspect ratio ω (Fig. 4.8),
- scalar conductivity λ^* of closed cracks affects the effective conductivity (Fig. 4.9).

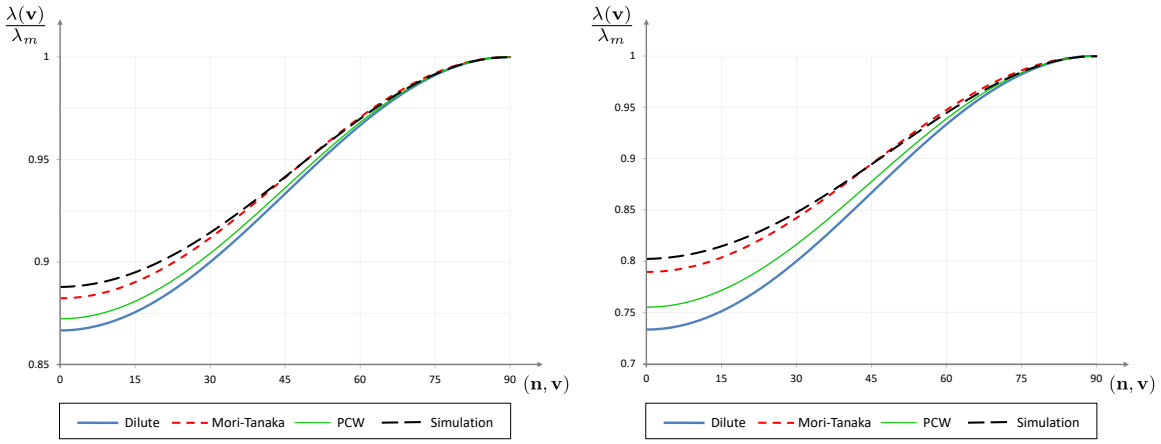

(a) $d = 0.05$ (b) $d = 0.1$

FIGURE 4.6: Generalized thermal conductivity $\lambda(\mathbf{v})$ in 3D, normalized by its initial value for a material weakened by a single array of parallel open microcracks of unit normal $\mathbf{n}$.

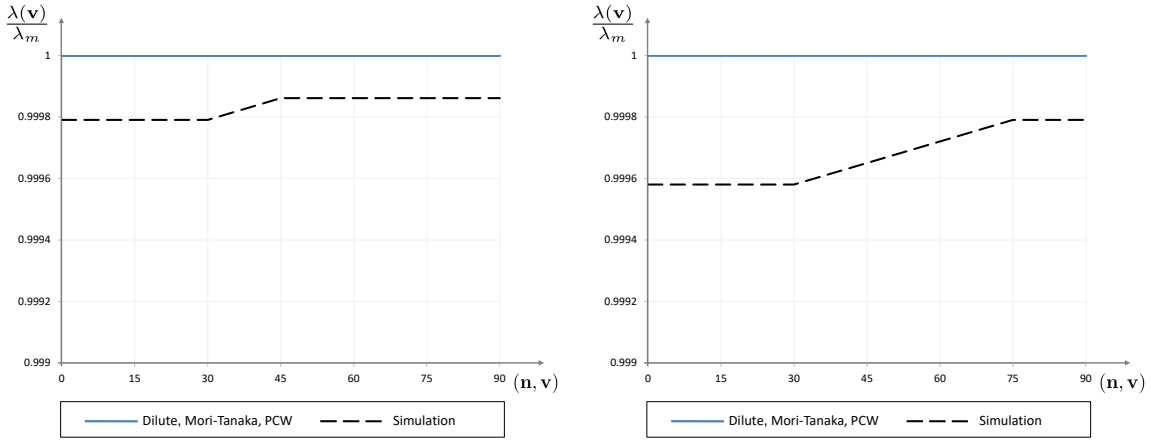

(a) $d = 0.05$ (b) $d = 0.1$

FIGURE 4.7: Generalized thermal conductivity $\lambda(\mathbf{v})$ in 3D, normalized by its initial value for a material weakened by a single array of parallel closed microcracks of unit normal $\mathbf{n}$ ($\lambda^* = 50\%\ \lambda_m$).

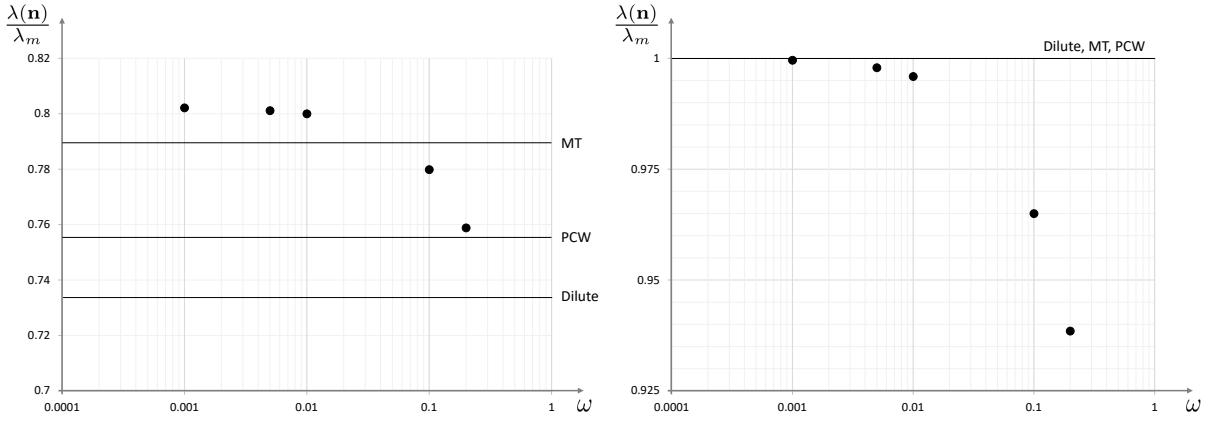

(a) Open cracks (b) Closed cracks ($\lambda^* = 50\%\ \lambda_m$)

FIGURE 4.8: Normal thermal conductivity $\lambda(\mathbf{n})$ in 3D, normalized by its initial value for various aspect ratios ($d = 0.1$); $\log_{10}$ scale is used for abscissa.

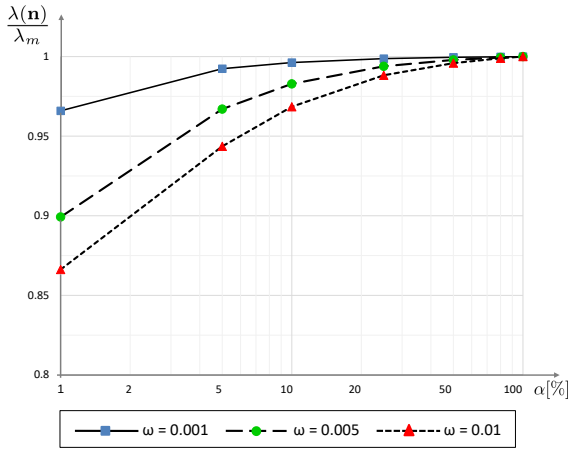

FIGURE 4.9: Influence of scalar conductivity $\lambda^* = \alpha\,\lambda_m$ on the normal thermal conductivity $\lambda(\mathbf{n})$ in 3D, normalized by its initial value ($d = 0.1$); $\log_{10}$ scale is used for abscissa.

4.4 Thermal resistivity

In this part, lets keep the properties used in the previous section, changing only the boundary condition. To be consistent with theory, uniform heat flux $Q\,(= Q_{\mathbf{v}}\,\mathbf{v})$ is imposed. This condition can be achieved by applying a heat flux density (also known as surface heat flux) $Q_{\mathbf{v}} = 14400$ W/m^2 on the top face and a temperature $T_1 = 293$ K on the bottom face. The four lateral faces of the RVE are adiabatic (Fig. 4.10). Similar to Eq. 2.13, the numerical effective resistivity in the direction $\mathbf{v}$:

$$\rho^{\text{num}}(\mathbf{v}) = \frac{G_{\mathbf{v}}}{Q_{\mathbf{v}}} \tag{4.2}$$

where $G_{\mathbf{v}}$ is the average temperature gradient along $\mathbf{v}$ direction. This temperature gradient can be given by $G_{\mathbf{v}} = \dfrac{T_2 - T_1}{L}$ in which $T_2 = \dfrac{1}{A}\displaystyle\sum_{i=1}^{N} \text{NT11}_i$, where NT11_i is the Nodal Temperature on each node i on the top face.

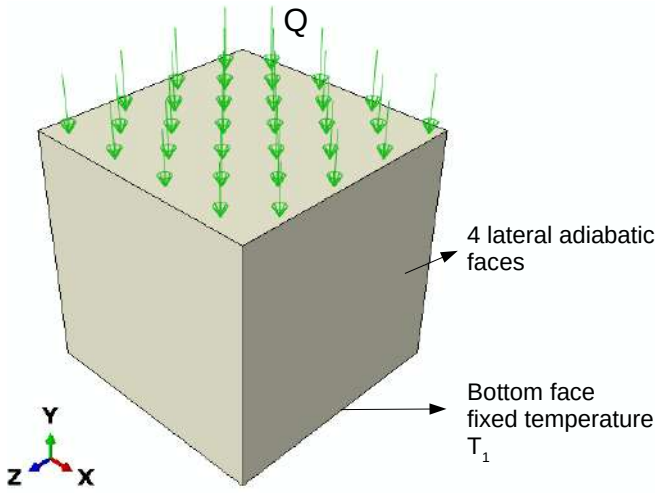

FIGURE 4.10: Simulated RVE showing the boundary condition and the prescribed load.

Results

Dilute and MT estimates in Section 1.4 are compared to numerical results here. PCW is again provided as an element of comparison for theoretical approaches. Numerical resistivity also shows crack-induced anisotropy. Just like theoretical approach, simulations show increase in resistivity as the density of cracks d increases (Fig. 4.11). From Fig. 4.12, one can see that closed cracks have only a very small influence on the resistivity (less than 0.025% for $d = 0.05$ and less than 0.045% for $d = 0.1$). Resistivity shows sensitivity to aspect ratio in both open and closed cases (Fig. 4.13). Scalar conductivity λ^* and its influence on thermal resistivity is studied for various aspect ratios. Fig. 4.14 shows this influence and also indicates that as $\omega \to 0$, closed crack property λ^* becomes irrelevant to predicting the effective resistivity. Finally, the simulated resistivity in 3D shows results close to MT. Note that, Figs. 4.13 and 4.14 only describe simulations since theoretical results do not depend on aspect ratio ω or scalar conductivity λ^*.

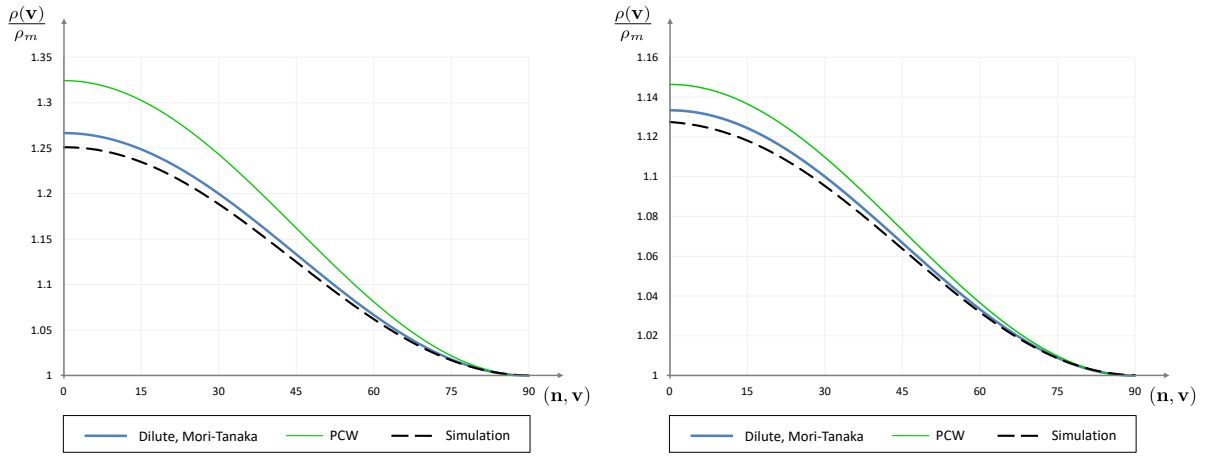

(a) $d = 0.05$ (b) $d = 0.1$

FIGURE 4.11: Generalized thermal resistivity $\rho(\mathbf{v})$ in 3D, normalized by its initial value for a material weakened by a single array of parallel open microcracks of unit normal $\mathbf{n}$.

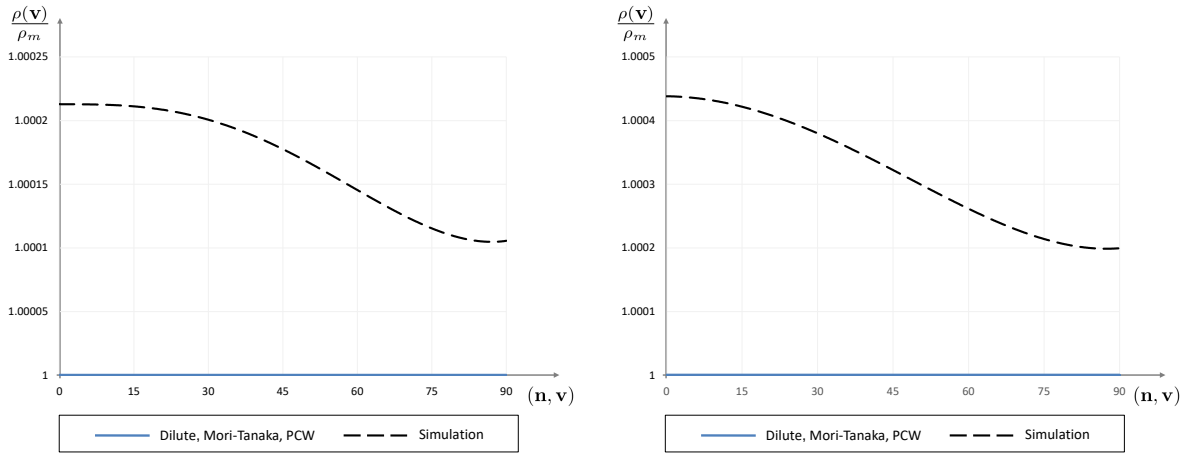

(a) $d = 0.05$ (b) $d = 0.1$

FIGURE 4.12: Generalized thermal resistivity $\rho(\mathbf{v})$ in 3D, normalized by its initial value for a material weakened by a single array of parallel closed microcracks of unit normal $\mathbf{n}$ ($\lambda^* = 50\%\ \lambda_m$).

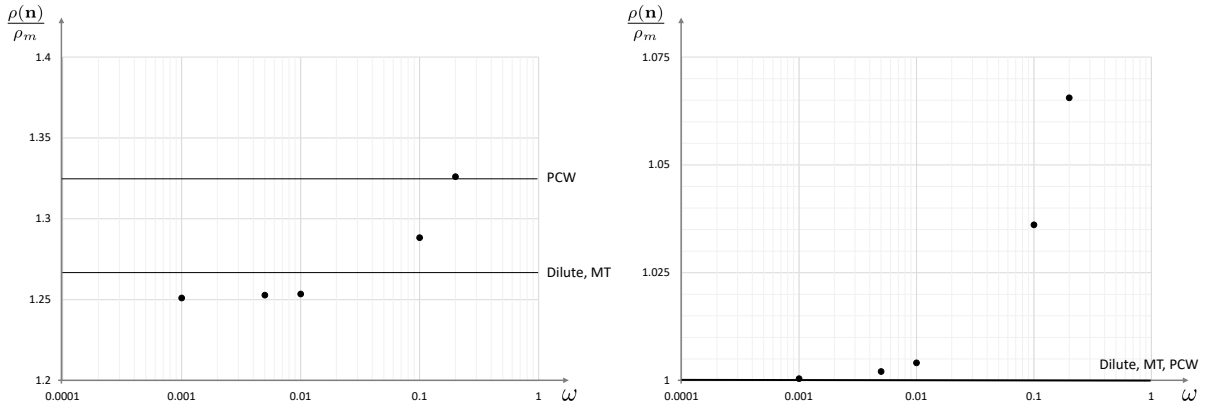

(a) Open cracks (b) Closed cracks ($\lambda^* = 50\%\ \lambda_m$)

FIGURE 4.13: Normal thermal resistivity $\rho(\mathbf{n})$ in 3D, normalized by its initial value for various aspect ratios ($d = 0.1$); $\log_{10}$ scale is used for abscissa.

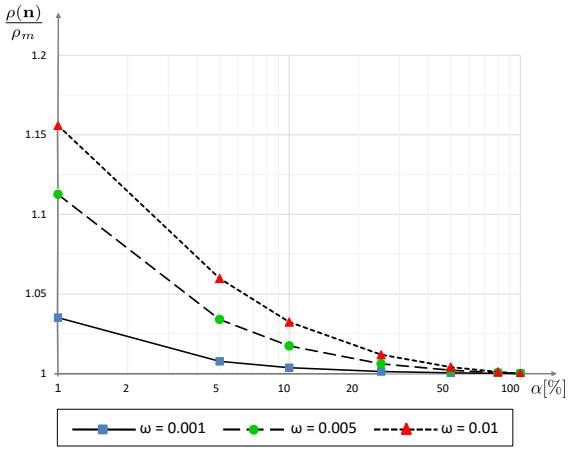

FIGURE 4.14: Influence of scalar conductivity $\lambda^* = \alpha\,\lambda_m$ on the normal thermal resistivity $\rho(\mathbf{n})$ in 3D, normalized by its initial value ($d = 0.1$); $\log_{10}$ scale is used for abscissa.

4.5 Thermoelasticity

To account for the material thermoelastic behaviour, the finite element type used for the matrix and cracks are C3D10 and C3D20R respectively. Roller boundary condition is introduced on all the RVE faces (Fig. 4.15), along with an uniform initial temperature defined all over the RVE (T_{initial}). During the calculated step, another uniform temperature load (T_{final}) is applied allowing to have $\Delta T = T_{\text{final}} - T_{\text{initial}} = 80$ K over the entire RVE. The numerical thermal stress in any direction $\mathbf{m}$ is:

$$\kappa^{\text{num}}(\mathbf{m}) = -\frac{\mathbf{m}\cdot\Sigma\cdot\mathbf{m}}{\Delta T} \tag{4.3}$$

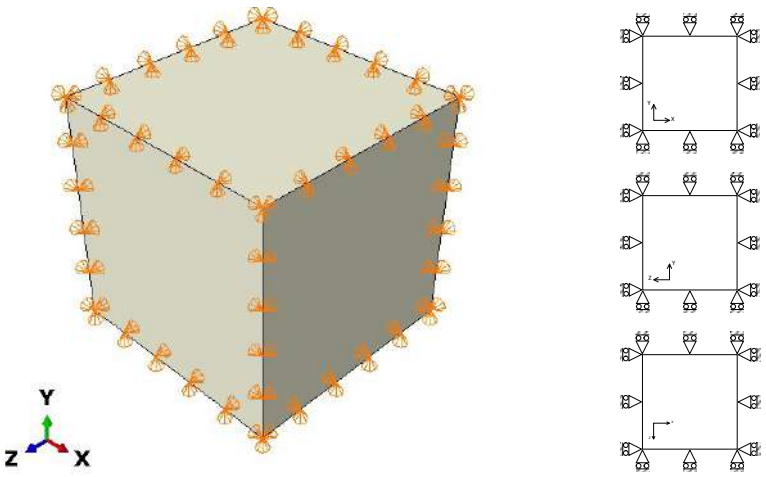

(a) (b)

FIGURE 4.15: Roller boundary condition used for the thermoelastic problem (a) ABAQUS symbols, (b) normalized scheme.

where Σ is the macroscopic stress tensor along direction $\mathbf{m}$. And the stresses in each principal axis are given by $\Sigma_{\mathbf{tt}} = \frac{1}{A}\sum_{i=1}^{N} \mathrm{RF1}_i$; $\Sigma_{\mathbf{vv}} = \frac{1}{A}\sum_{i=1}^{N} \mathrm{RF2}_i$; $\Sigma_{\mathbf{kk}} = \frac{1}{A}\sum_{i=1}^{N} \mathrm{RF3}_i$ and RF_i is the Reaction Force on each node i on the respective face.

The scalar properties of the matrix are representative of the SiC bulk cermaic, with Young's modulus $E_m = 420$ GPa, Poisson's ratio $\nu_m = 0.16$ and CTE $\alpha_m = 2.2$ ppm/K. Open cracks have zero elastic and thermal expansion properties, i.e. $E_c^{open} = 0$, $\mu_c^{open} = 0$ and $\alpha_c^{open} = 0$. For closed cracks, inclusion properties are those of a fictitious material. Similar to the theoretical work, it is assumed that the closed cracks transmit only normal stress and not shear stress. In fact, using $\mathbb{C}_c^{closed} = 3k_m\,\mathbb{J}$ for the closed cracks suggested by Deudé *et al.* (2002) cannot be implemented directly since $\mathbb{J}$ is not invertible. While encountering such difficulty, the consistency with theoretical representation can be maintained by defining engineering constants (typically used for composites) for the cracks. This allows one to define the Young's modulus E^*, Poisson's ratio ν^* and shear modulus μ^* separately, as if they are an orthotropic material with $E_{\mathbf{X}} = E_{\mathbf{Y}} = E_{\mathbf{Z}} = E^*$, $\nu_{\mathbf{X}} = \nu_{\mathbf{Y}} = \nu_{\mathbf{Z}} = \nu^*$ and $\mu_{\mathbf{X}} = \mu_{\mathbf{Y}} = \mu_{\mathbf{Z}} = \mu^*$.

Results

The first challenge of the study stands in the definition of adequate fictitious properties for closed microcracks, namely the Young's modulus E^* and Poisson's ratio ν^*, $\mu^* = 0$ being considered to cancel shear stresses. At the same time, the scalar thermal stress should be as $\kappa^* = 3\,k^*\alpha^*$ with $k^* = k_m$ (Deudé *et al.* 2002). So, to find the influence of the closed cracks on the overall thermal stress $\kappa(\mathbf{v})$, one can keep $\nu^* = \nu_m = cte$ and vary both E^* and α^*. Considering the large number of combinations to be evaluated and the resulting calculation time, the choice was made to use a method that would allow one to evaluate behavioural trends while minimizing the experiments (numerical calculations) to be done. To do this, we use the *2-level factorial design method*. This method, although practical and efficient, is based on a multilinear model of the studied system. Simulations were performed for the combinations of extreme value of E^* and α^* given in Tab. 4.1. Results of these simulations for various aspect ratios are presented in Tab. 4.2. Thus, from the 2-level factorial design method, the closed case model can be written as:

$$\frac{\kappa(\mathbf{n})}{\kappa_m} = r_0 + r_1\ E_t + r_2\ \alpha_t + r_{12}\ E_t\ \alpha_t \tag{4.4}$$

Table 4.1: Simulation problem domain

	low level: -1	**high level**: +1
Young modulus E^*	1% E_m	100% E_m
CTE: α^*	1% α_m	100% α_m

TABLE 4.2: Simulation and response matrix for factors and interactions ($\mathbf{v} = \mathbf{n}$)

Simulations No.	Avg	E_t	α_t	$E_t\alpha_t$	$\kappa(\mathbf{n})/\kappa_m$		
					$\omega = 0.001$	$\omega = 0.005$	$\omega = 0.1$
1	+1	-1	-1	+1	0.9634	0.8764	0.8232
2	+1	+1	-1	-1	0.9995	0.9978	0.9958
3	+1	-1	+1	-1	0.9637	0.8776	0.8249
4	+1	+1	+1	+1	1	1	1

TABLE 4.3: Coefficients of the factorial design method ($\mathbf{v} = \mathbf{n}$)

ω	r_0	r_1	r_2	r_{12}
0.001	0.98165	0.0181	0.0002	$5{\cdot}10^{-5}$
0.005	0.93795	0.06095	0.00085	0.00025
0.01	0.910975	0.086925	0.001475	0.000625

In Tab. 4.3, we see that $r_1 \gg r_2$, which means that the Young's modulus has much stronger influence than CTE. Since r_{12} is very small, one can say their interaction effect is negligible. Therefore, Eq. (4.4) becomes:

$$\frac{\kappa(\mathbf{n})}{\kappa_m} = r_0 + r_1\ E_t + r_2\ \alpha_t \tag{4.5}$$

with $E_t = \dfrac{E^* - 50.5\%\ E_m}{49.5\%\ E_m}$ and $\alpha_t = \dfrac{\alpha^* - 50.5\%\ \alpha_m}{49.5\%\ \alpha_m}$ provided the domain in Table 4.1 is respected, i.e. $E^* \in [1, 100]\%\ E_m$ and $\alpha^* \in [1, 100]\%\ \alpha_m$. Fig. 4.16 introduces the scalar $\eta = \dfrac{E^*}{E_m} = \dfrac{\alpha^*}{\alpha_m} = \{1...100\}$ [%], for which the influence of the aspect ratio on the overall thermal stress is presented. One can notice, as $\omega \to 0$, the influence of η becomes less consequential.

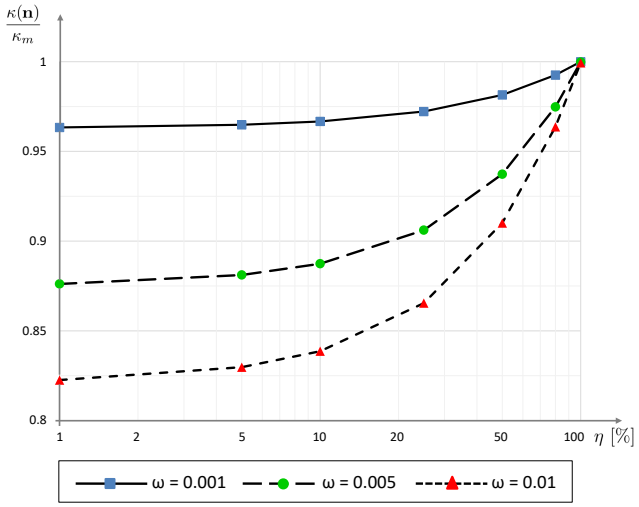

FIGURE 4.16: Influence of the ratio $\eta = {}^{E^*}/_{E_m} = {}^{\alpha^*}/_{\alpha_m}$ on the normal thermal stress $\kappa(\mathbf{n})$ normalized by its initial value ($d = 0.1$); $\log_{10}$ scale is used for abscissa.

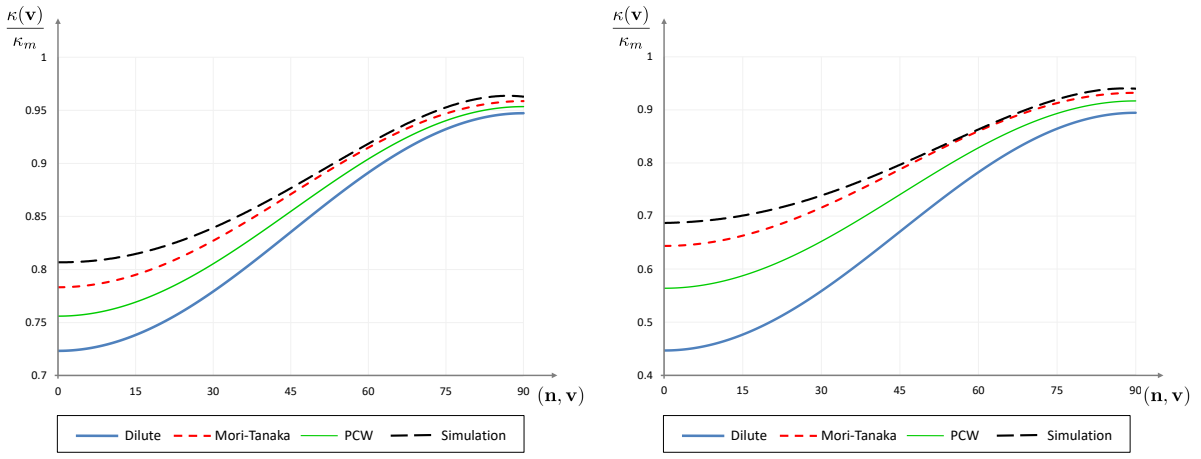

(a) $d = 0.05$ ($a = 0.171$ m) (b) $d = 0.1$ ($a = 0.215$ m)

FIGURE 4.17: Generalized thermal stress $\kappa(\mathbf{v})$ normalized by its initial value for a material weakened by a single array of parallel open microcracks of unit normal $\mathbf{n}$.

In what follows, numerical results will be compared to dilute and MT theoretical results from Chapter 3. Once again, crack-induced anisotropy can be seen here. To be precise, the thermal stress tensor is transversely isotropic around the axis $\mathbf{n}$. Unlike steady-state heat conduction problem, in thermoelasticity, cracks oriented at $(\mathbf{n}, \mathbf{v}) = 90°$ contribute to degradation of overall property (Fig. 4.17). We see that, as the cracks become smaller, their influence on the thermal stress is also reduced ($\kappa(\mathbf{n}) \approx 0.68\ \kappa_m$ for $a = 0.215$ m but $\kappa(\mathbf{n}) \approx 0.80\ \kappa_m$ for $a = 0.171$ m).

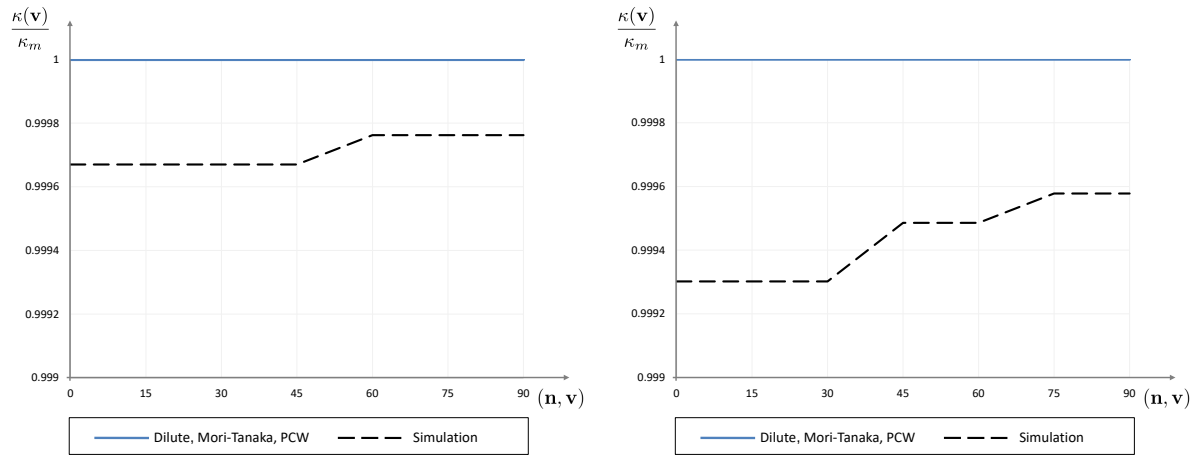

(a) $d = 0.05$ (b) $d = 0.1$

FIGURE 4.18: Generalized thermal stress $\kappa(\mathbf{v})$ normalized by its initial value for a material weakened by a single array of parallel closed microcracks of unit normal $\mathbf{n}$ ($E^* = 50\%\ E_m; \alpha^* = 50\%\ \alpha_m$).

Fig. 4.18 shows that closed cracks amount for negligible degradation of thermal stress (less than 0.04% for $d = 0.05$ and less than 0.07% for $d = 0.1$). Fig. 4.19a shows that thermal stress is not sensitive to aspect ratio of open cracks. This point will be discussed later. However, closed cracks are sensitive to aspect ratio (Fig. 4.19b). As $\omega \to 0$, the numerical result for closed case tends to theoretical result.

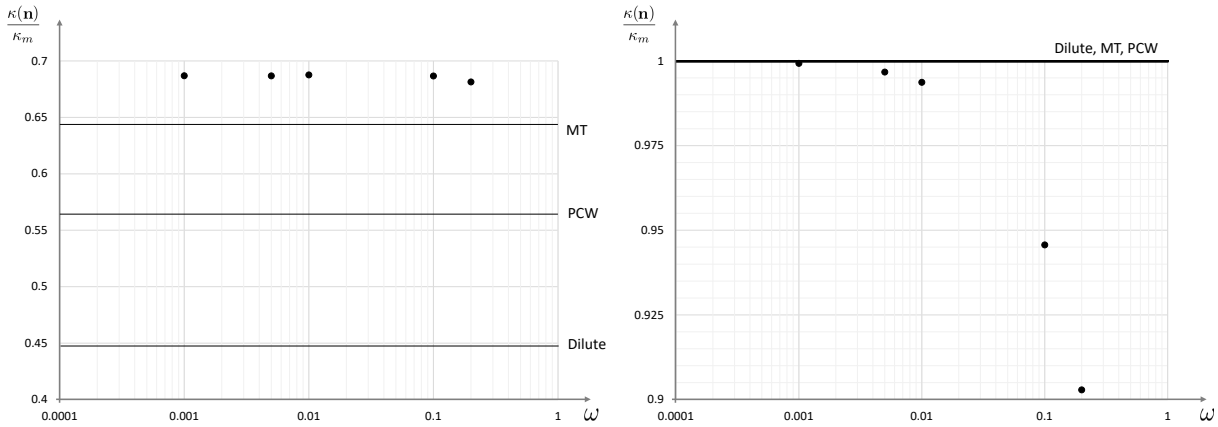

(a) Open cracks (b) Closed cracks ($E^* = 50\%\ E_m; \alpha^* = 50\%\ \alpha_m$)

FIGURE 4.19: Normal thermal stress $\kappa(\mathbf{n})$ normalized by its initial value for various aspect ratios ($d = 0.1$); $\log_{10}$ scale is used for abscissa.

4.6 Complexities and limitations

FEM may be the one of the commonly used numerical methods but as any other numerical method, it is not without limitations. For the 2D simulation of the thermal conductivity, a mesh study was done to understand its influence on the results (Tab. 2.1). 3D meshing was built using the same strategy as the 2D case. It is always the balance between accuracy and time in the FEA. One of the first challenge is to position the cracks inside the RVE. Due to their size, need for rotation and preventing edge effects, this can prove difficult. During the earlier stages of the thesis, we found that if the position of cracks is agreeable for one orientation (45° in Fig. 4.20a) then it may not be agreeable for another (0° in Fig. 4.20b). So, finding the right coordinates for the crack position is really important. Lejeunes and Bourgeois (2011) have developed a homogenization tool which allows generating an RVE with randomly distributed Voronoi cells or spherical inclusions. But this tool is for a 2D RVE since the distribution of inclusions in a 3D RVE can be complex and challenging.

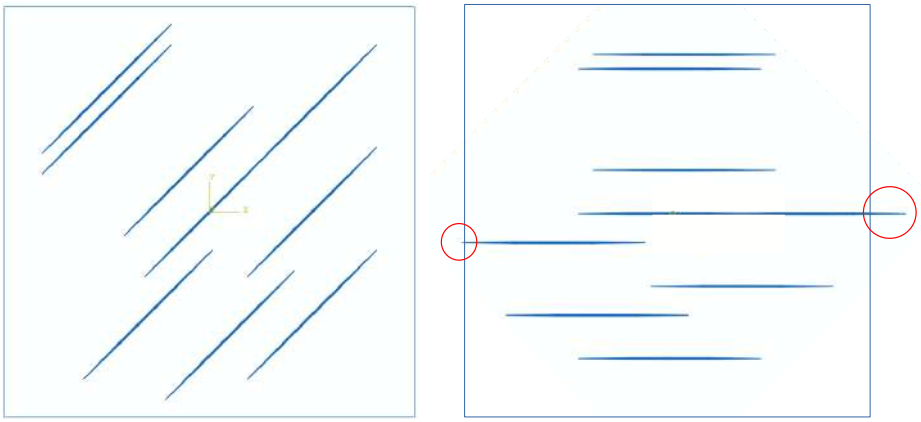

(a) $(\mathbf{v}, \mathbf{n}) = 45°$ (b) $(\mathbf{v}, \mathbf{n}) = 0°$

FIGURE 4.20: Crack position for two orientations.

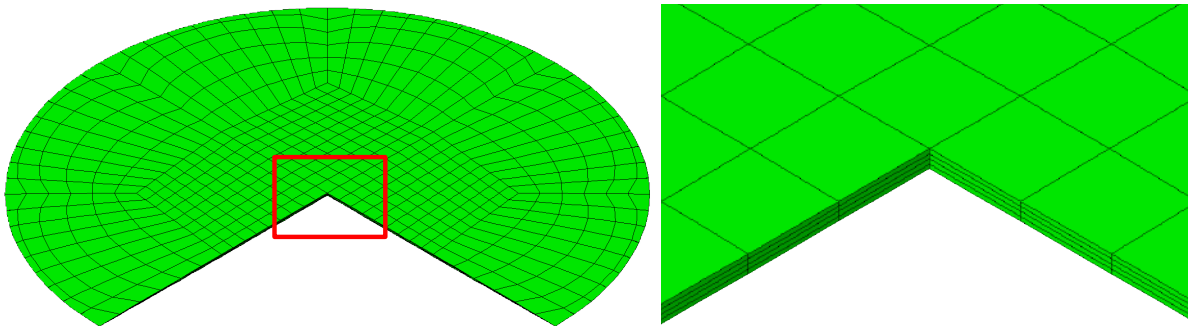

(a) Global crack mesh (b) Magnification towards the crack centre

FIGURE 4.21: Meshing of the crack showing critical area (quarter section removed) for aspect ratio $\omega = 0.005$.

This work encountered another issue when running simulations for various aspect ratio ω in open case. From Fig. 4.19a, one can see a trend that is not consistent with expected result. The figure shows that the effective property is not sensitive to aspect ratio, which can be surprising considering the previous results (Figs. 2.10, 4.8, 4.13 and 4.19b). While analyzing this point, it was discovered the issue lies with the meshing. So, a more in-depth analysis of the mesh was done to understand such result. Attempts to increase the number of elements only increase the radial and circumferential elements but not along the thickness or at the edge (crack front), which are the most critical areas (Figs. 4.21 and 4.22). In the same way, it is not possible to increase mesh density around the inclusion circumference. The heavily distorted elements at the cracks tip for small aspect ratios are not easily solved. Due to these reasons, there is no influence of the aspect ratio on the effective thermal stress in the direction $\mathbf{v}$ corresponding to the normal of the cracks even with finer meshing. Nevertheless, there is a substantial influence on the radial directions $\mathbf{t}$ and $\mathbf{k}$ (Fig. 4.23).

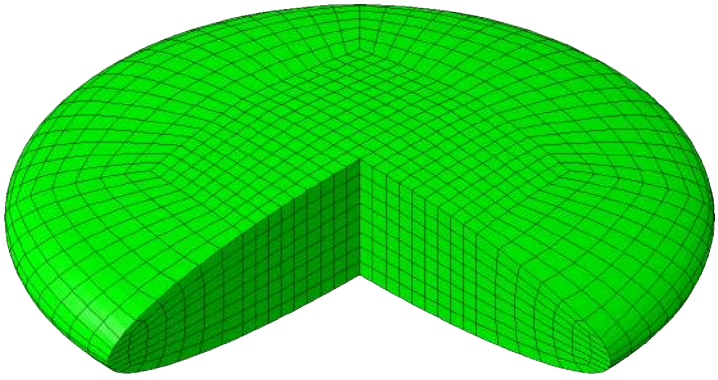

FIGURE 4.22: Meshing of the crack showing critical area (quarter section removed) for aspect ratio $\omega = 0.2$.

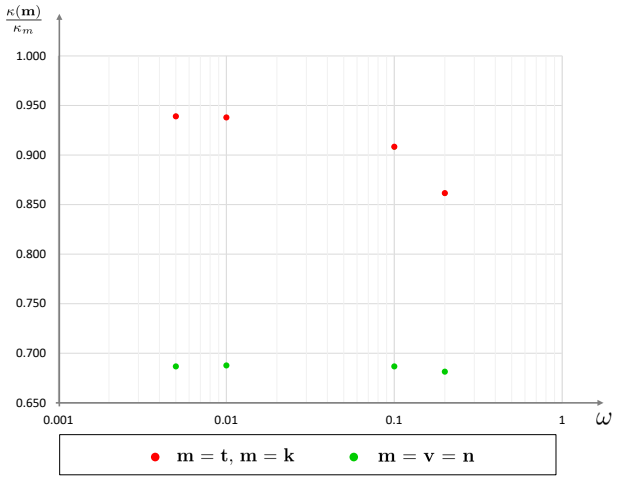

FIGURE 4.23: Normal thermal stress $\kappa(\mathbf{m})$ in any direction $\mathbf{m}$ for a single family of open cracks, normalized by its initial value for various aspect ratios ($d = 0.1$); $\log_{10}$ scale is used for abscissa.

4.7 Conclusion

This numerical part takes into account the geometry and property of the cracks same as in the theory. The consistency of theoretical and numerical results have been demonstrated through the following points. For open cracks, we observe that the microcracked RVE exhibits an induced anisotrophy with main influence of conductivity, resistivity and thermal stress on the direction normal to the crack. On the other hand, closure of cracks leads to a complete deactivation of their influence on the microcracks. We also studied the effect of aspect ratio and scalar closed crack properties on the effective properties. Finally, the limitations pertaining to using FEM is presented. In the future, further simulations can be performed by grouping the cracks closer to one another and study their interactions. This would allow to compare the different estimates, specially MT scheme and PCW bound, to the numerical modelling. Though this work studies thermal and thermoelastic concepts separately, combined thermomechanical loading and their effect of the effective properties might be interesting.

General conclusion and perspectives

The present work was indented to study the thermomechanical behaviour of the microcracked brittle materials. To this purpose, the theoretical approach is used and compared to the numerical approach.

As a first, using the existing theoretical framework for composites, the thesis gives closed-form expressions for effective thermal and thermoelastic properties for the case of microcracks. Special attention is paid to the orientation of the cracks, distribution of the cracks, unilateral effect and crack-induced anisotropy. The initially isotropic media of the RVE is considered to be weakened by randomly distributed thin oblate-ellipsoidal cracks. Open cracks are considered non-conductive and closed cracks are fictitious isotropic material to amount for some heat transfer continuity in the spirit of Deudé *et al.* (2002). Using Eshelby's *equivalent inclusion method* extended by Hatta and Taya (1986) for steady-state heat conduction, effective conductivity and resistivity are derived. The former is found using uniform gradient boundary condition and the latter using uniform flux boundary condition. Interactions between cracks are taken into account by means of Mori-Tanaka scheme and Ponte Castañeda-Willis bound. The results show that each open family of cracks acts as a thermal barrier and that the overall properties are transversely isotropic around its normal axis. So, when there are more than one family of cracks, one has a complex anisotropy which would be the summation of transverse isotropies around different crack normals. For a given family of open cracks, the maximum degradation (in conductivity) or enhancement (in resistivity) is in the direction normal to cracks. It should also be noted that different distributions of cracks (MT and PCW) lead to different expressions of thermal properties. Additionally, a family of closed cracks do not contribute to the degradation or enhancement of the conductivity or resistivity respectively, whatever the considered estimation method. All these observations were true for the analyzed 2D and 3D microcracked RVE.

Based on the same 3D microstructure, the next step is to determine the effective thermoelastic properties. The thermoelastic properties considered for homogenization are thermal strain and stress and specific heat capacities at constant strain and stress. The derivation of effective thermal stress and strain directly comes from the elastic problem, since only the knowledge of elastic strain localization and stress concentration tensors is needed. The specific heat capacity determination requires the less common thermal strain localization and stress concentration tensors. The open cracks are assumed to

have zero stiffness, zero thermal expansion and zero heat capacity whereas closed cracks are represented as before by a fictitious isotropic material to account for stress/strain continuity. Once again, expressions are given for dilute and MT schemes and PCW bound. The boundary conditions used are uniform strain with uniform temperature (to find thermal stress and specific heat at constant strain) and uniform stress with uniform temperature (to find thermal strain and specific heat at constant stress). Here also, one can observe transverse isotropy in thermal stress for a single system of open cracks with major degradation in the normal direction. As expected, different distributions of cracks give different results. Despite the conclusions of the elastic problem, closed cracks have no influence on the effective thermoelastic properties. Thermoelastic stress-based properties are not affected by cracks, either open or closed.

As mentioned many times, due to the lack of experimental data, numerical simulation was performed to get some comparison with the theoretical results. Framework similar to micromechanics was adopted for the numerical analysis in the FEA software ABAQUS. Open and closed cracks are designed as inclusion and their status is determined only based on their material property. The numerical work started with a simple 2D analysis of effective thermal conductivity, then extended to 3D to numerically find the effective thermal conductivity, resistivity and stress of the microcracked RVE. More than 150 simulations were performed to study the said properties numerically. 2D analysis considers a spherical distribution of cracks (equivalent to PCW bound) while 3D considers an elliptical distribution (equivalent to MT scheme). So, 2D results are closer to the PCW bound and 3D results are closer to MT scheme. Micromechanical results are not dependent on the aspect ratio of the cracks nor on the fictitious property of the closed cracks. The same is not true for numerical results. So, their influence was studied and presented in detail. Simulation of the steady-state conduction problem is simple but the thermoelastic problem remains much more complex (meshing issues, definition of fictitious properties of closed cracks, for instance). Using the numerical approach, this work was able to obtain tendencies consistent with the theoretical results.

Works in the thesis can be improved and present some interesting research perspectives, both on the theoretical and numerical points of view.

First, the theoretical works can be applied to other estimations techniques like self-consistent, differential, interaction direct derivative (IDD), etc. Though only linear behaviour is presented here, extension to a non-linear (viscosity, plasticity, etc.) matrix could be interesting to study damage in other types of materials. The effective thermal and thermoelastic properties provide also useful estimates for thermomechanical calculations of brittle materials. While the thesis explores fixed damage state, thermal loads applied can generate more cracks and which in turn can affect the very thermal properties studied and consequently heat transfer and thermoelastic behaviours. To that point, this work gives relevant information for further works that can be dedicated in modelling a fully coupled thermomechanical damage model with evolving damage. The framework

used can be extended to finding the effective electrical conductivity and resistivity of a microcracked media.

In the numerical works, the need for studying the interaction between cracks should be addressed. This question will face the very challenging issue of cracks location in the 3D cell. At the same time, it would be relevant to compare the inclusion-based representation used in the thesis with the representation of cracks as seams, where definition of contact can be set to evaluate closed cracks. Though the work deals with random microstructure, using X-ray tomography, real structures can be mapped and their volume reconstructed and simulations can be performed in FEA softwares. The simulations linked to this work consider thermal and thermoelastic simulations separately, but combined thermo-mechanical loading can aid in creating the damage model mentioned above. Lejeunes and Bourgeois (2011) developed a homogenization toolbox for ABAQUS to determine the homogenized elastic characteristics of heterogeneous materials. Similarly, a new graphical interface toolbox can be developed to derive the homogenized thermal characteristics as well. Since extracting results can be time consuming, toolbox powered by python script will be very attractive.

Appendices

Appendix A

Supplement to Chapter I

A.1 Equivalent inclusion method in steady-state

This part intends to present the equivalent inclusion method developed to solve the problem described at Eq. (1.12).

Consider a problem of a homogeneous medium of thermal conductivity $\boldsymbol{\lambda}_0$ in the same volume Ω, subjected to same conditions at the boundary $\partial\Omega$, and surrounded by a eigen temperature gradient g^e (or an equivalent pre-flux $q^0 = \boldsymbol{\lambda}_0 \cdot g^e$). The resulting heat flux q^*, temperature T^* and temperature gradient g^* of this fictitious problem must satisfy the following equations:

$$\begin{cases} q^*(x) & = -\boldsymbol{\lambda}_0 \cdot [g^*(x) - g^e(x)], & \forall\, x \in \Omega \\ div\ q^*(x) & = 0, & \forall\, x \in \Omega \\ g^*(x) & = grad\ T^*(x), & \forall\, x \in \Omega \\ T^*(x) & = G \cdot x, & \forall\, x \in \partial\Omega \end{cases} \tag{A.1}$$

The works of Eshelby (1957), in extension Hatta and Taya (1986), falls within the framework defined by equation set (A.1) with certain specifies: the domain Ω is considered infinite, the temperature tends to zero at infinity, the free temperature gradient g^e (or pre-flux q^0) is zero outside the inclusion domain I of Ω and uniform within the domain I (or q^0 uniform equal to $q^I = \boldsymbol{\lambda}_0 \cdot g^e$). The problem can be written as:

$$\begin{cases} q^*(x) & = -\boldsymbol{\lambda}_0 \cdot [g^*(x) - g^e(x)] = -\boldsymbol{\lambda}_0 \cdot g^*(x) + q^I, & \forall\, x \in \Omega \\ q^*(x) & = -\boldsymbol{\lambda}_0 \cdot g^*(x), & \forall\, x \in (\Omega - I) \\ div\ q^*(x) & = 0, & \forall\, x \in \Omega \\ g^*(x) & = grad\ T^*(x), & \forall\, x \in \Omega \\ T^*(x) & \to 0, & \forall\, x \to \infty \end{cases} \tag{A.2}$$

It is shown that this is equivalent to determining the temperature field equal to zero at infinity in an infinite elastic homogeneous medium subjected on an inner surface $\partial\Omega_I$ corresponding to the boundary of the inclusion to surface flux density $-q^0 \cdot \mathbf{u}$ ($\mathbf{u}$ the unit normal to $\partial\Omega_I$ directed outside I). Green's function in an infinite medium provides solution to this problem. Accordingly, when the inclusion I is ellipsoidal, the resulting temperature gradient g^I is uniform, so:

$$g^*(x) = g^I = \mathbf{S}^E \cdot g^e = \mathbf{S}^E \cdot \boldsymbol{\lambda}_0^{-1} \cdot q^I, \qquad \forall\, x \in I \tag{A.3}$$

and the resultant uniform heat flux is:

$$q^*(x) = q^I = -\boldsymbol{\lambda}_0 \cdot \left[g^I - g^e\right] = \left[\mathbf{I} - \boldsymbol{\lambda}_m \cdot \mathbf{S}^E \cdot \boldsymbol{\lambda}_0^{-1}\right] \cdot q^I, \qquad \forall\, x \in I \tag{A.4}$$

where the depolarization (Eshelby-like) tensor $\mathbf{S}^E$ depends on the shape and orientation of the inclusion.

Now consider the so-called problem of heterogeneity, were the infinite medium of volume Ω and conductivity $\boldsymbol{\lambda}_0$ is subjected to a homogeneous temperature gradient G_∞ at infinity. Additionally, a different medium of volume Ω_H and conductivity $\boldsymbol{\lambda}_H$ occupies a domain H within V with a condition of perfect interface. This problem can be defined with following set of equations:

$$\begin{cases} q^*(x) & = -\boldsymbol{\lambda}_H \cdot g^*(x), \qquad \forall\, x \in H \\ q^*(x) & = -\boldsymbol{\lambda}_0 \cdot g^*(x), \qquad \forall\, x \in (\Omega - H) \\ div\ q^*(x) & = 0, \qquad \forall\, x \in \Omega \\ g^*(x) & = grad\ T^*(x), \qquad \forall\, x \in \Omega \\ T^*(x) & \to G_\infty \cdot x, \qquad \forall\, x \to \infty \end{cases} \tag{A.5}$$

Under the condition that H is an ellipsoid and by subjecting the volume Ω including I to the same temperature gradient G_∞ at infinity as Ω including H, it can be demonstrated that there is equivalence between the inclusion problem and the heterogeneity problem if q^I is such that:

$$q^I = (\boldsymbol{\lambda}_H - \boldsymbol{\lambda}_0) \cdot (g^I + G_\infty) \tag{A.6}$$

From Eqs. (A.3) and (A.6), we get:

$$g^H = g^I + G_\infty = \left[\mathbf{I} + \mathbf{S}^E \cdot \boldsymbol{\lambda}_0^{-1} \cdot (\boldsymbol{\lambda}_H - \boldsymbol{\lambda}_0)\right]^{-1} \cdot G_\infty \tag{A.7}$$

and

$$q^H = -\boldsymbol{\lambda}_H \cdot g^H \tag{A.8}$$

In estimation methods, the solution for the heterogeneity problem is used to approximate the mean temperature gradient over the phases of the heterogeneous medium. Returning to our microcracked media problem, a cracks family is modelled as an ellipsoidal heterogeneity. Average temperature gradient $\langle g \rangle_c$ and heat flux $\langle q \rangle_c$ over the cracks phase are assimilated to the uniform fields developing in an ellipsoidal heterogeneity with same conductivity as the crack ($\boldsymbol{\lambda}_H = \boldsymbol{\lambda}_c$), with adequate shape and orientation (described through tensor $\mathbf{S}^E$) and embedded in an infinite homogeneous reference medium (of conductivity $\boldsymbol{\lambda}_0$) subjected to uniform gradient G_∞. Eq. (A.7) becomes:

$$\langle g \rangle_c = g^H = \left[\mathbf{I} + \mathbf{S}^E \cdot \boldsymbol{\lambda}_0^{-1} \cdot (\boldsymbol{\lambda}_c - \boldsymbol{\lambda}_0)\right]^{-1} \cdot G_\infty \tag{A.9}$$

For homogenization schemes considered in the study, the matrix is considered as the reference medium ($\boldsymbol{\lambda}_0 = \boldsymbol{\lambda}_m$). Moreover, for a **dilute** concentration of cracks with no interaction between cracks, the remote condition is $G_\infty = G$, therefore:

$$\langle g \rangle_c = \left[\mathbf{I} + \mathbf{S}^E \cdot \boldsymbol{\lambda}_m^{-1} \cdot (\boldsymbol{\lambda}_c - \boldsymbol{\lambda}_m)\right]^{-1} \cdot G \tag{A.10}$$

Comparing Eqs. (A.10) and (1.11), we can find the gradient localization tensor:

$$\langle \mathbf{A} \rangle_c^{dil} = \left[\mathbf{I} + \mathbf{S}^E \cdot \boldsymbol{\lambda}_m^{-1} \cdot (\boldsymbol{\lambda}_c - \boldsymbol{\lambda}_m) \right]^{-1} \tag{A.11}$$

For the **Mori – Tanka** scheme, we consider some interaction between the cracks. We retain the metholodly using in dilute case but we account the interaction between cracks by modifying the temperature gradient or flux acting on each crack. For this case, the macroscopic temperature gradient at infinity G_∞ is replaced by the phase average temperature gradient of the matrix $\langle g \rangle_m$, i.e. $G_\infty = \langle g \rangle_m$, and we know that:

$$G = \langle g \rangle = f_m \langle g \rangle_m + f_c \langle g \rangle_c \tag{A.12}$$

Based on the above mentioned assumption, one can say:

$$\langle g \rangle_c = \langle \mathbf{A} \rangle_c^{dil} \cdot \langle g \rangle_m \tag{A.13}$$

From the above two equations, G_∞ can be given in terms of G as:

$$G_\infty = \langle g \rangle_m = \left[f_m \mathbf{I} + f_c \langle \mathbf{A} \rangle_c^{dil} \right]^{-1} \cdot G \tag{A.14}$$

Substituting Eq. (A.14) in Eq. (A.13),

$$\langle g \rangle_c = \langle \mathbf{A} \rangle_c^{dil} \cdot \left[f_m \mathbf{I} + f_c \langle \mathbf{A} \rangle_c^{dil} \right]^{-1} \cdot G \tag{A.15}$$

one can compare Eqs. (A.15) and (1.11) to show that:

$$\langle \mathbf{A} \rangle_c^{MT} = \langle \mathbf{A} \rangle_c^{dil} \cdot \left[f_m \mathbf{I} + f_c \langle \mathbf{A} \rangle_c^{dil} \right]^{-1} \tag{A.16}$$

As we see from Eqs. (A.11) and (A.16), the estimation are function of

- volume fractions,
- matrix and crack properties,
- shape of the crack (through Eshelby-like tensor).

Since the above points are already known, it is fairly easy to estimate the effective properties by combining Eq. (A.11) or (A.16) into Eq. (1.10).

Apart from these two methods, Ponte Castañeda and Willis introduced an energy based bound which help us find the effective properties directly. They employ an additional tensor which takes into account the spatial distribution of the inclusions (or cracks). From this method, both dilute and Mori-Tanaka results can be achieved by considering different spatial distribution tensor. This makes them a special case of PCW.

Using the same methodology used for the conductivity problem, we can also find the effective resistivity. Here instead of considering a uniform temperature gradient G boundary condition, we will consider a uniform heat flux Q. Accordingly,

$$\boldsymbol{\rho}_{hom} = \boldsymbol{\rho}_m + f_c \left(\boldsymbol{\rho}_c - \boldsymbol{\rho}_m \right) \cdot \langle \mathbf{B} \rangle_i \tag{A.17}$$

where $\mathbf{B}$ is the second-order flux concentration tensor. And it links the microscopic and macroscopic heat flux of each phase linearly:

$$\langle q \rangle_r = \langle \mathbf{B} \rangle_r \cdot Q \tag{A.18}$$

For the crack phase, from Eqs. (1.3), (1.5), (1.6) and (A.18), and for **dilute** case ($f_c \ll 1$), $\langle \boldsymbol{\lambda} \cdot \mathbf{A} \rangle^{-1} \approx \boldsymbol{\lambda}_m^{-1} = \boldsymbol{\rho}_m$, the flux concentration tensor becomes:

$$\mathbf{B}_c^{dil} = \boldsymbol{\lambda}_c \cdot \mathbf{A}_c^{dil} \cdot \langle \boldsymbol{\lambda} \cdot \mathbf{A} \rangle^{-1} = \boldsymbol{\lambda}_c \cdot \mathbf{A}_c^{dil} \cdot \boldsymbol{\rho}_m \tag{A.19}$$

Similar to Eq. (A.16) with the remote condition $Q_\infty = \langle q \rangle_m$, the flux concentration tensor in **Mori – Tanaka** can be given by:

$$\langle \mathbf{B} \rangle_c^{MT} = \langle \mathbf{B} \rangle_c^{dil} \cdot \left[f_m \mathbf{I} + f_c \langle \mathbf{B} \rangle_c^{dil} \right]^{-1} \tag{A.20}$$

Many such schemes can be used to find the flux concentration and gradient localization tensors, each with their own assumptions, advantages and shortcomings.

A.2 Volume fraction of cracks

When a cracks family is modeled as a penny-shaped ellipsoid (Fig. 1.1b), volume fraction of $\mathcal{N}$ number of cracks per unit volume is defined by:

$$f_c = \mathcal{N} * \frac{4}{3}\pi a^2 c = \frac{4}{3}\pi a^3 \left(\frac{c}{a}\right) \mathcal{N} = \frac{4}{3}\pi d\omega \tag{A.21}$$

where (a, c) are the mean semi-axes of the cracks, $\omega = {}^{c}/_{a}$ the mean aspect ratio and $d = \mathcal{N} a^3$ the crack density.

A.3 Depolarization tensor

The components of the depolarization tensor in 3D can be given by (Hatta and Taya 1986):

$$S_{ii} = \frac{a_1 a_2 a_3}{2} \int_0^\infty \frac{ds}{(a_i^2 + s)\sqrt{(a_1^2 + s)(a_2^2 + s)(a_3^2 + s)}} \quad (i = 1...3) \tag{A.22}$$

and $S_{ij} = 0$ for $i \neq j$. Eq. (A.22) is an elliptical integral but can be expressed for a simple geometries of ellipsoids. Typically, for an ellipsoid such that $a_1 = a_2 = a$ and $a_3 = c$, Therefore Eq. (A.22) becomes:

$$S_{11} = S_{22} = \frac{a^2 c}{2} \int_0^\infty \frac{ds}{(a^2 + s)^2 \sqrt{(c^2 + s)}} \tag{A.23}$$

$$S_{33} = \frac{a^2 c}{2} \int_0^\infty \frac{ds}{(c^2 + s)(a^2 + s)\sqrt{(c^2 + s)}} \tag{A.24}$$

Solving Eqs. (A.23) and (A.24), and considering the special case of penny-shape, i.e. $a \gg c$, one has:

$$S_{11} = S_{22} = \frac{\pi}{4}\omega \qquad S_{33} = 1 - \frac{\pi}{2}\omega \tag{A.25}$$

For an orthogonal base $(\mathbf{k}, \mathbf{t}, \mathbf{n})$, the tensorial form of Eq. (A.25) can be written as

$$\mathbf{S}_E = S_{11}\ \mathbf{k} \otimes \mathbf{k} + S_{22}\ \mathbf{t} \otimes \mathbf{t} + S_{33}\ \mathbf{n} \otimes \mathbf{n} = S_{11}\ (\mathbf{k} \otimes \mathbf{k} + \mathbf{t} \otimes \mathbf{t}) + S_{33}\ \mathbf{n} \otimes \mathbf{n} \tag{A.26}$$

Knowing that, $\mathbf{I} = \mathbf{k}\otimes\mathbf{k} + \mathbf{t}\otimes\mathbf{t} + \mathbf{n}\otimes\mathbf{n}$, it can be simplified as:

$$\mathbf{S}_E = S_{11}\ (\mathbf{I} - \mathbf{n}\otimes\mathbf{n}) + S_{33}\ \mathbf{n}\otimes\mathbf{n} = \frac{\pi}{4}\,\omega\ (\mathbf{I} - \mathbf{n}\otimes\mathbf{n}) + \left(1 - \frac{\pi}{2}\,\omega\right)\mathbf{n}\otimes\mathbf{n} \tag{A.27}$$

A.4 Tensorial inverse

Let the second order tensor $\mathbf{A} = w\ (\mathbf{I} - \mathbf{n}\otimes\mathbf{n}) + z\ \mathbf{n}\otimes\mathbf{n}$, where w and z are scalars such that $w \neq 0$ and $z \neq 0$. Now its inverse can given be as $\mathbf{A}^{-1} = \dfrac{1}{w}\ (\mathbf{I} - \mathbf{n}\otimes\mathbf{n}) + \dfrac{1}{z}\ \mathbf{n}\otimes\mathbf{n}$.

A.5 Detailed calculation of conductivity

For simplicity, the mathematical demonstration is detailed here for a single family of crack. It can be extended to several families as provided in Chapter 1.

Lets recall the expression to find the effective conductivity from Eq. (1.10):

$$\boldsymbol{\lambda}_{hom} = \boldsymbol{\lambda}_m + f_c\ (\boldsymbol{\lambda}_c - \boldsymbol{\lambda}_m)\cdot\langle\mathbf{A}\rangle_c \tag{A.28}$$

since we already know $\boldsymbol{\lambda}_m = \lambda_m\ \mathbf{I}$ and $\boldsymbol{\lambda}_c = \lambda_c\ \mathbf{I}$, the equation above can rewritten as

$$\boldsymbol{\lambda}_{hom} = \boldsymbol{\lambda}_m + \lambda_m\ f_c\ \left(\frac{\lambda_c}{\lambda_m} - 1\right)\langle\mathbf{A}\rangle_c = \lambda_m\Big[\mathbf{I} - f_c\,(1-\xi)\,\langle\mathbf{A}\rangle_c\Big] \quad \text{with} \quad \xi = \frac{\lambda_c}{\lambda_m} \tag{A.29}$$

A.5.1 Dilute scheme

The gradient localization tensor for dilute case given by Eq. (A.11):

$$\langle\mathbf{A}\rangle_c^{dil} = \Big[\mathbf{I} + \mathbf{S}_E\cdot\boldsymbol{\lambda}_m^{-1}\cdot(\boldsymbol{\lambda}_c - \boldsymbol{\lambda}_m)\Big]^{-1} \tag{A.30}$$

$$\langle\mathbf{A}\rangle_c^{dil} = \left[\mathbf{I} + \left(\frac{\lambda_c}{\lambda_m} - 1\right)\mathbf{S}_E\right]^{-1} = \Big[\mathbf{I} - (1-\xi)\,\mathbf{S}_E\Big]^{-1} \tag{A.31}$$

Substituting Eq. (A.27) in Eq. (A.31) one gets:

$$\langle\mathbf{A}\rangle_c^{dil} = \Big[\mathbf{I} - \mathbf{n}\otimes\mathbf{n} + \mathbf{n}\otimes\mathbf{n} - \left(\frac{\pi}{4}\,\omega\ (\mathbf{I} - \mathbf{n}\otimes\mathbf{n}) + \left(1 - \frac{\pi}{2}\,\omega\right)\ \mathbf{n}\otimes\mathbf{n}\right)(1-\xi)\Big]^{-1} \tag{A.32}$$

$$\langle\mathbf{A}\rangle_c^{dil} = \left[\left(1 - \frac{\pi}{4}\,\omega\ (1-\xi)\right)(\mathbf{I} - \mathbf{n}\otimes\mathbf{n}) + \left[1 - \left(1 - \frac{\pi}{2}\,\omega\right)(1-\xi)\right]\mathbf{n}\otimes\mathbf{n}\right]^{-1} \tag{A.33}$$

Using the tensorial inverse in Section A.4, Eq. (A.33) comes to:

$$\langle\mathbf{A}\rangle_c^{dil} = \frac{1}{1 - \dfrac{\pi}{4}\,\omega\ (1-\xi)}\ (\mathbf{I} - \mathbf{n}\otimes\mathbf{n}) + \frac{1}{1 - \left(1 - \dfrac{\pi}{2}\,\omega\right)(1-\xi)}\ \mathbf{n}\otimes\mathbf{n} \tag{A.34}$$

Further simplifying effective conductivity Eq. (A.29) can be:

$$\boldsymbol{\lambda}_{hom}^{dil} = \lambda_m \left[\mathbf{I} - \frac{4}{3}\pi d\omega\,(1-\xi)\,\langle\mathbf{A}\rangle_c^{dil}\right] = \lambda_m \left[\mathbf{I} - \frac{4}{3}\pi d\,\mathbf{T}\right]$$
$$\text{with} \quad \mathbf{T} = \lim_{\omega\to 0} \omega\,(1-\xi)\,\langle\mathbf{A}\rangle_c^{dil} \tag{A.35}$$

$$\mathbf{T} = \lim_{\omega\to 0} \frac{\omega(1-\xi)}{1-\frac{\pi}{4}\,\omega\,(1-\xi)}\,(\mathbf{I}-\mathbf{n}\otimes\mathbf{n}) + \frac{\omega(1-\xi)}{1-\left(1-\frac{\pi}{2}\,\omega\right)(1-\xi)}\,\mathbf{n}\otimes\mathbf{n} \tag{A.36}$$

For open case $\lambda_c = 0$ therefore $\xi = 0$, so:

$$\mathbf{T} = \lim_{\omega\to 0} \frac{4\omega}{4-\pi\omega}\,(\mathbf{I}-\mathbf{n}\otimes\mathbf{n}) + \frac{2}{\pi}\,\mathbf{n}\otimes\mathbf{n} = \frac{2}{\pi}\,\mathbf{n}\otimes\mathbf{n} \tag{A.37}$$

For closed case $\lambda_c \neq 0$ therefore for all $\xi \neq 0$:

$$\mathbf{T} = \lim_{\omega\to 0} \frac{\omega(1-\xi)}{1-\frac{\pi}{4}\,\omega\,(1-\xi)}\,(\mathbf{I}-\mathbf{n}\otimes\mathbf{n}) + \frac{\omega(1-\xi)}{\xi+\frac{\pi}{2}\,\omega(1-\xi)}\,\mathbf{n}\otimes\mathbf{n} = \mathbf{0} \tag{A.38}$$

A.5.2 Mori-Tanaka scheme

The gradient localization tensor for Mori-Tanaka is presented in Eq. (A.16):

$$\langle\mathbf{A}\rangle_c^{MT} = \langle\mathbf{A}\rangle_c^{dil} \cdot \left[f_m\,\mathbf{I} + f_c\,\langle\mathbf{A}\rangle_c^{dil}\right]^{-1} \tag{A.39}$$

Therefore, Eq. (A.29) takes the form:

$$\boldsymbol{\lambda}_{hom}^{MT} = \lambda_m \left[\mathbf{I} - f_c\,(1-\xi)\,\langle\mathbf{A}\rangle_c^{dil} \cdot \left[f_m\,\mathbf{I} + f_c\,\langle\mathbf{A}\rangle_c^{dil}\right]^{-1}\right] \tag{A.40}$$

Lets call $\left[f_m\,\mathbf{I} + f_c\,\langle\mathbf{A}\rangle_c^{dil}\right]^{-1} = \mathbf{G}$, so:

$$\boldsymbol{\lambda}_{hom}^{MT} = \lambda_m \left[\mathbf{G}^{-1} - f_c\,(1-\xi)\,\langle\mathbf{A}\rangle_c^{dil}\right] \cdot \mathbf{G} = \lambda_m \left[f_m\,\mathbf{I} + \xi f_c \langle\mathbf{A}\rangle_c^{dil}\right] \cdot \mathbf{G} = \lambda_m\,\mathbf{X}\cdot\mathbf{G} \tag{A.41}$$

Considering thin inclusion ($\omega \to 0$), $f_m = 1 - f_c \to 1$. Moreover, since $\xi = 0$ in the open case and $\omega\langle\mathbf{A}\rangle_c^{dil} = 0$ in the closed case, we thus have $\mathbf{X} = \mathbf{I}$ and $\boldsymbol{\lambda}_{hom} = \lambda_m\,\mathbf{G}$, so:

$$\boldsymbol{\lambda}_{hom}^{MT} = \lambda_m \left[\mathbf{I} + \frac{4}{3}\pi d\omega\,\langle\mathbf{A}\rangle_c^{dil}\right]^{-1} = \lambda_m \left[\mathbf{I} + \frac{4}{3}\pi d\,\mathbf{T}\right]^{-1} \tag{A.42}$$

A.5.3 Ponte Castañeda-Willis bound

The gradient localization tensor for PCW is given in Eq. (1.29)

$$\begin{aligned}\langle \mathbf{A} \rangle_c^{PCW} &= \langle \mathbf{A} \rangle_c^{dil} \cdot \left(f_m \, \mathbf{I} + f_c \Big[\mathbf{I} + \big(\mathbf{P}_E - \mathbf{P}_d \big) \cdot \big(\boldsymbol{\lambda}_c - \boldsymbol{\lambda}_m \big) \Big] \cdot \langle \mathbf{A} \rangle_c^{dil} \right)^{-1} \\ &= \langle \mathbf{A} \rangle_c^{dil} \cdot \left(f_m \, \mathbf{I} + f_c \Big[\mathbf{I} + \big(\mathbf{S}_E - \mathbf{S}_d \big) \big(1 - \xi \big) \Big] \cdot \langle \mathbf{A} \rangle_c^{dil} \right)^{-1} \\ &= \langle \mathbf{A} \rangle_c^{dil} \cdot \left(f_m \, \mathbf{I} + f_c \left(1 - \xi \right) \mathbf{S}_d \cdot \langle \mathbf{A} \rangle_c^{dil} \right)^{-1}\end{aligned}$$

At the limit $\omega \to 0$ and for a spherical spatial distribution $\mathbf{S}_d = \dfrac{1}{3}\mathbf{I}$, one has:

$$\langle \mathbf{A} \rangle_c^{PCW} = \langle \mathbf{A} \rangle_c^{dil} \cdot \left(\mathbf{I} + \frac{4}{9} \pi d \, \mathbf{T} \right)^{-1} \tag{A.43}$$

A.6 Detailed calculation of resistivity

The effective resistivity is given in Eq. (A.17).

A.6.1 Dilute scheme

The flux concentration tensor is given in Eq. (A.19):

$$\mathbf{B}_c^{dil} = \boldsymbol{\lambda}_c \cdot \mathbf{A}_c^{dil} \cdot \boldsymbol{\rho}_m = \boldsymbol{\lambda}_c \cdot \Big[\mathbf{I} + \mathbf{S}_E \cdot \boldsymbol{\lambda}_m^{-1} \cdot \left(\boldsymbol{\lambda}_c - \boldsymbol{\lambda}_m \right) \Big]^{-1} \cdot \boldsymbol{\rho}_m \tag{A.44}$$

$$\mathbf{B}_c^{dil} = \Big[\boldsymbol{\lambda}_m \cdot \boldsymbol{\rho}_c + \boldsymbol{\lambda}_m \cdot \mathbf{S}_E \cdot \boldsymbol{\lambda}_m^{-1} \cdot \left(\boldsymbol{\lambda}_c - \boldsymbol{\lambda}_m \right) \cdot \boldsymbol{\rho}_c \Big]^{-1} \tag{A.45}$$

Lets call $\mathbf{S}_E \cdot \boldsymbol{\lambda}_m^{-1} = \mathbf{P}_E$, which is similar to the Hill first tensor in elasticity, so:

$$\begin{aligned}\mathbf{B}_c^{dil} &= \Big[\boldsymbol{\lambda}_m \cdot \boldsymbol{\rho}_c + \boldsymbol{\lambda}_m \cdot \mathbf{P}_E \cdot \boldsymbol{\lambda}_c \cdot \boldsymbol{\rho}_c - \boldsymbol{\lambda}_m \cdot \mathbf{P}_E \cdot \boldsymbol{\lambda}_m \cdot \boldsymbol{\rho}_c \Big]^{-1} \\ &= \Big[\boldsymbol{\lambda}_m \cdot \boldsymbol{\rho}_c + \boldsymbol{\lambda}_m \cdot \mathbf{P}_E \cdot \mathbf{I} - \boldsymbol{\lambda}_m \cdot \mathbf{P}_E \cdot \boldsymbol{\lambda}_m \cdot \boldsymbol{\rho}_c \Big]^{-1} \\ &= \Big[\mathbf{I} + \boldsymbol{\lambda}_m \cdot \boldsymbol{\rho}_c - \mathbf{I} + \boldsymbol{\lambda}_m \cdot \mathbf{P}_E \cdot \mathbf{I} - \boldsymbol{\lambda}_m \cdot \mathbf{P}_E \cdot \boldsymbol{\lambda}_m \cdot \boldsymbol{\rho}_c \Big]^{-1} \\ &= \Big[\mathbf{I} + \boldsymbol{\lambda}_m \cdot \boldsymbol{\rho}_c - \boldsymbol{\lambda}_m \cdot \boldsymbol{\rho}_m + \boldsymbol{\lambda}_m \cdot \mathbf{P}_E \cdot \boldsymbol{\lambda}_m \cdot \boldsymbol{\rho}_m - \boldsymbol{\lambda}_m \cdot \mathbf{P}_E \cdot \boldsymbol{\lambda}_m \cdot \boldsymbol{\rho}_c \Big]^{-1} \\ &= \Big[\mathbf{I} + \boldsymbol{\lambda}_m \cdot \left(\boldsymbol{\rho}_c - \boldsymbol{\rho}_m \right) - \boldsymbol{\lambda}_m \cdot \mathbf{P}_E \cdot \boldsymbol{\lambda}_m \cdot \left(\boldsymbol{\rho}_c - \boldsymbol{\rho}_m \right) \Big]^{-1} \\ &= \Big[\mathbf{I} + \left(\boldsymbol{\lambda}_m - \boldsymbol{\lambda}_m \cdot \mathbf{P}_E \cdot \boldsymbol{\lambda}_m \right) \cdot \left(\boldsymbol{\rho}_c - \boldsymbol{\rho}_m \right) \Big]^{-1}\end{aligned}$$

Therefore:

$$\mathbf{B}_c^{dil} = \Big[\mathbf{I} + \mathbf{Q}_E \cdot \left(\boldsymbol{\rho}_c - \boldsymbol{\rho}_m \right) \Big]^{-1} \tag{A.46}$$

where $\mathbf{Q}_E = \boldsymbol{\lambda}_m - \boldsymbol{\lambda}_m \cdot \mathbf{P}_E \cdot \boldsymbol{\lambda}_m$ is similar to the Hill second tensor of elasticity. Now, substituting Eq. (A.46) into Eq. (A.17):

$$\begin{aligned}
\boldsymbol{\rho}_{hom}^{dil} &= \boldsymbol{\rho}_m + f_c \left[(\boldsymbol{\rho}_c - \boldsymbol{\rho}_m)^{-1} + \mathbf{Q}_E \right]^{-1} = \boldsymbol{\rho}_m + f_c \left[\left(\frac{\xi}{1-\xi} \right) \boldsymbol{\rho}_m^{-1} + \mathbf{Q}_E \right]^{-1} \\
&= \boldsymbol{\rho}_m + f_c \left[\left(\frac{\xi}{1-\xi} \right) \mathbf{I} + \mathbf{I} - \mathbf{S}_E \right]^{-1} \cdot \boldsymbol{\rho}_m \\
&= \boldsymbol{\rho}_m + f_c \, (1-\xi) \left[\mathbf{I} - (1-\xi) \mathbf{S}_E \right]^{-1} \cdot \boldsymbol{\rho}_m = \rho_m \left[\mathbf{I} + \frac{4}{3} \pi d\omega \, (1-\xi) \, \langle \mathbf{A} \rangle_c^{dil} \right]
\end{aligned}$$

This leads to:

$$\boldsymbol{\rho}_{hom}^{dil} = \rho_m \left[\mathbf{I} + \frac{4}{3} \pi d \, \mathbf{T} \right] \tag{A.47}$$

A.6.2 Mori-Tanaka scheme

For the MT model, the flux concentration tensor reads:

$$\langle \mathbf{B} \rangle_c^{MT} = \langle \mathbf{B} \rangle_c^{dil} \cdot \left[f_m \, \mathbf{I} + f_c \, \langle \mathbf{B} \rangle_c^{dil} \right]^{-1} \tag{A.48}$$

Accordindgly,

$$\begin{aligned}
\langle \mathbf{B} \rangle_c^{MT} &= \left[(1-f_c) \left(\langle \mathbf{B} \rangle_c^{dil} \right)^{-1} + f_c \, \mathbf{I} \right]^{-1} \\
&= \left[(1-f_c) \left[\mathbf{I} + \mathbf{Q}_E \cdot (\boldsymbol{\rho}_c - \boldsymbol{\rho}_m) \right] + f_c \, \mathbf{I} \right]^{-1} \\
&= \left[\mathbf{I} + (1-f_c) \, \mathbf{Q}_E \cdot (\boldsymbol{\rho}_c - \boldsymbol{\rho}_m) \right]^{-1}
\end{aligned}$$

From Eq. (A.17), and using similar simplifications as for the dilute case, the effective resistivity writes:

$$\boldsymbol{\rho}_{hom}^{MT} = \boldsymbol{\rho}_m + f_c \, (1-\xi) \left[\xi \mathbf{I} + (1-\xi)(1-f_c) \mathbf{I} - (1-f_c)^2 (1-\xi) \mathbf{S}_E \right]^{-1} \cdot \boldsymbol{\rho}_m \tag{A.49}$$

At the limit case ($\omega \to 0$), it comes thus :

$$\boldsymbol{\rho}_{hom}^{MT} = \boldsymbol{\rho}_{hom}^{dil} \tag{A.50}$$

A.6.3 Ponte Castañeda-Willis bound

The flux concentration tensor for PCW is presented in Eq. (3.61):

$$\begin{aligned}
\langle \mathbf{B} \rangle_c^{PCW} &= \langle \mathbf{B} \rangle_c^{dil} \cdot \left(f_m \, \mathbf{I} + f_c \Big[\mathbf{I} + \big(\mathbf{Q}_E - \mathbf{Q}_d \big) \cdot \big(\boldsymbol{\rho}_c - \boldsymbol{\rho}_m \big) \Big] \cdot \langle \mathbf{B} \rangle_c^{dil} \right)^{-1} \\
&= \langle \mathbf{B} \rangle_c^{dil} \cdot \left(f_m \, \mathbf{I} + f_c \Big[\mathbf{I} + \mathbf{Q}_E \cdot \big(\boldsymbol{\rho}_c - \boldsymbol{\rho}_m \big) - \mathbf{Q}_d \cdot \big(\boldsymbol{\rho}_c - \boldsymbol{\rho}_m \big) \Big] \cdot \langle \mathbf{B} \rangle_c^{dil} \right)^{-1} \\
&= \langle \mathbf{B} \rangle_c^{dil} \cdot \left(\mathbf{I} - f_c \, \mathbf{Q}_d \cdot \big(\boldsymbol{\rho}_c - \boldsymbol{\rho}_m \big) \cdot \langle \mathbf{B} \rangle_c^{dil} \right)^{-1} \\
&= \langle \mathbf{B} \rangle_c^{dil} \cdot \left(\mathbf{I} - f_c \, (1-\xi) \, \mathbf{Q}_d \cdot \boldsymbol{\rho}_m \cdot \left[\mathbf{I} - \mathbf{S}_E \, (1-\xi) \right]^{-1} \right)^{-1}
\end{aligned}$$

We already established $\mathbf{Q}_d = \boldsymbol{\lambda}_m - \boldsymbol{\lambda}_m \cdot \mathbf{P}_d \cdot \boldsymbol{\lambda}_m = \boldsymbol{\lambda}_m \cdot (\mathbf{I} - \mathbf{S}_d) = \dfrac{2}{3}\boldsymbol{\lambda}_m$, so:

$$\langle \mathbf{B} \rangle_c^{PCW} \quad = \quad \langle \mathbf{B} \rangle_c^{dil} \cdot \left(\mathbf{I} - \frac{8}{9}\pi d\omega \ (1-\xi) \ \langle \mathbf{A} \rangle_c^{dil} \right)^{-1}$$

The concentration tensor finally reads:

$$\langle \mathbf{B} \rangle_c^{PCW} = \langle \mathbf{B} \rangle_c^{dil} \cdot \left(\mathbf{I} - \frac{8}{9}\pi d\, \mathbf{T} \right)^{-1} \tag{A.51}$$

A.7 Scheme equivalence

According to these results, some equivalence between estimates of the overall thermal properties can be highlighted (Fig. A.1).

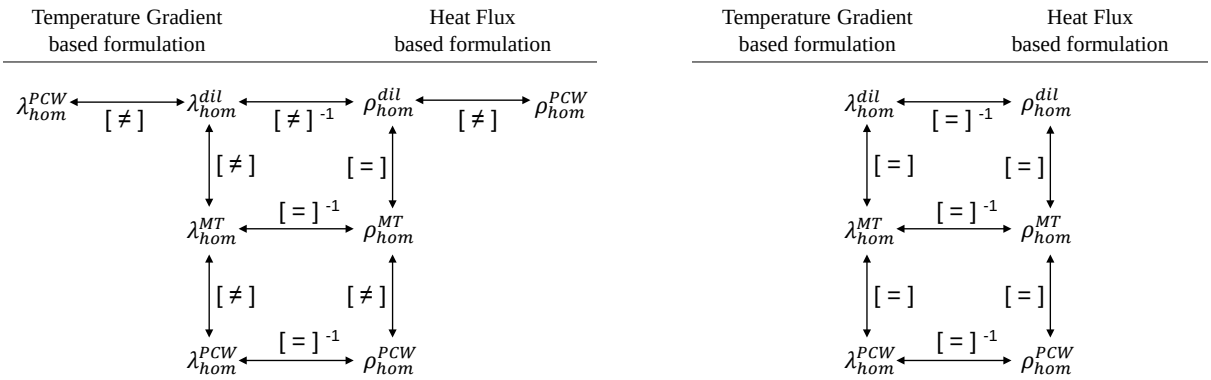

(a) Open cracks (b) Closed cracks

Figure A.1: Equivalence relationships between micromechanical schemes according to the microcracks status and boundary conditions.

Appendix B

Supplement to Chapter II

B.1 2D Volume fraction of cracks

When a cracks family is modeled as a flat ellipse ellipsoid (Fig. 2.1b), volume fraction of $\mathcal{N}$ number of cracks per unit area, is defined by:

$$f_c = \mathcal{N} * \pi ac = \pi a^2 \left(\frac{c}{a}\right) \mathcal{N} = \pi d\omega \tag{B.1}$$

(a, c) are the mean semi-axes of the cracks, $\omega = {}^{c}/_{a}$ the mean aspect ratio and $d = \mathcal{N}a^2$ the crack density.

B.2 2D Depolarization tensor

The depolarization tensor in 2D is given by:

$$S_{ii} = \frac{a_1 a_2}{2} \int_0^\infty \frac{ds}{(a_i^2 + s)\sqrt{(a_1^2 + s)(a_2^2 + s)}} \quad (i = 1, 2) \tag{B.2}$$

and $S_{ij} = 0$ for $i \neq j$. For an ellipse with $a_1 = a$ and $a_2 = c$, Eq. (B.2) becomes:

$$S_{11} = \frac{ac}{2} \int_0^\infty \frac{ds}{(a^2 + s)\sqrt{(a^2 + s)(c^2 + s)}} \tag{B.3}$$

$$S_{22} = \frac{ac}{2} \int_0^\infty \frac{ds}{(c^2 + s)\sqrt{(a^2 + s)(c^2 + s)}} \tag{B.4}$$

Solving Eqs. (B.3) and (B.4), and considering the special case of flat-ellipse, i.e. $a \gg c$, one has:

$$S_1 = \frac{\omega}{1 + \omega} \qquad S_2 = \frac{1}{1 + \omega} \tag{B.5}$$

For an orthogonal base $(\mathbf{k}, \mathbf{n})$, the tensorial form of Eq. (B.5) can be written as

$$\mathbf{S}_E = S_1 \, \mathbf{k} \otimes \mathbf{k} + S_2 \, \mathbf{n} \otimes \mathbf{n} \tag{B.6}$$

Knowing that, $\mathbf{I} = \mathbf{k} \otimes \mathbf{k} + \mathbf{n} \otimes \mathbf{n}$, it comes:

$$\mathbf{S}_E = S_1 \, (\mathbf{I} - \mathbf{n} \otimes \mathbf{n}) + S_2 \, \mathbf{n} \otimes \mathbf{n} = \frac{\omega}{1 + \omega} \, (\mathbf{I} - \mathbf{n} \otimes \mathbf{n}) + \frac{1}{1 + \omega} \, \mathbf{n} \otimes \mathbf{n} \tag{B.7}$$

B.3 Calculation of the effective thermal resistivity

Using the same boundary condition used in Section 1.4, the following properties are derived. Starting with **Dilute scheme**, the respective flux concentration tensor is given in Eq. (1.33), therefore the effective tensor is given as:

$$\boldsymbol{\rho}_{hom}^{dil} = \Big[\mathbf{I} + \pi d\ \mathbf{R}\Big] \tag{B.8}$$

Knowing and expanding $\mathbf{R}$ tensor (Section 2.3), we get:

$$\boldsymbol{\rho}_{hom}^{dil} = \begin{cases} \boldsymbol{\rho}_m \cdot \Big[\mathbf{I} + \pi d\ \mathbf{n} \otimes \mathbf{n}\Big] & \text{, if cracks are open} \\ \boldsymbol{\rho}_m & \text{, if cracks are closed} \end{cases} \tag{B.9}$$

The above result for open case coincides with the one given by Sevostianov (2006), who calculated this solution using heat flux intensity factor around the crack tip.

While considering elliptical spatial distribution to account for interaction, **Mori-Tanaka scheme** is used. Its concentration tensor is given in Eq. (1.37). This leads to:

$$\boldsymbol{\rho}_{hom}^{MT} = \boldsymbol{\rho}_{hom}^{dil} \tag{B.10}$$

Ponte Castañeda-Willis bound allows to take any spatial distribution of cracks. Inline with previous works, we will consider a circular distribution. The simplified concentration tensor is (see Apprendix A.6.3):

$$\langle \mathbf{B} \rangle_c^{PCW} = \langle \mathbf{B} \rangle_c^{dil} \cdot \Big(\mathbf{I} - f_c\ \mathbf{Q}_d \cdot \big(\boldsymbol{\rho}_c - \boldsymbol{\rho}_m\big) \cdot \langle \mathbf{B} \rangle_c^{dil}\Big)^{-1} \tag{B.11}$$

From the equation above, the thermal resistivity is:

$$\boldsymbol{\rho}_{hom}^{PCW} = \boldsymbol{\rho}_m \cdot \left[\mathbf{I} + \pi\, d\, \mathbf{R} \cdot \left(\mathbf{I} - \frac{\pi\, d}{2}\, \mathbf{R}\right)^{-1}\right] \tag{B.12}$$

Substituting the limit tensor $\mathbf{R}$ and further simplification leads to:

$$\boldsymbol{\rho}_{hom}^{PCW} = \begin{cases} \boldsymbol{\rho}_m \cdot \left[\mathbf{I} + \pi d\ \dfrac{1}{1 - \frac{\pi d}{2}} \mathbf{n} \otimes \mathbf{n}\right] & \text{, if cracks are open} \\ \boldsymbol{\rho}_m & \text{, if cracks are closed} \end{cases} \tag{B.13}$$

Fig. B.1b presents the evolution of effective thermal resistivity for various schemes and bounds.

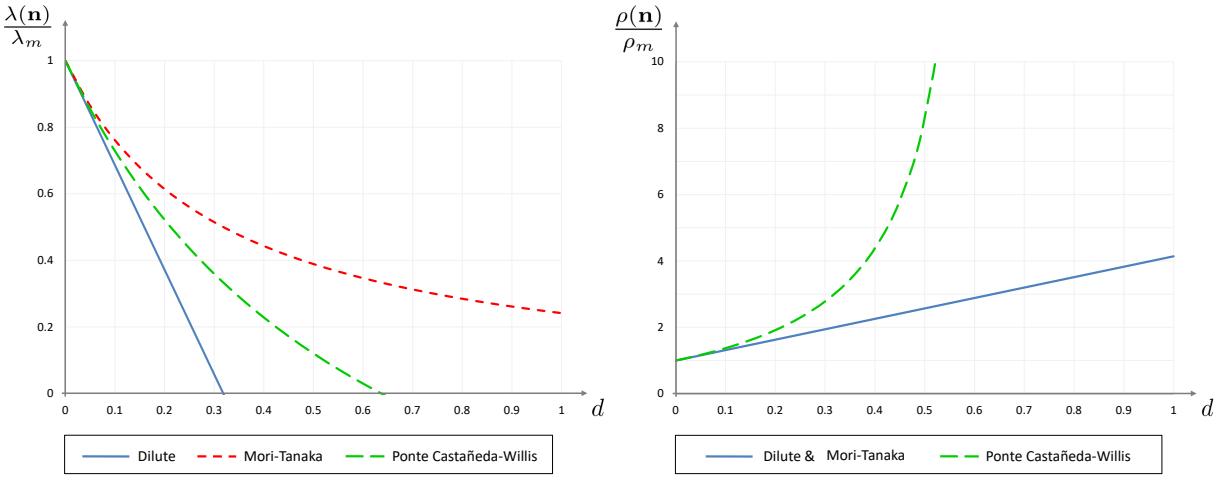

(a) Conductivity (b) Resistivity

FIGURE B.1: Prediction of generalized thermal conductivity $\lambda(\mathbf{n})$ and resistivity $\rho(\mathbf{n})$ for a material weakened by a single family of open microcrack with unit normal $\mathbf{n}$.

Appendix C

Supplement to Chapter III

C.1 Walpole base

The tensors $\mathbb{J}$ and $\mathbb{K}$ given by Walpole (1981)

$$\mathbb{J} = \frac{1}{3}\,\mathbf{I}\otimes\mathbf{I} \qquad\qquad \mathbb{K} = \mathbb{I} - \mathbb{J} \tag{C.1}$$

satisfy following conditions :

$$\mathbb{J} : \mathbb{J} = \mathbb{J}, \quad \mathbb{K} : \mathbb{K} = \mathbb{K}, \quad \mathbb{J} : \mathbb{K} = \mathbb{K} : \mathbb{J} = \mathbb{O} \tag{C.2}$$

so that any fourth order isotropic tensor $\mathbb{D} = \gamma\,\mathbb{J} + \delta\,\mathbb{K}$ has an inverse $\mathbb{D}^{-1} = \frac{1}{\gamma}\,\mathbb{J} + \frac{1}{\delta}\,\mathbb{K}$. Given a unit vector $\mathbf{n}$, Walpole also introduce the following base :

$$\begin{aligned}
&\mathbb{E}_1 = \frac{1}{2}(\mathbf{I}-\mathbf{n}\otimes\mathbf{n})\otimes(\mathbf{I}-\mathbf{n}\otimes\mathbf{n}), \quad \mathbb{E}_2 = \mathbf{n}\otimes\mathbf{n}\otimes\mathbf{n}\otimes\mathbf{n},\\
&\mathbb{E}_3 = (\mathbf{I}-\mathbf{n}\otimes\mathbf{n})\,\overline{\underline{\otimes}}\,(\mathbf{I}-\mathbf{n}\otimes\mathbf{n}) \;-\; \frac{1}{2}(\mathbf{I}-\mathbf{n}\otimes\mathbf{n})\otimes(\mathbf{I}-\mathbf{n}\otimes\mathbf{n}),\\
&\mathbb{E}_4 = \mathbf{n}\otimes\mathbf{n}\,\overline{\underline{\otimes}}\,(\mathbf{I}-\mathbf{n}\otimes\mathbf{n}) + (\mathbf{I}-\mathbf{n}\otimes\mathbf{n})\,\overline{\underline{\otimes}}\,\mathbf{n}\otimes\mathbf{n}, \quad \mathbb{E}_5 = \mathbf{n}\otimes\mathbf{n}\otimes(\mathbf{I}-\mathbf{n}\otimes\mathbf{n}),\\
&\mathbb{E}_6 = (\mathbf{I}-\mathbf{n}\otimes\mathbf{n})\otimes\mathbf{n}\otimes\mathbf{n}
\end{aligned} \tag{C.3}$$

Using Eq. (C.3), any fourth order transversely isotropic $\mathbb{D}$ can be decomposed as :

$$\mathbb{D} = e_1\,\mathbb{E}_1 + e_2\,\mathbb{E}_2 + e_3\,\mathbb{E}_3 + e_4\,\mathbb{E}_4 + e_5\,\mathbb{E}_5 + e_6\,\mathbb{E}_6 \tag{C.4}$$

which is simply expressed as

$$\mathbb{D} = [e_1, e_2, e_3, e_4, e_5, e_6] \tag{C.5}$$

In Walpole base, tensors $\mathbb{I}, \mathbb{J}$ and $\mathbb{K}$ can be expressed as:

$$\mathbb{I} = [1,1,1,1,0,0] \qquad \mathbb{J} = \left[\frac{2}{3},\frac{1}{3},0,0,\frac{1}{3},\frac{1}{3}\right] \qquad \mathbb{K} = \left[\frac{1}{3},\frac{2}{3},1,1,-\frac{1}{3},-\frac{1}{3}\right] \tag{C.6}$$

Note that, if $e_5 = e_6$ then tensor $\mathbb{D}$ is symmetric. Also,

$$\mathbf{I} : \mathbb{D} = [(e_1+e_5)\,(\mathbf{I}-\mathbf{n}\otimes\mathbf{n}) + (e_2+2e_6)\,\mathbf{n}\otimes\mathbf{n}] \tag{C.7}$$

where

$$\mathbb{D} : \mathbf{I} = [(e_1 + e_6)\,(\mathbf{I} - \mathbf{n} \otimes \mathbf{n}) + (e_2 + 2e_5)\,\mathbf{n} \otimes \mathbf{n}] \tag{C.8}$$

and for a symmetric $\mathbb{D}$ tensor Eqs. (C.7) and (C.8) yield to same result. If another fourth order tensor $\mathbb{D}' = [e'_1, e'_2, e'_3, e'_4, e'_5, e'_6]$ then their product $\mathbb{D} : \mathbb{D}'$ is:

$$\mathbb{D} : \mathbb{D}' = [e_1e'_1 + 2e_6e'_5, e_2e'_2 + 2e_5e'_6, e_3e'_3, e_4e'_4, e_5e'_1 + e_2e'_5, e_6e'_2 + e_1e'_6] \tag{C.9}$$

and finally the inverse of $\mathbb{D}$ can be given by:

$$\mathbb{D}^{-1} = \left[\frac{e_2}{l}, \frac{e_1}{l}, \frac{1}{e_3}, \frac{1}{e_4}, -\frac{e_5}{l}, -\frac{e_6}{l}\right] \tag{C.10}$$

with $l = e_1e_2 - 2e_5e_6$. Additionally, one has:

$$\mathbb{D} : \mathbb{D}'^T = [e_1e'_1 + 2e_6e'_6, e_2e'_2 + 2e_5e'_5, e_3e'_3, e_4e'_4, e_2e'_6 + e_5e'_1, e_1e'_5 + e_6e'_2] \tag{C.11}$$

with $\mathbb{D}'^T$ the transpose of tensor $\mathbb{D}'$.

One can thus provide expressions of some tensors in the base of Eq. (C.3) :

$$\mathbb{I} = \mathbb{E}_1 + \mathbb{E}_2 + \mathbb{E}_3 + \mathbb{E}_4 + = [1,\ 1,\ 1,\ 1,\ 0,\ 0] \tag{C.12}$$

$$\mathbb{J} = \frac{1}{3}\Big[2\,\mathbb{E}_1 + \mathbb{E}_2 + \mathbb{E}_5 + \mathbb{E}_6\Big] = \Big[\frac{2}{3},\ \frac{1}{3},\ 0,\ 0,\ \frac{1}{3},\ \frac{1}{3}\Big] \tag{C.13}$$

$$\mathbb{K} = \Big[\frac{1}{3},\ \frac{2}{3},\ 1,\ 1,\ -\frac{1}{3},\ -\frac{1}{3}\Big] \tag{C.14}$$

Besides, the matrix stiffness tensor $\mathbb{C}_m$ and compliance tensor $\mathbb{S}_m$ are on the form :

$$\mathbb{C}_m = \frac{E_m}{(1+\nu_m)(1-2\nu_m)}[1, 1-\nu_m, 1-2\nu_m, 1-2\nu_m, \nu_m, \nu_m] \tag{C.15}$$

$$\mathbb{S}_m = \frac{1}{E_m}[1-\nu_m, 1, 1+\nu_m, 1+\nu_m, -\nu_m, -\nu_m] \tag{C.16}$$

where E_m and ν_m is the Young's modulus and Poisson's ratio respectively. Finally, the spherical spatial distribution tensor $\mathbb{S}^d_c$ $(= \mathbb{P}^d_c : \mathbb{C}_m = \beta_1\mathbb{J} + \beta_2\mathbb{K})$ can be written as :

$$\mathbb{S}^d_c = \frac{1}{3}\ [\ 2\beta_1 + \beta_2,\ \beta_1 + 2\beta_2,\ 3\beta_2,\ 3\beta_2,\ \beta_1 - \beta_2,\ \beta_1 - \beta_2] \tag{C.17}$$

where β_1 and β_2 are given in Eq. (3.50).

C.2 Elasticity tensors for microcracked media

Following the same general framework of the study, several authors have derived elasticity tensors for microcracked media, including unilateral effects (Deudé *et al.* 2002, Zhu 2006, Dormieux and Kondo 2009).

- *Dilute scheme :*

$$\mathbb{C}^{dil}_{hom} = \mathbb{C}_m : \left[\mathbb{I} - \frac{4}{3}\pi \sum_{i/open} d_i\,\mathbb{T}_i - \frac{4}{3}\pi \sum_{i/closed} d_i\,\mathbb{T}'_i\right] \tag{C.18}$$

$$\mathbb{S}_{hom}^{dil} = \left(\mathbb{I} + \frac{4}{3}\pi \sum_{i/open} d_i \, \mathbb{T}_i + \frac{4}{3}\pi \sum_{i/closed} d_i \, \mathbb{T}'_i \right) : \mathbb{S}_m \tag{C.19}$$

- *Mori-Tanaka scheme :*

$$\mathbb{C}_{hom}^{MT} = \mathbb{C}_m : \left[\mathbb{I} + \frac{4}{3}\pi \left(\sum_{i/open} d_i \, \mathbb{T}_i + \sum_{i/closed} d_i \, \mathbb{T}'_i \right) \right]^{-1} \tag{C.20}$$

$$\mathbb{S}_{hom}^{MT} = \mathbb{S}_{hom}^{dil} \tag{C.21}$$

- *Ponte Castañeda-Willis bounds (upper bound for stiffness $\mathbb{C}_{hom}^{PCW}$ and lower bound for compliance $\mathbb{S}_{hom}^{PCW}$, with spherical distribution) :*

$$\mathbb{C}_{hom}^{PCW} = \mathbb{C}_m : \left[\mathbb{I} - \left(\frac{4}{3}\pi \sum_{i/open} d_i \, \mathbb{T}_i + \frac{4}{3}\pi \sum_{i/closed} d_i \, \mathbb{T}'_i \right) : \left(\mathbb{I} + \frac{4}{3}\pi \sum_{i/open} d_i \, \mathbb{S}_c^d : \mathbb{T}_i + \frac{4}{3}\pi \sum_{i/closed} d_i \, \beta_2 \, \mathbb{T}'_i \right)^{-1} \right] \tag{C.22}$$

$$\mathbb{S}_{hom}^{PCW} = \left[\mathbb{I} + \left(\mathbb{I} - \frac{4}{3}\pi \sum_{i/open} d_i \, \mathbb{T}_i : \mathbb{S}_m : \mathbb{Q}_c^d - \frac{4}{3}\pi \sum_{i/closed} d_i \, \mathbb{T}'_i : \mathbb{S}_m : \mathbb{Q}_c^d \right)^{-1} : \left(\frac{4}{3}\pi \sum_{i/open} d_i \, \mathbb{T}_i + \frac{4}{3}\pi \sum_{i/closed} d_i \, \mathbb{T}'_i \right) \right] : \mathbb{S}_m \tag{C.23}$$

with $\mathbb{T}_i$ and $\mathbb{T}'_i$ given in Eqs. (3.24) and (3.25) respectively.

C.3 Detailed calculation of specific heat

The specific heat capacity at constant strain for single family:

$$c_{\varepsilon,hom} = c_{\varepsilon,m} + f_c \left(c_{\varepsilon,c} - c_{\varepsilon,m} + T_0 \, (\boldsymbol{\kappa}_c - \boldsymbol{\kappa}_m) : \langle \mathbf{a} \rangle_c \right) \tag{C.24}$$

C.3.1 Dilute scheme

The thermal strain localization tensor in dilute scheme is:

$$\langle \mathbf{a} \rangle_c^{dil} = (\mathbb{I} - \langle \mathbb{A} \rangle_c^{dil}) : (\mathbb{C}_c - \mathbb{C}_m)^{-1} : (\boldsymbol{\kappa}_c - \boldsymbol{\kappa}_m) \qquad \text{with} \qquad \mathbb{C}_m = 3k_m \, \mathbb{J} + 2\mu_m \, \mathbb{K} \tag{C.25}$$

Open case

Recalling $\mathbb{C}_c = \mathbb{O}$, $\boldsymbol{\kappa}_c = \mathbf{0}$, $c_{\varepsilon,c} = 0$, $\mathbb{S}_m : \boldsymbol{\kappa}_m = \boldsymbol{\alpha}_m$, Eq. (C.24) and Eq. (C.25) simplify to:

$$c_{\varepsilon,hom}^{dil} = f_m \, c_{\varepsilon,m} - f_c \, T_0 \, \boldsymbol{\kappa}_m : \langle \mathbf{a} \rangle_c^{dil/open} = f_m \, c_{\varepsilon,m} - f_c \, T_0 \, \kappa_m \, \mathbf{I} : \langle \mathbf{a} \rangle_c^{dil/open} \tag{C.26}$$

$$\langle \mathbf{a} \rangle_c^{dil/open} = (\mathbb{I} - \langle \mathbb{A} \rangle_c^{dil/open}) : \boldsymbol{\alpha}_m \tag{C.27}$$

Substituting Eq. (C.27) in (C.26)

$$c_{\varepsilon,hom}^{dil} = f_m \, c_{\varepsilon,m} - f_c \, T_0 \, \alpha_m \, \kappa_m \, \mathbf{I} : (\mathbb{I} - \langle \mathbb{A} \rangle_c^{dil/open}) : \mathbf{I} \tag{C.28}$$

Considering limit case for the equation above,

$$c_{\varepsilon,hom}^{dil} = c_{\varepsilon,m} - \frac{4}{3} \pi d \, T_0 \, \alpha_m \, \kappa_m \, X \quad \text{with } X = \lim_{\omega \to 0} \omega \, \mathbf{I} : (\mathbb{I} - \langle \mathbb{A} \rangle_c^{dil/open}) : \mathbf{I} \tag{C.29}$$

simplification of X gives:

$$X = \lim_{\omega \to 0} \omega \, (\mathbf{I} - \mathbf{I} : \langle \mathbb{A} \rangle_c^{dil/open}) : \mathbf{I} = -\mathbf{I} : \mathbb{T} : \mathbf{I} = -\frac{4}{\pi} \left(\frac{1 - \nu_m^2}{1 - 2\nu_m} \right) \tag{C.30}$$

and:

$$c_{\varepsilon,hom}^{dil} = c_{\varepsilon,m} + T_0 \, \alpha_m \, \kappa_m \, \frac{16}{3} \left(\frac{1 - \nu_m^2}{1 - 2\nu_m} \right) d = c_{\varepsilon,m} + (1 + \nu_m) \, T_0 \, \alpha_m \, \kappa_m \, a_1 \, d \tag{C.31}$$

Closed case

For closed case,

$$\langle \mathbf{a} \rangle_c^{dil/closed} = (\mathbb{I} - \langle \mathbb{A} \rangle_c^{dil/closed}) : (2\mu_m \mathbb{K})^{-1} : \kappa_m \, (1 - \psi) \, \mathbf{I} \tag{C.32}$$

$$c_{\varepsilon,hom}^{dil} = c_{\varepsilon,m} + f_c \, \left(c_{\varepsilon,c} - c_{\varepsilon,m} \right) - f_c \, T_0 \, \kappa_m \, (1 - \psi) \, \mathbf{I} : \langle \mathbf{a} \rangle_c^{dil/closed} \tag{C.33}$$

From these equations,

$$c_{\varepsilon,hom}^{dil} = c_{\varepsilon,m} + f_c \, \left(c_{\varepsilon,c} - c_{\varepsilon,m} \right) - f_c \, T_0 \, \kappa_m^2 \, (1 - \psi^2) \, \mathbf{I} : (\mathbb{I} - \langle \mathbb{A} \rangle_c^{dil/closed}) : (2\mu_m \mathbb{K})^{-1} : \mathbf{I} \tag{C.34}$$

Tending to the limit case,

$$c_{\varepsilon,hom}^{dil} = c_{\varepsilon,m} - \frac{4}{3} \pi d \, T_0 \, \kappa_m^2 \, (1 - \psi^2) \, X' \quad \text{with } X' = \lim_{\omega \to 0} \omega \, \mathbf{I} : (\mathbb{I} - \langle \mathbb{A} \rangle_c^{dil/closed}) : (2\mu_m \mathbb{K})^{-1} : \mathbf{I} \tag{C.35}$$

According to the development explained in Chapter 3, it comes to $X' = 0$ and:

$$c_{\varepsilon,hom}^{dil} = c_{\varepsilon,m} \tag{C.36}$$

C.3.2 Mori-Tanaka scheme

The thermal localization tensor for single family of cracks is given by:

$$\langle \mathbf{a} \rangle_c^{MT} = \langle \mathbf{a} \rangle_c^{dil} - \langle \mathbb{A} \rangle_c^{MT} : f_c \, \langle \mathbf{a} \rangle_c^{dil} \quad \text{and} \quad \mathbb{A}_c^{MT} = \mathbb{A}_c^{dil} : \mathbb{G} \tag{C.37}$$

Open case

$$
\begin{aligned}
c^{MT}_{\varepsilon,hom} &= f_m\, c_{\varepsilon,m} - f_c\, T_0\ \kappa_m\ \mathbf{I} : \langle \mathbf{a} \rangle^{MT/open}_c && \text{(C.38)}\\
&= f_m\, c_{\varepsilon,m} - f_c\, T_0\ \kappa_m\ \mathbf{I} : \left(\langle \mathbf{a} \rangle^{dil/open}_c - \langle \mathbb{A} \rangle^{MT/open}_c : f_c\ \langle \mathbf{a} \rangle^{dil/open}_c \right) && \text{(C.39)}\\
&= c^{dil/open}_{\varepsilon,hom} + f_c\, T_0\ \kappa_m\ \mathbf{I} : \langle \mathbb{A} \rangle^{MT/open}_c : f_c\ \langle \mathbf{a} \rangle^{dil/open}_c && \text{(C.40)}\\
&= c^{dil/open}_{\varepsilon,hom} + \frac{4}{3}\pi d\omega\, T_0\ \kappa_m\ \mathbf{I} : \langle \mathbb{A} \rangle^{MT/open}_c : \frac{4}{3}\pi d\omega\ \langle \mathbf{a} \rangle^{dil/open}_c && \text{(C.41)}
\end{aligned}
$$

Applying limit case,

$$
c^{MT}_{\varepsilon,hom} = c^{dil/open}_{\varepsilon,hom} + \frac{4}{3}\pi d\, T_0\ \kappa_m\ \mathbf{I} : \mathbb{T} : \mathbb{G}^{open} : \mathbf{M}^{open} \qquad \text{(C.42)}
$$

with

$$
\mathbb{G}^{open} = \left[\mathbb{I} + \frac{4}{3}\pi d\, \mathbb{T} \right]^{-1} \text{ and } \mathbf{M}^{open} = \frac{4}{3}\pi d \lim_{\omega \to 0} \omega\ \langle \mathbf{a} \rangle^{dil/open}_c \qquad \text{(C.43)}
$$

Since,

$$
\mathbb{G}^{open} : \mathbf{M}^{open} = -\frac{a_1}{a_2^{MT}} (1 + \nu_m)\, \alpha_m\, d\ \ \mathbf{n} \otimes \mathbf{n} \qquad \text{(C.44)}
$$

Then

$$
\mathbf{I} : \mathbb{T} : \mathbb{G}^{open} : \mathbf{M}^{open} = -\frac{4}{\pi} \frac{a_1}{a_2^{MT}} (1 - \nu_m^2) \left(\frac{1 - \nu_m}{1 - 2\nu_m} \right) \alpha_m d \qquad \text{(C.45)}
$$

So, Eq. (C.42) comes to:

$$
c^{MT}_{\varepsilon,hom} = c^{dil}_{\varepsilon,hom} - T_0\, \alpha_m\, \kappa_m\, \frac{a_1^2}{a^{MT}}\, d^2\, (1 - \nu_m^2) \qquad \text{(C.46)}
$$

$$
\begin{aligned}
c^{MT}_{\varepsilon,hom} &= c_{\varepsilon,m} + T_0\, \alpha_m\, \kappa_m\, a_1\, d\, (1 + \nu_m) - T_0\, \alpha_m\, \kappa_m\, \frac{a_1^2}{a_2^{MT}}\, d^2\, (1 - \nu_m^2) && \text{(C.47)}\\
&= c_{\varepsilon,m} + T_0\, \alpha_m\, \kappa_m\, a_1\, d\, (1 + \nu_m) \left[1 - \frac{a_1}{a_2^{MT}}\, d\, (1 - \nu_m) \right] && \text{(C.48)}\\
&= c_{\varepsilon,m} + (1 + \nu_m)\, T_0\, \alpha_m\, \kappa_m\, \frac{a_1}{a_2^{MT}}\, d && \text{(C.49)}
\end{aligned}
$$

Closed case

$$
\begin{aligned}
c^{MT}_{\varepsilon,hom} &= c_{\varepsilon,m} + f_c\, \left(c_{\varepsilon,c} - c_{\varepsilon,m} \right) - f_c\ T_0\ \kappa_m\ (1 - \psi)\ \mathbf{I} : \langle \mathbf{a} \rangle^{MT/closed}_c && \text{(C.50)}\\
&= c^{dil/closed}_{\varepsilon,m} + f_c\ T_0\ \kappa_m\ (1 - \psi)\ \mathbf{I} : \langle \mathbb{A} \rangle^{MT/closed}_c : f_c\ \langle \mathbf{a} \rangle^{dil/closed}_c && \text{(C.51)}\\
&= c^{dil/closed}_{\varepsilon,m} + \frac{4}{3}\pi d\, \omega\, T_0\, \kappa_m\, (1 - \psi)\, \mathbf{I} : \langle \mathbb{A} \rangle^{MT/closed}_c : \frac{4}{3}\pi d\, \omega\, \langle \mathbf{a} \rangle^{dil/closed}_c && \text{(C.52)}\\
&= c^{dil/closed}_{\varepsilon,m} + \frac{4}{3}\pi d\, T_0\, \kappa_m\, (1 - \psi)\, \mathbf{I} : \mathbb{T}' : \mathbb{G}^{closed} : \mathbf{M}^{closed} && \text{(C.53)}
\end{aligned}
$$

with $\mathbb{G}^{closed} = \left[\mathbb{I} + \frac{4}{3}\pi d\, \mathbb{T}' \right]^{-1}$ and $\mathbf{M}^{closed} = \frac{4}{3}\pi d \lim_{\omega \to 0} \omega\ \langle \mathbf{a} \rangle^{dil/closed}_c$.

Since:

$$
\mathbb{G}^{closed} : \mathbf{M}^{closed} = \mathbf{0} \qquad \text{(C.54)}
$$

Then:

$$c_{\varepsilon,hom}^{MT} = c_{\varepsilon,m}^{dil/closed} = c_{\varepsilon,m} \tag{C.55}$$

C.3.3 Ponte Castañeda-Willis bound

The thermal localization tensor for single family of cracks is

$$\langle \mathbf{a} \rangle_c^{PCW} = -\left(\mathbb{C}_c - \mathbb{C}_m\right)^{-1} : \left(\langle \mathbb{A} \rangle_c^{PCW} - \mathbb{I}\right)^T : \left(\boldsymbol{\kappa}_c - \boldsymbol{\kappa}_m\right) \tag{C.56}$$

Open case

In the open state, above thermal localization tensor reads:

$$\langle \mathbf{a} \rangle_c^{PCW/open} = -\mathbb{C}_m^{-1} : \mathbb{Z}^{open} \tag{C.57}$$

where

$$\mathbb{Z}^{open} = -\kappa_m \mathbf{I} : \left(\langle \mathbb{A} \rangle_c^{dil/open} : \mathbb{H}^{open} - \mathbb{I}\right) \tag{C.58}$$

and $\mathbb{H}^{open} = \left[\mathbb{I} + \dfrac{4}{3}\pi d\, \mathbb{S}_c^d : \mathbb{T}\right]^{-1}$. For the limit case, one has:

$$c_{\varepsilon,hom}^{PCW} = c_{\varepsilon,m} + \frac{4}{3}\pi d\, T_0\, \kappa_m^2\, \mathbf{I} : \mathbb{C}_m^{-1} : \left(\mathbb{T} : \mathbb{H}^{open}\right)^T : \mathbf{I} \tag{C.59}$$

Since $\mathbf{I} : \mathbb{C}_m^{-1} = \frac{1}{3k_m}\mathbf{I}$ and

$$\left(\mathbb{T} : \mathbb{H}^{open}\right)^T : \mathbf{I} = \mathbf{I} : \mathbb{T} : \mathbb{H}^{open} = \frac{4}{\pi}\frac{1}{a_2^{PCW}}\left(\frac{1-\nu_m}{1-2\nu_m}\right)\left[(1-\nu_m)\,\mathbf{n}\otimes\mathbf{n} + \nu_m(\mathbf{I} - \mathbf{n}\otimes\mathbf{n})\right] \tag{C.60}$$

it comes finally:

$$c_{\varepsilon,hom}^{PCW} = c_{\varepsilon,m} + (1+\nu_m)\, T_0\, \alpha_m\, \kappa_m\, \frac{a_1}{a_2^{PCW}}\, d \tag{C.61}$$

Closed case

Introducing function F allows to express the thermal localization tensor as:

$$\langle \mathbf{a} \rangle_c^{PCW/closed} = -\lim_{b\to 0} \mathbb{F}(b) : \mathbb{Z}^{closed} \tag{C.62}$$

where

$$\mathbb{Z}^{closed} = -\kappa_m(1-\psi)\mathbf{I} : \left(\langle \mathbb{A} \rangle_c^{dil/closed} : \mathbb{H}^{closed} - \mathbb{I}\right) \tag{C.63}$$

and $\mathbb{H}^{closed} = \left[\mathbb{I} + \dfrac{4}{3}\pi\beta_2 d\, \mathbb{T}'\right]^{-1}$. Considering again the limit case $\omega \to 0$, it comes:

$$c_{\varepsilon,hom}^{PCW} = c_{\varepsilon,m} - \frac{4}{3}\pi d\, T_0\, (1-\psi)^2 \kappa_m^2 \lim_{b\to 0} \mathbf{I} : \mathbb{F}(b) : \left(\mathbb{T}' : \mathbb{H}^{closed}\right)^T : \mathbf{I} \tag{C.64}$$

It can be shown that $\mathbb{F}(b) : \left(\mathbb{T}' : \mathbb{H}^{closed}\right)^T$ does not depend on b and that

$$\mathbb{F}(b) : \left(\mathbb{T}' : \mathbb{H}^{closed}\right)^T : \mathbf{I} = \mathbf{0} \tag{C.65}$$

Accordingly,

$$c_{\varepsilon,hom}^{PCW} = c_{\varepsilon,m} \tag{C.66}$$

References

Abdulagatova, Z., **Abdulagatov, I.M.**, **Emirov, V.N.** (2009). *Effect of temperature and pressure on the thermal conductivity of sandstone.* International Journal of Rock Mechanics and Mining Sciences, 46(6):1055–1071.

Andrieux, S., **Bamberger, Y.**, **Marigo, J.** (1986). *un modèle de matériau microfissuré pour les béton et les roches.* Journal de Mécanique Théorique et Appliquée, 5:471–513.

Baste, S., **Aristégui, C.** (1998). *Induced anisotropy and crack systems orientations of a ceramic matrix composite under off-principal axis loading.* Mechanics of Materials, 29(1):19–41.

Benveniste, Y. (1987). *A new approach to the application of Mori-Tanaka's theory in composite materials.* Mechanics of Materials, 6(2):147–157.

Benveniste, Y., **Dvorak, G.J.** (1990). *On a Correspondence Between Mechanical and Thermal Effects in Two-Phase Composites.* In: G.J. Weng, M. Taya, H. Abé (editors), *Micromechanics and Inhomogeneity.* Springer New York, New York, NY, pages 65–81.

Benveniste, Y., **Miloh, T.** (1989). *An exact solution for the effective thermal conductivity of cracked bodies with oriented elliptical cracks.* Journal of Applied Physics, 66(1):176–180.

Benveniste, Y., **Dvorak, G.**, **Chen, T.** (1991). *On diagonal and elastic symmetry of the approximate effective stiffness tensor of heterogeneous media.* Journal of the Mechanics and Physics of Solids, 39(7):927–946.

Berryman, J.G. (1997). *Generalization of Eshelby's formula for a single ellipsoidal elastic inclusion to poroelasticity and thermoelasticity.* Physical Review Letters, 79(6):1142–1145.

Bristow, J.R. (1960). *Microcracks, and the static and dynamic elastic constants of annealed and heavily cold-worked metals.* British Journal of Applied Physics, 11(2):81–85.

Budiansky, B., **O'Connell, R.J.** (1976). *Elastic moduli of a cracked solid.* International Journal of Solids and Structures, 12(2):81–97.

Buessem, W.R., **Lange, F.F.** (1966). *Residual stresses in anisotropic ceramics.* Interceram, 15:229–231.

Buryachenko, V.A. (2007). *Micromehcanics of heterogenous materials.* Springer US, Boston, MA.

Böhm, H.J. (2019). *A short introduction to basic aspects of continuum microcmechanics.* Vienna University of Technology.

Cao, H., **Evans, A.G.** (1993). *Nonlinear deformation of ferroelectric ceramics.* Journal of the American Ceramic Society, 76(4):890–896.

Carson, J.K., **Lovatt, S.J.**, **Tanner, D.J.**, **Cleland, A.C.** (2003). *An analysis of the influence of material structure on the effective thermal conductivity of theoretical porous materials using finite element simulations.* International Journal of Refrigeration, 26(8):873–880.

Case, E.D., **Smyth, J.R.**, **Hunter, O.** (1981). *Microcracking in Large-grain* Al_2O_3. Materials Science and Engineering, 51(2):175–179.

Chaboche, J.L. (1992). *Damage Induced Anisotropy: On the Difficulties Associated with the Active/Passive Unilateral Condition.* International Journal of Damage Mechanics, 1(2):148–171.

Chen, Y., **Li, D.**, **Jiang, Q.**, **Zhou, C.** (2012a). *Micromechanical analysis of anisotropic damage and its influence on effective thermal conductivity in brittle rocks.* International Journal of Rock Mechanics and Mining Sciences, 50:102–116.

Chen, Y.L., **Ni, J.**, **Shao, W.**, **Azzam, R.** (2012b). *Experimental study on the influence of temperature on the mechanical properties of granite under uni-axial compression and fatigue loading.* International Journal of Rock Mechanics and Mining Sciences, 56:62–66.

Cormery, F., **Welemane, H.** (2002). *A critical review of some damage models with unilateral effect.* Mechanics Research Communications, 29(5):391–395.

Damhof, F.E. (2010). *Numerical-experimental analysis of thermal shock damage in refractory materials.* Corus Technology.

Deudé, V., **Dormieux, L.**, **Kondo, D.**, **Pensée, V.** (2002). *Propriétés élastiques non linéaires d'un milieu mésofissuré.* Comptes Rendus Mécanique, 330(8):587–592.

Dormieux, L., **Kondo, D.** (2009). *Stress-based estimates and bounds of effective elastic properties: The case of cracked media with unilateral effects.* Computational Materials Science, 46(1):173–179.

Dormieux, L., **Kondo, D.** (2016). *Micromechanics of fracture and damage*. John Wiley & Sons, Inc., Hoboken, NJ, USA.

Dormieux, L., **Kondo, D.**, **Ulm, F.J.** (2006). *Microporomechanics*. John Wiley & Sons, Ltd, Chichester, UK.

Dvorak, G. (2013). *Micromechanics of composite materials*, *Solid mechanics and its applications*, volume 186. Springer Netherlands, Dordrecht.

Eshelby, J.D. (1957). *The determination of the elastic field of an ellipsoidal inclusion, and related problems*. Proceedings of the Royal Society A: Mathematical, Physical and Engineering Sciences, 241(1226):376–396.

Evans, A.G., **Zok, F.W.** (1994). *The physics and mechanics of fibre-reinforced brittle matrix composites*. Journal of Materials Science, 29(15):3857–3896.

Fernández, M., **Böhlke, T.** (2018). *Hashin-Shtrikman bounds with eigenfields in terms of texture coefficients for polycrystalline materials*. Acta Materialia, 165:686–697.

Fertig, R.S., **Nickerson, S.T.** (2015). *Towards prediction of thermally induced microcrack initiation and closure in porous ceramics*. Journal of the American Ceramic Society, 99(2):581–588.

François, D., **Pineau, A.**, **Zaoui, A.** (2012). *Mechanical Behaviour of Materials: Volume 1: Micro- and Macroscopic Constitutive Behaviour*, *Solid mechanics and its applications*, volume 180. Springer Netherlands, Dordrecht.

Gardner, D.R., **Lark, R.J.**, **Barr, B.** (2005). *Effect of conditioning temperature on the strength and permeability of normal- and high-strength concrete*. Cement and Concrete Research, 35(7):1400–1406.

Germain, P., **Nguyen, Q.S.**, **Suquet, P.** (1983). *Continuum Thermodynamics*. Journal of Applied Mechanics, 50(4b):1010–1020.

Ghassemi Kakroudi, M. (2007). *Comportement thermomécanique en traction de bétons réfractaires : influence de la nature des agrégats et de l'histoire thermique*. Ph.D. thesis, Université de Limoges.

Giraud, A., **Gruescu, C.**, **Do, D.P.**, **Homand, F.**, **Kondo, D.** (2007). *Effective thermal conductivity of transversely isotropic media with arbitrary oriented ellipsoïdal inhomogeneities*. International Journal of Solids and Structures, 44(9):2627–2647.

Goidescu, C., **Welemane, H.**, **Kondo, D.**, **Gruescu, C.** (2013). *Microcracks closure effects in initially orthotropic materials*. European Journal of Mechanics - A/Solids, 37:172–184.

Griffiths, L., **Heap, M.J.**, **Baud, P.**, **Schmittbuhl, J.** (2017). *Quantification of microcrack characteristics and implications for stiffness and strength of granite.* International Journal of Rock Mechanics and Mining Sciences, 100:138–150.

Hashin, Z. (1983). *Analysis of composite materials - A survey.* Journal of Applied Mechanics, 50(3):481–505.

Hashin, Z. (1988). *The differential scheme and its application to cracked materials.* Journal of the Mechanics and Physics of Solids, 36(6):719–734.

Hashin, Z., **Shtrikman, S.** (1963). *A variational approach to the theory of the elastic behaviour of multiphase materials.* Journal of the Mechanics and Physics of Solids, 11(2):127–140.

Hatta, H., **Taya, M.** (1986). *Equivalent inclusion method for steady state heat conduction in composites.* International Journal of Engineering Science, 24(7):1159–1172.

Hill, R. (1963). *Elastic properties of reinforced solids: Some theoretical principles.* Journal of the Mechanics and Physics of Solids, 11(5):357–372.

Hill, R. (1965). *A self-consistent mechanics of composite materials.* Journal of the Mechanics and Physics of Solids, 13(4):213–222.

Hoenig, A. (1983). *Thermal conductivities of a cracked solid.* Journal of Composite Materials, 17(3):231–237.

Homand-Etienne, F., **Houpert, N.**, **Tisot, J.P.** (1987). *La fissuration thermique dans le grès de Fontainebleau.* Greco Geomatériaux, (44):46–61.

Horii, H., **Nemat-Nasser, S.** (1983). *Overall moduli of solids with microcracks: Load-induced anisotropy.* Journal of the Mechanics and Physics of Solids, 31(2):155–171.

Jen, S.H., **Bertrand, J.A.**, **George, S.M.** (2011). *Critical tensile and compressive strains for cracking of Al_2O_3 films grown by atomic layer deposition.* Journal of Applied Physics, 109(8):084305.

Kachanov, M. (1993). *Elastic solids with many cracks and related problems.* In: *Advances in applied mechanics*, volume 30. Elsevier, pages 259–445.

Kanaun, S. (1980). *The poisson set of cracks in an elastic continuous medium.* Journal of Applied Mathematics and Mechanics, 44(6):808–815.

Karch, C. (2014). *Micromechanical analysis of thermal expansion coefficients.* Modeling and Numerical Simulation of Material Science, 04(03):104–118.

Kim, R.Y., **Crastoa, A.S.**, **Schoeppner, G.A.** (2000). *Dimensional stability of composite in a space thermal environment.* Composites Science and Technology, 60(12-13):2601–2608.

Kim, B.C., **Chen, J.**, **Kim, J.Y.** (2020). *Relation between crack density and acoustic nonlinearity in thermally damaged sandstone.* International Journal of Rock Mechanics and Mining Sciences, 125:104171.

Laws, N. (1973). *On the thermostatics of composite materials.* Journal of the Mechanics and Physics of Solids, 21(1):9–17.

Lejeunes, S., **Bourgeois, S.** (2011). *Une Toolbox Abaqus pour le calcul de propriétés effectives de milieux hétérogènes.* In: *10ème Colloque National en Calcul des Structures.* HAL, Giens, France.

Levin, V.M. (1967). *Thermal expansion coefficient of heterogeneous materials.* Mechanics of Solids, 2:58–61.

Lin, W. (2002). *Permanent strain of thermal expansion and thermally induced microcracking in Inada granite.* Journal of Geophysical Research, 107(B10):ECV 3–1–ECV 3–16.

Lu, T.J., **Hutchinson, J.W.** (1995). *Effect of matrix cracking on the overall thermal conductivity of fibre-reinforced composites.* Philosophical Transactions of the Royal Society of London. Series A: Mathematical, Physical and Engineering Sciences, 351(1697):595–610.

Maitournam, H. (2017). *Matériaux et structures anélastiques.* Ecole Polytechnique.

Mori, T., **Tanaka, K.** (1973). *Average stress in matrix and average elastic energy of materials with misfitting inclusions.* Acta Metallurgica, 21(5):571–574.

Morvan, J.M., **Baste, S.** (1998). *Effect of the Opening/Closure of Microcracks on the Nonlinear Behavior of a 2D C-SiC Composite under Cyclic Loading.* International Journal of Damage Mechanics, 7(4):381–402.

Mura, T. (1987). *Micromechanics of defects in solids*, *Mechanics of elastic and inelastic solids*, volume 3. Springer Netherlands, Dordrecht.

Nechnech, W., **Meftah, F.**, **Reynouard, J.M.** (2002). *An elasto-plastic damage model for plain concrete subjected to high temperatures.* Engineering Structures, 24(5):597–611.

Nemat-Nasser, S., **Hori, M.** (1993). *Micromechanics: Overall properties of heterogeneous materials.* North-holland, Amsterdam.

Nguyen, S.T., **Vu, M.**, **Vu, M.N.**, **Tang, A.M.** (2017). *Modeling of heat flow and effective thermal conductivity of fractured media: Analytical and numerical methods.* Journal of Applied Geophysics, 140:117–122.

Pensée, V., **Kondo, D.** (2001). *Une analyse micromécanique 3-D de l'endommagement par mésofissuration.* Comptes Rendus de l'Académie des Sciences - Series IIB - Mechanics, 329(4):271–276.

Pietrak, K., **Wiśniewski, T.S.** (2015). *A review of models for effective thermal conductivity of composite materials.* Journal of Power Technologies, 95(1):14–24.

Ponte Castañeda, P. (2002). *Heterogeneous materials.* Ecole Polytechnique.

Ponte Castañeda, P., **Willis, J.R.** (1995). *The effect of spatial distribution on the effective behavior of composite materials and cracked media.* Journal of the Mechanics and Physics of Solids, 43(12):1919–1951.

Rangasamy Mahendren, S.R., **Welemane, H.**, **Dalverny, O.**, **Tongne, A.** (2019). *Thermal conduction properties of microcracked media: Accounting for the unilateral effect.* Comptes Rendus Mécanique, 347(12):944–952.

Rangasamy Mahendren, S.R., **Welemane, H.**, **Dalverny, O.**, **Tongne, A.** (2020a). *Steady-state heat transfer in microcracked media.* Mechanics & Industry, 21:519.

Rangasamy Mahendren, S.R., **Welemane, H.**, **Dalverny, O.**, **Tongne, A.** (2020b). *Effective thermoelastic properties of brittle materials: micromechanical estimations for open and closed state of microcracks.* Euro. J. Mech. A/Solids, submitted.

Reinhardt, H.W. (1984). *Fracture mechanics of elastic softening materials like concrete*, volume 29. Heron.

Rosen, B., **Hashin, Z.** (1970). *Effective thermal expansion coefficients and specific heats of composite materials.* International Journal of Engineering Science, 8(2):157–173.

Sevostianov, I. (2006). *Thermal conductivity of a material containing cracks of arbitrary shape.* International Journal of Engineering Science, 44(8-9):513–528.

Sevostianov, I., **Giraud, A.** (2013). *Generalization of Maxwell homogenization scheme for elastic material containing inhomogeneities of diverse shape.* International Journal of Engineering Science, 64:23–36.

Sevostianov, I., **Kachanov, M.** (2019). *On the effective properties of polycrystals with intergranular cracks.* International Journal of Solids and Structures, 156-157:243–250.

Shafiro, B., **Kachanov, M.** (2000). *Anisotropic effective conductivity of materials with nonrandomly oriented inclusions of diverse ellipsoidal shapes.* Journal of Applied Physics, 87(12):8561–8569.

Shen, L., **Ren, Q.**, **Xia, N.**, **Sun, L.**, **Xia, X.** (2015). *Mesoscopic numerical simulation of effective thermal conductivity of tensile cracked concrete.* Construction and Building Materials, 95:467–475.

Shiliang, W., **Hong, Z.**, **Juntao, J.**, **Yunfeng, L.** (2015). *Investigation on surface micro-crack evaluation of engineering ceramics by rotary ultrasonic grinding machining.* The International Journal of Advanced Manufacturing Technology, 81(1-4):483–492.

Sibai, M., **Dormieux, L.**, **Pensée, V.**, **Kondo, D.** (2003). *Effets de la microfissuration en poroélasticité des roches: étude expérimentale et analyse théorique.* In: *16ème Congrés Français de Mécanique.* Nice, France.

Su, D., **Santare, M.H.**, **Gazonas, G.A.** (2008). *An effective medium model for elastic waves in microcrack damaged media.* Engineering Fracture Mechanics, 75(14):4104–4116.

Sævik, P.N., **Berre, I.**, **Jakobsen, M.**, **Lien, M.** (2013). *A 3D computational study of effective medium methods applied to fractured media.* Transport in Porous Media, 100(1):115–142.

Tang, S.B., **Tang, C.A.** (2015). *Crack propagation and coalescence in quasi-brittle materials at high temperatures.* Engineering Fracture Mechanics, 134:404–432.

Tang, S., **Tang, C.**, **Liang, Z.**, **Zhang, Y.**, **Li, L.** (2012). *Numerical study of the influence of material structure on effective thermal conductivity of concrete.* Heat Transfer Engineering, 33(8):732–747.

Tappin, G., **Davidge, R.W.**, **McLaren, J.R.** (1978). *The strength of ceramics under biaxial stresses.* In: *Flaws and Testing.* Springer US, Boston, MA, pages 435–449.

Terrien, M. (1980). *Emission acoustique et "comportement mécanique post-critique" d'un béton sollicité en traction.* Bulletin de liaison des laboratoires des ponts et chaussees.

Torquato, S. (2002). *Random heterogeneous materials: Microstructure and macroscopic properties*, *Interdisciplinary Applied Mathematics*, volume 16. Springer+Business Media, New York.

Tran, A.B., **Vu, M.N.**, **Nguyen, S.T.**, **Dong, T.Q.**, **Le-Nguyen, K.** (2018). *Analytical and numerical solutions for heat transfer and effective thermal conductivity of cracked media.* Journal of Applied Geophysics, 149:35–41.

Valdiviezo-Mijangos, O.C., **Rodríguez-Ramos, R.**, **Sabina, F.J.**, **Guinovart-Díaz, R.**, **Bravo-Castillero, J.**, **Padilla-Longoria, P.** (2020). *Thermoelastic bounds and self-consistent estimation for the overall properties of composites.* Mechanics Research Communications.

Valès, B., **Munoz, V.**, **Welemane, H.**, **Pastor, M.L.**, **Trajin, B.**, **Perrin, M.**, **Cantarel, A.**, **Karama, M.** (2016). *Heat source estimation in anisotropic materials.* Composite Structures, 136:287–296.

Vejmelková, E., **Padevět, P.**, **Černý, R.** (2008). *Effect of cracks on hygric and thermal characteristics of concrete.* Bauphysik, 30(6):438–444.

Vu, X.H. (2007). *Caractérisation expérimentale du béton sous fort confinement: influences du degré de saturation et du rapport eau/ciment.* Ph.D. thesis, Université Joseph Fourier.

Vu, M.N., **Nguyen, S.T.**, **Vu, M.H.**, **Tang, A.M.**, **To, V.T.** (2015). *Heat conduction and thermal conductivity of 3D cracked media.* International Journal of Heat and Mass Transfer, 89:1119–1126.

Walpole, L.J. (1981). *Elastic behavior of composite materials: theoretical foundations.* In: *Advances in applied mechanics volume 21*, *Advances in Applied Mechanics*, volume 21. Elsevier, pages 169–242.

Wang, X.D., **Jiang, L.Y.** (2003). *The effective electroelastic property of piezoelectric media with parallel dielectric cracks.* International Journal of Solids and Structures, 40(20):5287–5303.

Welemane, H., **Cormery, F.** (2002). *Some remarks on the damage unilateral effect modelling for microcracked materials.* International Journal of Damage Mechanics, 11(1):65–86.

Willis, J.R. (1977). *Bounds and self-consistent estimates for the overall properties of anisotropic composites.* Journal of the Mechanics and Physics of Solids, 25(3):185–202.

Willis, J.R. (2002). *Mechanics of composites.* Ecole Polytechnique.

Wong, H.C., **Chau, K.T.**, **Wang, P.** (1996). *Microcracking and grain size effect in Yuen Long marbles.* International Journal of Rock Mechanics and Mining Sciences & Geomechanics Abstracts, 33(5):479–485.

Wu, T., **Wriggers, P.** (2014). *Effects of debonding on thermal conduction and humidity diffusion at mesoscale of concrete.* Proceedings in Applied Mathematics and Mechanics, 14(1):489–490.

Zaoui, A. (2002). *Continuum Micromechanics: Survey.* Journal of Engineering Mechanics, 128(8):808–816.

Zhao, Y., **Huang, J.**, **Wang, R.** (1993). *Real-time SEM observations of the microfracturing process in rock during a compression test.* International Journal of Rock Mechanics and Mining Sciences & Geomechanics Abstracts, 30(6):643–652.

Zhu, Q.Z. (2006). *Applications des approches d'homogénéisation à la modélisation tridimensionnelle de l'endommagement des matériaux quasi fragiles : formulations, validations et implémentations numériques.* Ph.D. thesis, Université de Lille.

Zimmerman, R.W. (1985). *The effect of microcracks on the elastic moduli of brittle materials*. Journal of Materials Science Letters, 4(12):1457–1460.

Thermomechanical behaviour of multi-cracked brittle media taking into account unilateral effects: theoretical and numerical approaches

Micromechanical and numerical methods are explored to predict the effective thermal and thermoelastic properties of a microcracked media. The effective properties are given in 2D and 3D. In this thesis, special attention is paid to the anisotropy, induced by the orientation of the cracks and the unilateral effect related to the opening and closing of the cracks.

The cracks are modelled as ellipsoidal inclusions. The open cracks are considered to have no stiffness and to be thermally insulating, whereas the closed cracks are represented by a fictitious isotropic material. The theoretical approach takes advantage of various homogenization schemes and bounds to derive closed-form expressions of effective properties. The numerical approach considers finite element modelling and is based on the same geometry and properties of cracks as in the theory. Finally, results are compared to demonstrate the consistency between the two approaches.

Keywords: thermomechanics, microcracked materials, homogenization, unilateral effect, finite element modelling

---

Comportement thermomécanique des matériaux fragiles microfissurés avec prise en compte des effets unilatéraux: approches théoriques et numériques

Dans ces travaux de thèse, des approches micromécaniques et numériques sont utilisées pour prédire les propriétés thermiques et thermoélastiques effectives d'un milieu microfissuré. Les développements sont effectués pour les cas bidimensionnel et tridimensionnel. Une attention particulière est portée à l'anisotropie induite par l'orientation des fissures et à l'effet unilatéral associé à leur ouverture/fermeture.

Plus précisément, les fissures sont modélisées comme des inclusions ellipsoïdales, sans rigidité et thermiquement isolantes dans le cas des fissures ouvertes et constituées d'un matériau isotrope fictif dans le cas des fissures fermées. L'approche théorique tire profit de différents schémas et bornes obtenues par homogénéisation pour déterminer les expressions analytiques des propriétés effectives. Sur le plan numérique, le travail s'appuie sur la modélisation par éléments finis et se base sur les mêmes géométrie et propriétés des fissures que celles retenues pour la démarche micromécanique. La comparaison des résultats permet de montrer la cohérence entre ces deux approches.

Mots clés: thermomécanique, matériaux microfissurés, homogénéisation, effet unilatéral, modélisation par éléments finis